

Politecnico di Torino

Politecnico di Torino

Laurea Magistrale in Ingegneria Aerospaziale

A.a. 2025/2026

Graduation Session March-April 2026

Analysis of the Dynamics for Lunar Satellite Constellations

Supervisors:

Stefano Mauro

Erica Scantamburlo

Domenico Sfasciamuro

Candidate:

Nicolò Sanzo

Table of Contents

List of Tables v

List of Figures vi

Glossary xii

Introduction 3

1 State of the art 4
1.1 Orbital Dynamics . . . 4
1.1.1 Kepler Restricted 2-Body Problem . . . 5
The Kepler Equation . . . 8
Orbital Elements . . . 10
Orbital Perturbations . . . 13
1.1.2 Lunar Orbits . . . 17
Selenocentric Reference Frames . . . 19
Lunar Gravity Geopotential Model . . . 21
Earth Tidal Acceleration . . . 24
Lunar Frozen Orbits . . . 25
1.2 Earth Satellite Constellations . . . 28
1.2.1 Coverage in adjacent planes . . . 33
1.2.2 Constellation Patterns . . . 36
Geosynchronous Constellations . . . 37
Streets of Coverage Constellations . . . 38
Walker Constellations . . . 39
Elliptical Orbit patterns . . . 41
Other Constellation patterns . . . 42
1.2.3 Selection of Constellation Parameters . . . 43
1.2.4 Constellation Design Process . . . 45

2 Methods 50
2.1 Python Code Organization . . . 51
2.1.1 `Perturbed_KR2BP.py` . . . 52
2.1.2 `Lunar_Perturbations.py` . . . 55
2.1.3 `Lunar_Frozen_Orbits.py` . . . 59
2.1.4 `Lunar_Constellations.py` . . . 64
2.1.5 `Lunar_RF_Transformations.py` . . . 68
2.1.6 `Simulations.py` . . . 72
2.2 Constellations Performance&Stability Metrics . . . 74
2.2.1 Constellation Survival and Degradation . . . 75
Specific Mechanical Energy Variation . . . 75
Semi-major Axis Statistics . . . 75
Perilune Altitude Statistics . . . 76
2.2.2 Frozen Stability Analysis . . . 76
Eccentricity Vector Phase-Space . . . 76
Argument of Perilune Evolution . . . 77
Kozai-Lidov Coupling . . . 77
2.2.3 Geometry Maintenance (Station-Keeping) . . . 78
Inclination Statistics . . . 78
Relative Mean Anomaly Drift . . . 78
Relative Node Spacing Drift . . . 79
2.2.4 Collision Avoidance Safety . . . 79
Global Minimum Inter-Satellite Distance . . . 79

3 Results 81
3.1 Search for Frozen Orbits . . . 81
3.2 Stability Analysis . . . 87
3.3 Semi-Major Axis Correction Map . . . 96
3.4 Inclination Correction Map . . . 105
3.5 Constellations Comparison . . . 114
3.5.1 $h = 1000$ km, $i = 85$ deg . . . 117
3.5.2 $h = 1000$ km, $i = 79$ deg . . . 122
3.5.3 $h = 800$ km, $i = 85$ deg . . . 127
3.5.4 $h = 800$ km, $i = 76$ deg . . . 132
3.5.5 $h = 600$ km, $i = 70$ deg . . . 137

4 Conclusions 142

Bibliography 145

List of Tables

1.1 Gravitational parameter of the Sun ($\odot$), the Earth ($\oplus$) and the Moon ($\leftmoon$). 6
1.2 Orbital constants of motion related to dynamics and geometric variables. Properties of the elliptical orbits. 9
1.3 Moon's characteristics and mean orbital elements. 19
1.4 Examples of operative Earth Satellite Constellations[47]. 29
1.5 Constellation design aspects based on a performance vs. cost analysis. 32
1.6 Principal Factors to be defined during Constellation Design. 47

3.1 Initial osculating orbital elements for a constellation Walker Delta 85: 3/1/0. 96
3.2 Initial osculating orbital elements for a constellation Walker Delta 85: 3/3/0. 107
3.3 Initial osculating orbital elements for a constellation Walker Delta 85: 3/3/0. 108
3.4 Best candidates orbits from the frozen stability analysis. 115
3.5 Custom Constellation Design Space for an orbit with initial osculating orbital elements: $h_0 = 1000\,\text{km}$, $i_0 = 85$ deg, $e_0 = 0.004556$ and $\omega_0 = 270$ deg. 117
3.6 Custom Constellation Design Space for an orbit with initial osculating orbital elements: $h_0 = 1000\,\text{km}$, $i_0 = 79$ deg, $e_0 = 0.005095$ and $\omega_0 = 270$ deg. 122
3.7 Custom Constellation Design Space for an orbit with initial osculating orbital elements: $h_0 = 800\,\text{km}$, $i_0 = 85$ deg, $e_0 = 0.005328$ and $\omega_0 = 270$ deg. 127
3.8 Custom Constellation Design Space for an orbit with initial osculating orbital elements: $h_0 = 800\,\text{km}$, $i_0 = 76$ deg, $e_0 = 0.007078$ and $\omega_0 = 270$ deg. 132
3.9 Custom Constellation Design Space for an orbit with initial osculating orbital elements: $h_0 = 600\,\text{km}$, $i_0 = 70$ deg, $e_0 = 0.014486$ and $\omega_0 = 270$ deg. 137

List of Figures

1.1 Schematic representation of the Kepler Restricted 2-Body Problem. 6
1.2 Geometrical dimensions of an elliptical orbit. 8
1.3 Eccentric anomaly E and True anomaly ν. 9
1.4 Classical orbital elements definition. 12
1.5 Moon's orbital elements representation[10]. 18
1.6 Selenocentric coordinates. 21
1.7 The orientation of Moon's north pole and prime meridian after IAU[21]. 22
1.8 The gravity field of the Moon as measured by the NASA GRAIL mission[32]. 23
1.9 Artistic representation of the GPS constellation. 31
1.10 Street of Coverage geometric representation. 34
1.11 Streets of Coverage geometries of adjacent orbital planes. 35
1.12 Relative geometry between two orbital planes at the same inclination. 36
1.13 Design of a Streets of Coverage constellation. 38
1.14 View of a Street of Coverage constellation seen from the north pole. 39
1.15 Walker Constellations: star and delta configuration. 40
1.16 Elliptical orbits constellation example[47]. 41
1.17 Examples of typical "Non-Walker" Constellations[47]. 42
1.18 Relationship between FOV and Earth Central Angle. 43
1.19 Cause-effect diagram of the Constellation Design Process. 49

2.1 Python code organization represented with a system architecture flowchart. 52

3.1 Frozen Orbits solutions space for semi-major axis $a = 1862.4\,\text{km}$. Zonal Harmonics up to degree $n = 20$. 82
3.2 Frozen Orbits solutions space for semi-major axis $a = 1861\,\text{km}$. Zonal Harmonics up to degree $n = 50$. 83
3.3 Frozen Orbits solutions space for altitude $h = 100\,\text{km}$. 84
3.4 Frozen Orbits solutions space for altitude $h = 300\,\text{km}$. 84
3.5 Frozen Orbits solutions space for altitude $h = 500\,\text{km}$. 85

3.6 Frozen Orbits solutions space for altitude $h = 700\,\text{km}$. 85
3.7 Frozen Orbits solutions space for altitude $h = 1000\,\text{km}$. 86
3.8 Frozen Orbits solutions space for altitude $h = 5000\,\text{km}$. 87
3.9 Evolution of the argument of Peri-apsis (ω) over 1-year, for a LFO with $h = 1000\,\text{km}$ and $i = 35$ deg. 88
3.10 Evolution of the argument of Peri-apsis (ω) over 1-year, for a LFO with $h = 1000\,\text{km}$ and $i = 57.5$ deg. 88
3.11 Evolution of the argument of Peri-apsis (ω) over 1-year, for a LFO with $h = 200\,\text{km}$ and $i = 85$ deg. 89
3.12 Eccentricity Vector Phase-Space Evolution for the following orbits: Top left: $h = 1000\,\text{km}$, $i = 35$ deg; Top right: $h = 800\,\text{km}$, $i = 79$ deg; Bottom left: $h = 1000\,\text{km}$, $i = 57.5$ deg; Bottom right: $h = 1000\,km$, $i = 34$ deg. 90
3.13 Orbital safety analysis: 1-year evolution of the Perilune Altitude (h_p). Initial orbital elements: $h = 400\,\text{km}$, $i = 76$ deg, $e = 0.007632$. 91
3.14 Orbital safety analysis: 1-year evolution of the Perilune Altitude (h_p). Initial orbital elements: $h = 200\,\text{km}$, $i = 82$ deg, $e = 0.000483$. 92
3.15 Orbital safety analysis: 1-year evolution of the Perilune Altitude (h_p). Initial orbital elements: $h = 100\,\text{km}$, $i = 82$ deg, $e = 0.008332$. 92
3.16 Perilune altitude (h_p) stability statistics: minimum perilune altitude and altitude breathing VS initial orbital elements (h, i). 93
3.17 Frozen stability: amplitude of the oscillations of the argument of peri-apsis (ω) VS initial orbital elements (h, i). 94
3.18 Secondary frozen stability: Mean and Max dispersion of the eccentricity vector $(e\cos\omega, e\sin\omega)$ VS initial orbital elements (h, i). . . . 95
3.19 Semi-Major Axis 1-year evolution for a constellation with 3 satellites in 1 plane, deployed at $M_0 = [0,120,240]\,\text{deg}$. Initial osculating orbital elements: $h = 1000\,\text{km}$, $i = 85$ deg. 97
3.20 Relative Mean Anomaly Drift for a constellation with 3 satellites in 1 plane, deployed at $M_0 = [0,120,240]\,\text{deg}$. Initial orbital elements: $h = 1000\,\text{km}$, $i = 85$ deg. 97
3.21 Mean Semi-major axis VS initial orbital elements (h, Ω). 98
3.22 Mean Semi-major axis VS initial osculating orbital elements (h, M_e). 99
3.23 Semi-major Axis correction map: a_{mean} deviation correlated to initial RAAN (Ω) and Mean Anomaly (M_e). Initial osculating orbital elements: $h = 1000$, $i = 85$ deg. 100
3.24 Semi-major Axis correction map: a_{mean} deviation correlated to initial RAAN (Ω) and Mean Anomaly (M_e). Initial osculating orbital elements: $h = 600$, $i = 85$ deg. 101

3.25 Semi-major Axis correction map: a_{mean} deviation correlated to initial RAAN (Ω) and Mean Anomaly (M_e). Initial osculating orbital elements: $h = 1000$, $i = 70$ deg. 102
3.26 Semi-major Axis correction map: a_{mean} deviation correlated to initial RAAN (Ω) and Mean Anomaly (M_e). Initial osculating orbital elements: $h = 300$, $i = 85$ deg. 103
3.27 Semi-major Axis correction map: a_{mean} deviation correlated to initial RAAN (Ω) and Mean Anomaly (M_e). Initial osculating orbital elements: $h = 600$, $i = 70$ deg. 104
3.28 Semi-major Axis correction map: a_{mean} deviation correlated to initial RAAN (Ω) and Mean Anomaly (M_e). Initial osculating orbital elements: $h = 300$, $i = 70$ deg. 105
3.29 Inclination drift 1-year evolution for a constellation with 3 orbital planes at $\Omega_0 = [0,120,240]$ deg. Initial osculating orbital elements: $h = 1000$ km, $i = 85$ deg. 106
3.30 Kozai-Lidov coupling between eccentricity and inclination. Walker Star constellation pattern: 85:3/3/0. 107
3.31 Inclination drift linear regression VS initial osculating orbital elements (h_0, i_0). 108
3.32 Inclination drift 1-year evolution for a constellation Walker Delta 85:12/1/0, initialized at $h_0 = 300$ km. 109
3.33 Inclination Drift correction map: $\frac{di}{dt}$ linear regression correlated to initial RAAN (Ω) and Inclination (i_0). Initial osculating orbital elements: $h = 1000$ km. 110
3.34 Inclination Drift correction map: $\frac{di}{dt}$ linear regression correlated to initial RAAN (Ω) and Inclination (i_0). Initial osculating orbital elements: $h = 800$ km. 111
3.35 Inclination Drift correction map: $\frac{di}{dt}$ linear regression correlated to initial RAAN (Ω) and Inclination (i_0). Initial osculating orbital elements: $h = 600$ km. 112
3.36 Inclination Drift correction map: $\frac{di}{dt}$ linear regression correlated to initial RAAN (Ω) and Inclination (i_0). Initial osculating orbital elements: $h = 300$ km. 113
3.37 Inclination Drift correction map: $\frac{di}{dt}$ linear regression correlated to initial RAAN (Ω) and Inclination (i_0). Initial osculating orbital elements: $h = 100$ km. 114
3.38 Standard Deviation of the Semi-Major Axis for all the constellations of the Design Space at $h = 1000$ km and $i = 85$ deg. 118
3.39 Standard Deviation of the Inclination for all the constellations of the Design Space at $h = 1000$ km and $i = 85$ deg. 119

3.40 Mean Dispersion of the Eccentricity Vector for all the constellations of the Design Space at $h = 1000$ km and $i = 85$ deg. 119
3.41 Max Slope of the Relative Node Drift (Inter-plane spacing) for all the constellations of the Design Space at $h = 1000$ km and $i = 85$ deg. 120
3.42 Max Slope of the Relative Mean Anomaly Drift (Intra-plane phasing) for all the constellations of the Design Space at $h = 1000$ km and $i = 85$ deg. 120
3.43 Number of Collision Avoidance Events for all the constellations of the Design Space at $h = 1000$ km and $i = 85$ deg. 121
3.44 Standard Deviation of the Semi-Major Axis for all the constellations of the Design Space at $h = 1000$ km and $i = 79$ deg. 123
3.45 Standard Deviation of the Inclination for all the constellations of the Design Space at $h = 1000$ km and $i = 79$ deg. 124
3.46 Mean Dispersion of the Eccentricity Vector for all the constellations of the Design Space at $h = 1000$ km and $i = 79$ deg. 124
3.47 Max Slope of the Relative Node Drift (Inter-plane spacing) for all the constellations of the Design Space at $h = 1000$ km and $i = 79$ deg. 125
3.48 Max Slope of the Relative Mean Anomaly Drift (Intra-plane phasing) for all the constellations of the Design Space at $h = 1000$ km and $i = 79$ deg. 125
3.49 Number of Collision Avoidance Events for all the constellations of the Design Space at $h = 1000$ km and $i = 79$ deg. 126
3.50 Standard Deviation of the Semi-Major Axis for all the constellations of the Design Space at $h = 800$ km and $i = 85$ deg. 128
3.51 Standard Deviation of the Inclination for all the constellations of the Design Space at $h = 800$ km and $i = 85$ deg. 129
3.52 Mean Dispersion of the Eccentricity Vector for all the constellations of the Design Space at $h = 800$ km and $i = 85$ deg. 129
3.53 Max Slope of the Relative Node Drift (Inter-plane spacing) for all the constellations of the Design Space at $h = 800$ km and $i = 85$ deg. 130
3.54 Max Slope of the Relative Mean Anomaly Drift (Intra-plane phasing) for all the constellations of the Design Space at $h = 800$ km and $i = 85$ deg. 130
3.55 Number of Collision Avoidance Events for all the constellations of the Design Space at $h = 800$ km and $i = 85$ deg. 131
3.56 Standard Deviation of the Semi-Major Axis for all the constellations of the Design Space at $h = 800$ km and $i = 76$ deg. 133
3.57 Standard Deviation of the Inclination for all the constellations of the Design Space at $h = 800$ km and $i = 76$ deg. 134
3.58 Mean Dispersion of the Eccentricity Vector for all the constellations of the Design Space at $h = 800$ km and $i = 76$ deg. 134

3.59 Max Slope of the Relative Node Drift (Inter-plane spacing) for all the constellations of the Design Space at $h = 800\,\text{km}$ and $i = 76$ deg. 135
3.60 Max Slope of the Relative Mean Anomaly Drift (Intra-plane phasing) for all the constellations of the Design Space at $h = 800\,\text{km}$ and $i = 76$ deg. 135
3.61 Number of Collision Avoidance Events for all the constellations of the Design Space at $h = 800\,\text{km}$ and $i = 76$ deg. 136
3.62 Standard Deviation of the Semi-Major Axis for all the constellations of the Design Space at $h = 600\,\text{km}$ and $i = 70$ deg. 138
3.63 Standard Deviation of the Inclination for all the constellations of the Design Space at $h = 600\,\text{km}$ and $i = 70$ deg. 139
3.64 Mean Dispersion of the Eccentricity Vector for all the constellations of the Design Space at $h = 600\,\text{km}$ and $i = 70$ deg. 139
3.65 Max Slope of the Relative Node Drift (Inter-plane spacing) for all the constellations of the Design Space at $h = 600\,\text{km}$ and $i = 70$ deg. 140
3.66 Max Slope of the Relative Mean Anomaly Drift (Intra-plane phasing) for all the constellations of the Design Space at $h = 600\,\text{km}$ and $i = 70$ deg. 140
3.67 Number of Collision Avoidance Events for all the constellations of the Design Space at $h = 600\,\text{km}$ and $i = 70$ deg. 141

List of Algorithms

1 Direct Time Problem . . . 10
2 Inverse Time Problem . . . 11
3 The Constellation Design process. . . . 46
4 Equations of Motion for Perturbed Two-Body Problem . . . 53
5 Numerical Integration of the Perturbed KR2BP (Cowell's Method) 53
6 Equations of Motion for Unperturbed KR2BP . . . 54
7 Numerical Integration of KR2BP . . . 54
8 Processing and Extraction of GRAIL Spherical Harmonic Coefficients 56
9 Loading SPICE Kernels . . . 57
10 Lunar Gravity Perturbation Calculation . . . 58
11 Earth Third-Body Perturbation Calculation . . . 59
12 Computation of the summation term $S_n^\star$ . . . 61
13 Differential equation $\dot{g}(e)$ . . . 61
14 Calculation of Frozen Orbit Eccentricity . . . 62
15 Computation of LFOs and Inclination-Eccentricity Diagram . . . 63
16 Retrieve Frozen Orbit Elements . . . 64
17 Generation of Walker Delta Constellation . . . 65
18 Generation of Walker Star Constellation . . . 66
19 Generation of Streets of Coverage (SoC) Constellation . . . 67
20 Conversion from Keplerian Elements to Cartesian State Vector . . . 69
21 Conversion from Cartesian State Vector to Keplerian Elements . . . 70
22 Conversion from Mean Anomaly to True Anomaly . . . 71
23 Geometric-Only Frame Transformation . . . 71
24 Full State Vector Transformation via SPICE . . . 72
25 Full Lunar Constellation Simulation . . . 73
26 Full Lunar Constellation Simulation (Part 2) . . . 74
27 Generate Custom Constellation . . . 116

Glossary

ESA European Space Agency

NASA National Aeronautics and Space Administration

NavCom Navigation and Communication

GPS Global Positioning System

Mascons Mass concentrations

LFO Lunar Frozen Orbit

GRAIL Gravity Recovery And Interior Laboratory

SPICE Spacecraft, Planet, Instrument, C-matrix, Events

LLO Low Lunar Orbit

MLO Medium Lunar Orbit

HLO High Lunar Orbit

KR2BP Kepler Restricted 2-Body Problem

PKR2BP Perturbed Kepler Restricted 2-Body Problem

ODE Ordinary Differential Equations

ECI Earth-Centered Inertial

ECEF Earth-Centered Earth-Fixed

RAAN Right Ascension of the Ascending Node

OE Orbital Elements

IAU International Astronomical Union

RF Reference Frame

ICRF International Celestial Reference Frame

ME Mean-Earth Reference Frame

PALRF Principal Axis Lunar Reference Frame

MCI Moon-Centered Inertial

VLBI Very-Long Baseline Interferometer

ET Ephemeris Time

UTC Universal Time Coordinated

J2000 Julian Epoch 01/01/2000 12:00:00 UTC

JPL Jet Propulsion Laboratory

DE Development Ephemeris

JD Julian Day

NRHO Near-Rectilinear Halo Orbit

DRO Distant Retrograde Orbit

CR3BP Circular Restricted 3-Body Problem

ELFO Elliptical Low Frozen Orbit

FOC Full Operational Capability

LEO Low Earth Orbit

MEO Medium Earth Orbit

GEO Geostationary Earth Orbit

GSO GeoSynchronous Orbit

IGSO Inclined Geostationary Sun-synchronous Orbit

GLONASS Global Navigation Satellite System

WGS Wideband Global SATCOM

TDRSS Tracking and Data Relay Satellite System

DMC Disaster Monitoring Constellation

USA United States of America

USSF United States Space Force

EUSPA European Union Agency for the Space Programme

MUOS Mobile User Objective System

EU European Union

EO Earth Observation

SoC Streets of Coverage

MECA Maximum Earth Central Angle

FOV Field of View

PDS Planetary Data System

SRP Solar Radiation Pressure

LSK Leap-Seconds Kernel

PCK Planetary Constants Kernel

SPK Spacecraft & Planetary constants Kernel

FK Frame Kernel

SV State Vector

SMA Semi-Major Axis

Abstract

In the context of the renewed global interest in lunar exploration, driven by initiatives such as NASA's Artemis program and ESA's Moonlight, the establishment of a reliable satellites system infrastructure is a critical technological prerequisite to accomplish mission objectives as Navigation & Communication or Moon Observation. Unlike Earth-orbiting systems, the deployment of satellite constellations around the Moon faces unique dynamical challenges arising from the highly non-uniform lunar gravitational field and significant third-body perturbations from the Earth. This thesis addresses the dynamical feasibility of adapting standard Earth-like constellation patterns (specifically Walker Delta, Walker Star, and Streets of Coverage) to the lunar environment by exploiting the theory of Lunar Frozen Orbits (LFOs). The primary objective is to examine the orbital dynamics of lunar constellations, prioritizing physical survivability and geometric stability. To this end, a high-fidelity numerical propagator was developed in Python, integrating the equations of motion using Cowell's Method with an 8th-order Dormand-Prince solver, incorporating the GRAIL gravity model and precise ephemerides via the NASA SPICE toolkit. The methodology begins with the identification of stable LFOs using a double-averaging analytical theory, followed by a numerical stability analysis that characterizes the capacity of orbits across a grid of altitudes and inclinations to mantain frozen characteristics. The results indicate that the majority of solutions show stability behaviours, except for the existence of critical regions, particularly for altitudes below 200 km due to mascon effects and near the critical inclination of 57 degrees. A significant contribution of this work is the computation of maps which characterize the secular drift of the semi-major axis and inclination as a function of the initial Right Ascension of the Ascending Node (RAAN) and Mean Anomaly, called "Correction Maps", and offering a predictive tool for minimizing geometric degradation as an alternative to the Mean-to-Osculating orbital elements conversion. Finally, the research evaluates the comparative performance of Walker and Streets of Coverage patterns with respect to custom-generated constellations where the lunar perturbations are minimized by selecting the initial osculating orbital elements from the Correction Maps, and evaluating performance consistency if the total number of satellites is increased. Earth-like constellation patterns are feasible for lunar operations, on the condition that they are adapted to the frozen condition, thereby establishing a dynamical baseline for future lunar constellation design.

Introduction

In the last decade, the aerospace sector has witnessed a renaissance in lunar exploration, driven by the strategic goal of establishing a permanent human presence on the Moon rather than short-term visits. The "race" to the Moon has restarted in a new form, attracting ever increasing investments by governments, private companies and academia, with an estimated grow of the lunar exploration market up to $12+ billion in the near future[1]. Unlike the Apollo era, current initiatives such as NASA's Artemis program and the Lunar Gateway aim to create a sustainable ecosystem, relying heavily on international cooperation and commercial partnerships[2][3]. However, a critical bottleneck for these ambitions is the lack of dedicated infrastructure. As identified by the European Space Agency (ESA), over 400 lunar missions are planned by various agencies and private companies over the next two years, all of which require reliable Navigation and Communication (NavCom) capabilities[4]. Currently, these missions must carry heavy, complex standalone communication systems to link directly with Earth. To solve this, ESA's Moonlight initiative proposes a dedicated constellation of lunar satellites to provide shared telecommunications and navigation services[5]. This shared infrastructure would allow future landers and rovers to be lighter and more cost-efficient, enabling them to focus on scientific instruments rather than logistical support[6]. Consequently, the analysis of stable orbital dynamics for such constellations has become a priority for the space community.

While robust satellite constellations like GPS, Galileo, and Starlink have revolutionized navigation and connectivity on Earth, these architectures cannot simply be "copied and pasted" to the lunar environment[7]. The primary barrier is the Moon's hostile and highly unstable gravitational field, which differs fundamentally from Earth's. Unlike the uniform oblateness of our planet, the Moon's mass beneath its surface is not uniformly distributed due to the presence of "Mascons" (Mass Concentrations), which create significant gravitational anomalies[8]. When combined with the strong third-body gravitational perturbations from the Earth (tidal forces), these anomalies cause standard low-altitude orbits to degrade rapidly. A satellite placed in a circular orbit that would be stable around Earth might

crash into the lunar surface or drift into a useless trajectory within a matter of weeks[7]. This instability creates a critical design "gap": future missions require the continuous coverage of a constellation, yet the lunar environment actively works to destroy the very orbital geometry needed to sustain it.

To address this instability, this thesis focuses on the theory of Lunar Frozen Orbits (LFOs) as a primary solution. Unlike standard circular orbits, LFOs exploit specific combinations of eccentricity (e) and inclination (i) that naturally cancel out the disturbing effects of the lunar gravitational potential. By carefully selecting these "freezing" parameters, the secular variations in the eccentricity vector and the argument of perilune are minimized, effectively locking the orbit's geometry in place over long durations. My research focuses on identifying these stable regions within the phase space and applying them to constellation design, and verify the behaviour of the constellation dynamics under these assumptions. This approach aims to drastically reduce the station-keeping fuel required (ΔV) to maintain the constellation, rendering long-term lunar navigation and communication infrastructures feasible and cost-effective.

The main objective of this thesis is to analyze whether "Earth-like" constellation patterns can survive and function in the lunar orbital environment if they are adapted to the LFOs theory. The dynamics is analyzed from the point of view of the survivability and stability metrics, therefore it is not a cost analysis related to the mission design trade-off. The purpose is to deploy a constellation of satellites in orbit around the Moon and propagate their trajectory with a high-fidelity numerical integration of the equations of motion, in a passive control mode. For this reason, no orbit corrections are performed by the control system to keep the spacecraft in a station-keeping box. Instead, the spacecraft undergo the perturbing acceleration given by the gravitational environment of the Moon, and the evolution of the orbital elements is analyzed to verify how much different is the dynamics of lunar satellite constellations with respect to the Earth's counterpart.

To rigorously assess the stability of these constellation architectures, this study relies on a custom-developed high-fidelity numerical propagator implemented in Python. Unlike simplified analytical approximations, this tool integrates the full non-linear equations of motion using Cowell's Method, allowing for the precise accumulation of perturbing forces over time. The simulation environment is anchored in high-precision empirical data, specifically incorporating the GRAIL gravity model to capture the Moon's complex mass concentrations and NASA's SPICE toolkit to retrieve exact ephemerides for the Earth third-body perturbations. By systematically propagating thousands of initial conditions through this robust framework, the software captures the subtle long-term evolution of lunar satellite tracks. This

computational approach ensures that the identified "preliminary" frozen orbits are not merely theoretical mathematical solutions, but valid trajectories capable of surviving the actual, chaotic dynamical environment of cislunar space.

The scope of this research is strictly defined by specific orbital regimes and stability metrics. Geometrically, the analysis focuses on Low Lunar Orbits (LLO) and Medium Lunar Orbits (MLO), with an altitude ceiling of 5000 km, as these are the most critical regions for high-performance surface navigation. It is important to note that while factors such as launch costs, specific hardware design, and detailed link budget calculations are essential for a complete mission architecture, they fall outside the purview of this study. Instead, the primary objective is to isolate and quantify the orbital dynamics: prioritizing metrics such as survival time and degradation rates. This distinction ensures that the physical feasibility of the constellation's geometry is validated before logistical or economic constraints are applied.

The remainder of this thesis is organized into four distinct chapters. Chapter 1 provides a comprehensive review of the state of the art, covering the fundamental principles of orbital mechanics, the specific perturbations present in the lunar environment, and the theory behind standard constellation architectures. Chapter 2 details the methodology, describing the architecture of the custom Python simulation tool, the numerical integration algorithms employed, and the specific metrics defined to quantify orbital stability and the constellation performance metrics. Chapter 3 presents the core results of the study, offering a comparative analysis of the survival rates and degradation patterns for Walker and Streets of Coverage constellations under varying initial conditions, identifying trends and discussing the feasible lunar constellations. Finally, Chapter 4 summarizes the key findings, discusses the implications for future lunar infrastructure, and outlines the potential direction for further research.

Chapter 1

State of the art

1.1 Orbital Dynamics

Orbital dynamics is defined as the branch of astrodynamics that focuses on describing the motion of natural and artificial bodies under the influence of gravitational forces. The main purpose is to predict the position and the velocity of any object moving in the universe, describing mathematically the evolution of these quantities in time, the main causes for the motion, and the geometrical properties of this motion in the case of particular conditions. The latter is the formal definition of orbit, a trajectory in space with particular symmetries or properties generated by the balance of gravitational and inertial forces. It has always been an interest of humanity to be able to predict astronomical phenomena, and many cultures have contributed during the history, moved by very diverse motivations.

For example, ancient Mesopotamian populations were able to predict Moon eclipses and Sun conjunctions based on empirical observation, and discovered a periodicity in the movement of celestial bodies in the sky. In the Hellenistic period, many philosophers like Pythagoras, Aristotle, and Ptolemaus proposed for the first time the idea of circular motion of the celestial bodies around the Earth, which was believed to be at the center of the universe. This idea was formulated on the firm belief that the universe had to be geometrically perfect and in harmony with nature. We had to wait the 16th century for a new disruption of the point of view in orbital dynamics. Mikołaj Kopernik opened the doors for the birth of celestial mechanics, when he stated the Earth was orbiting around the Sun in circular orbit. The following studies and observations of Tycho Brahe, Johann Kepler and Galileo Galilei led to the formulation of the Law of Universal Gravitation by Isaac Newton, which, together with the Three Laws of Motion, is considered the foundation of

modern orbital dynamics. Newton was also able to derive mathematically the Kepler Laws, and defined the Kepler 2-body problem, which will be investigated in the next section. From the beginning of 18th century the age of "analytical mechanics" began, and thanks to the contributions of Euler, Lagrange and Laplace, the orbital dynamics are transformed into an analytical science, where more complex problems are solved (i.e. the three-body problem, the perturbation theory and the orbital stability). The last century is considered the "Space Age", during which the expanding capabilities of computers determined more accurate solutions to the orbital dynamics equations of motion. Engineers are nowadays able to create numerical and high-fidelity models to describe the orbital motion and perturbations, which led to the first man-made satellites in Earth orbit and all the space missions up to today[9].

Before we delve into the description of artificial satellite constellations, it is necessary to describe the orbital dynamics of lunar orbits starting from a simple analytical model, such as the Kepler Restricted 2-Body Problem using the Newtonian mechanics, up to the inclusion of orbital perturbations that typically occur in the vicinity of the Moon.

1.1.1 Kepler Restricted 2-Body Problem

The Kepler Restricted 2-Body Problem describes the motion of an artificial satellite around a planet called a "central body", in the absence of external forces and with the assumption that both the bodies are spherically symmetric. To summarize the procedure by which Newton was able to derive the final equation of motion, he considered n bodies of mass m_i with $i = 1, ..., n$ and applied the *2nd Newton's Law* describing the interaction between the motion of the body i-th (effect) and the forces acting on it (cause):

$$\vec{F} = \frac{d}{dt}\left(m_i \vec{\dot{r}_i}\right) \tag{1.1}$$

where $\vec{F}$ is the sum of all forces acting on the body, both gravitational and non-gravitational, whereas m_i is the mass of the body and $\vec{\dot{r}_i}$ is the velocity vector. For instance, he neglected the non-gravitational perturbations and substituted the *Law of Universal Gravitation*:

$$\vec{F_{ji}} = -G\frac{m_i m_j}{r_{ji}^3}\vec{r_{ji}} \quad , \quad \vec{r_{ji}} = \vec{r_j} - \vec{r_i} \tag{1.2}$$

which describes the gravitational force caused by the mass of body jth and acting on body ith. It is important to mention that the position, velocity and acceleration vectors are expressed in an inertial reference frame, as it is the only way the *Newton's Laws of Motion* are valid. $G = 6.673 \cdot 10^{-11}\ \frac{m^3}{kg\ s^2}$ is the Universal

Gravitational Constant, derived by Newton in his formulation. Finally, he formulates the final hypothesis: there are only 2 bodies with mass M (central body mass, i.e., a planet) and m (secondary body mass, i.e., an artificial satellite) with $M >> m$ and therefore $M + m \approx M$; only gravitational forces act on the masses; the bodies are spherically symmetric.

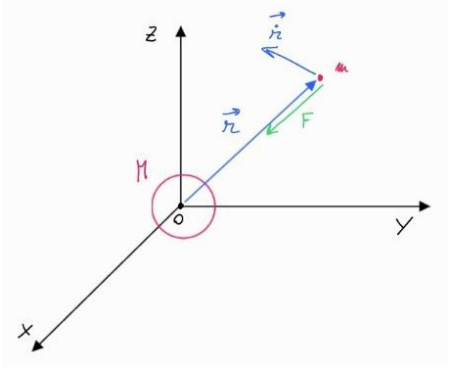


Figure 1.1: Schematic representation of the Kepler Restricted 2-Body Problem.

The final formulation expressed in terms of relative position, velocity and acceleration of the secondary body with respect to the central body, is:

$$\ddot{\vec{r}} + \frac{\mu}{r^3}\vec{r} = 0 \quad , \quad \mu = GM \tag{1.3}$$

The great breakthrough that this equation discovered is the possibility to find a closed-form solution $\vec{r}(t)$ for the trajectory of the satellite in orbit around a planet. The constant μ is the *gravitational parameter* and it is a value proportional with the mass of the central body, indicating how strong is the gravitational pull around the center of mass of the main planet. The most useful gravitational parameters that will be used in this dissertation are the central bodies of the Sun ($\odot$), Earth ($\oplus$) and the Moon ($\leftmoon$):

Body	μ $[\mathbf{m}^3\,\mathbf{s}^{-2}]$	μ $[\mathbf{km}^3\,\mathbf{s}^{-2}]$
$\mu_\odot$	$1.32712440018 \cdot 10^{20}$	$132712 \cdot 10^6$
$\mu_\oplus$	$3.986004418 \cdot 10^{14}$	398600
$\mu_\leftmoon$	$4.9048695 \cdot 10^{12}$	$\mu_\oplus/81.3$

Table 1.1: Gravitational parameter of the Sun ($\odot$), the Earth ($\oplus$) and the Moon ($\leftmoon$).

Newton was able to prove that the solution of the equation of motion represents, if the trajectory is expressed in polar coordinates, a conic section, in compliance to what Kepler had predicted a century earlier. A conic section is generated by the intersection of an infinite cone cut by a plane with a general inclination, and it is defined as the locus of points whose distance from the focus is proportional to the horizontal distance from a vertical line known as the conic section directrix. In this way it is possible to link dynamics variables to geometric variables, simplifying the analysis of the trajectories. This similarity not only verifies *Kepler's First Law*, but allows us to find other important properties of orbits in the KR2BP:

1. The conic section represents the only solution for the satellite trajectory in the KR2BP;
2. One of the foci of the conic orbit must be located at the center of the central body;
3. The specific mechanical energy (per unit mass) is conserved:

$$\epsilon = \frac{V^2}{2} - \frac{\mu}{r} = const. \tag{1.4}$$

4. The angular momentum is conserved:

$$\vec{h} = \vec{r} \times \vec{V} = const. \tag{1.5}$$

5. The orbital motion takes place in a plane which is fixed in the inertial space;

According to geometry theorems, a conic section can be either a *circle*, an *ellipse*, a *parabola* or a *hyperbola*, but for the purpose of analyzing the orbits of artificial satellites around the Moon, it is sufficient to describe elliptical and circular orbits, where the circle is simply an ellipse where the two foci coincide in one single point.

Solving the Kepler Restricted 2-Body Problem of Eq. (1.3) in polar coordinates is straightforward and leads to the closed-form solution of the position of the secondary body m:

$$r(t) = \frac{p}{1 + e\cos\nu(t)} \tag{1.6}$$

where p is the *semi-latus rectum* and e is the *eccentricity* , which are geometric constants of any conic sections and showed in Fig. 1.2 in the case of an elliptical orbit. The central body is located in the focus of the ellipse, then it is possible to define the *periapsis* r_p as the closest point of the trajectory from the focus, and the *apoapsis* r_a the furthest point from the focus. Other geometrical constants of the

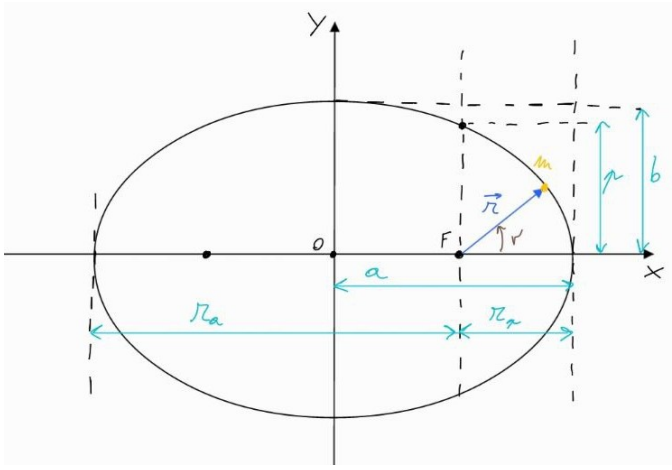


Figure 1.2: Geometrical dimensions of an elliptical orbit.

ellipse are the *semi-major axis* a and the *semi-minor axis* b indicated in the Figure 1.2. The coordinate system represented in Fig. 1.2 is called Perifocal Coordinate System, whose origin is at the center of mass of the central body, $\hat{x}$ axis lies on the orbital plane in the direction of the semi-major axis and pointing towards periapsis, $\hat{y}$ axis in the direction of the semi-latus rectum 90 deg in the direction of motion and $\hat{z}$ axis perpendicular to the orbital plane in the verse of $\vec{h}$. From Eq. (1.3) it is possible to determine the state vector of a satellite in orbit around a central body, assuming all the hypothesis of the KR2BP are respected:

$$\vec{r} = \begin{Bmatrix} r \cdot \cos\nu \\ r \cdot \sin\nu \\ 0 \end{Bmatrix} \quad , \quad \dot{\vec{r}} = \begin{Bmatrix} -\frac{\mu}{h} \cdot \sin\nu \\ \frac{\mu}{h} \cdot (e + \cos\nu) \\ 0 \end{Bmatrix} \tag{1.7}$$

The Table 1.2 below includes all the constants of the KR2BP and the formulas to calculate them using dynamics or geometric variables. The mathematical derivation of these results is deeply investigated in [10].

The Kepler Equation

Now that the shape of an orbital conic section has been described, the last step to compute the trajectory evolution in time of the satellite is to find the function $\nu(t)$, where ν is the *true anomaly* and it is defined as anti-clockwise angle measured from the periapsis to the position vector at the time t. To do so, we need to use Kepler Laws and to define the so-called "Time Problem". From the *3rd Kepler's Law*, the

Orbital constant		Dynamics	Geometric	Property
Specific mechanical energy	ϵ	$\frac{V^2}{2} - \frac{\mu}{r}$	$-\frac{\mu}{2a}$	$\epsilon < 0$
Angular momentum	h	$rV\cos\varphi$	$\sqrt{p\mu}$	$\vec{h} \parallel \hat{z}$
Semi-latus rectum	p	$\frac{h^2}{\mu}$	$a(1-e^2)$	$p > 0$
Eccentricity	e	$\sqrt{1+\frac{2\epsilon h^2}{\mu^2}}$	$\frac{r_a - r_p}{r_a + r_p}$	$0 \leq e < 1$
Semi-major axis	a	$\frac{-\mu}{2\epsilon}$	$\frac{r_a + r_p}{2}$	$a > 0$

Table 1.2: Orbital constants of motion related to dynamics and geometric variables. Properties of the elliptical orbits.

orbital period T and the *mean motion* n are derived:

$$T = 2\pi\sqrt{\frac{a^3}{\mu}} \quad , \quad n = \sqrt{\frac{\mu}{a^3}} \tag{1.8}$$

From the *2nd Kepler's Law*, we know that the position vector sweeps equal areas in equal time, thus:

$$\frac{\Delta t}{A_1} = \frac{T}{\pi ab} \tag{1.9}$$

where A_1 is shown in Fig. 1.3.

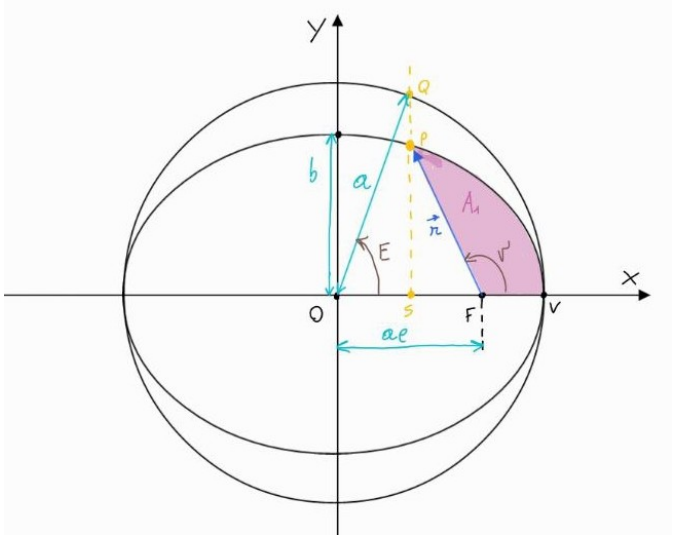


Figure 1.3: Eccentric anomaly E and True anomaly ν.

The process goes on by defining the *eccentric anomaly* E and the *mean anomaly* M_e, contructed by circumscribing a circle with radius a and extending in the vertical direction from point P in the Fig. 1.3.

$$\cos E = \frac{e + \cos \nu}{1 + e \cos \nu} \quad , \quad M_e = E - e \sin E \tag{1.10}$$

The second of Eq.(1.11) is called *Kepler's Equation*, and it can be derived to find the time passed between a generic position 1 to a position 2 in the ellipse. The mathematical proof is described in [10], as well as the same derivation for other conic sections, thus only the final result valid for the ellipse is presented:

$$t_2 - t_1 = \sqrt{\frac{a^3}{\mu}}(M_{e,2} - M_{e,1}) \tag{1.11}$$

The time problem branches out in the Direct Problem and the Inverse Problem. In the Direct Problem, the true anomaly $\Delta\nu$ is known and we want to compute how long does it take for the satellite to sweep this angle (Δt). In this case, the procedure is the following:

Algorithm 1 Direct Time Problem

ν is known;
$\nu \leftarrow \cos E$ through Eq.(1.10);
$\cos E \leftarrow E$;
if $0 < \nu < \pi$ **then**
    $0 < E < \pi$;
else if $\pi < \nu < 2\pi$ **then**
    $\pi < E < 2\pi$;
end if
$E \leftarrow M_e$ through Eq.(1.10);
$M_e \leftarrow t$ through Eq.(1.11).

In the Inverse Problem, the time-of-flight Δt is known, and we want to compute the angular position of the satellite ($\Delta\nu$):

Orbital Elements

Until now, we have discussed the KR2BP without properly defining any coordinate system. In real case applications, such as Earth and Lunar orbits, it is important to define a defined set of coordinates and a system of time measurement to be able to describe position and velocity vectors. While selenocentric reference frames are discussed in the next sections, for the purpose of describing the state vector of an

Algorithm 2 Inverse Time Problem

t is known
$t \leftarrow M_e$ through Eq.(1.11)
procedure NEWTON'S ITERATIVE METHOD($f, f', x_0, tol, N_{\max}$)
    $M_e \leftarrow E_0$
    $i = 1$
    while $err < tol$ or $N_{it} > N_{\max}$ **do**
        $f(E_{i-1}) = E_{i-1} - e \sin E_{i-1}$
        $f'(E_{i-1}) = 1 - e \cos E_{i-1}$
        $E_i = E_{i-1} + \frac{M_e - f(E_{i-1})}{f'(E_{i-1})}$
        $i \leftarrow i + 1$
    end while
    $E_0 \leftarrow E$
end procedure

orbiting satellite, the following coordinates systems are defined:

- *Geocentric-Equatorial*: it has the origin at the center of the Earth, the fundamental plane is the equatorial on which the x-axis lie pointing towards the vernal equinox, the z-axis is in the direction of the North Pole and this frame is non-rotating with respect to the stars. This reference frame is often referred as *Earth-Centered Inertial* to underline its main characteristic that it is possible to use it to determine Earth orbits in a cartesian coordinate system[11].

- *Right Ascension-Declination*: it is related to the ECI but the position of the objects is rather expressed in polar coordinates (r, α, δ) which can be easier to determine. The right ascension (α) is the angle measured on the equatorial plane from the vernal equinox and it is the analogous of the longitude on the Earth's surface for the celestial sphere; the declination (δ) is the angular displacement from the equatorial plane and it is the analogous of the latitude[11];

- *Perifocal*: the most convenient coordinate system for describing the motion of a satellite. It has the origin at the focus of the orbit (the center of the Earth for terrestial orbits), the z-axis is in the direction of the angular momentum and therefore perpendicular to the orbital plane, the x-axis points towards the periapsis and the y-axis is defined with the rigth-hand rule[11].

To describe the state vector of a satellite in orbit, 5 elements are needed to

describe the shape, orientation and size of the latter, while 1 last element is needed to define the position at a specified epoch.

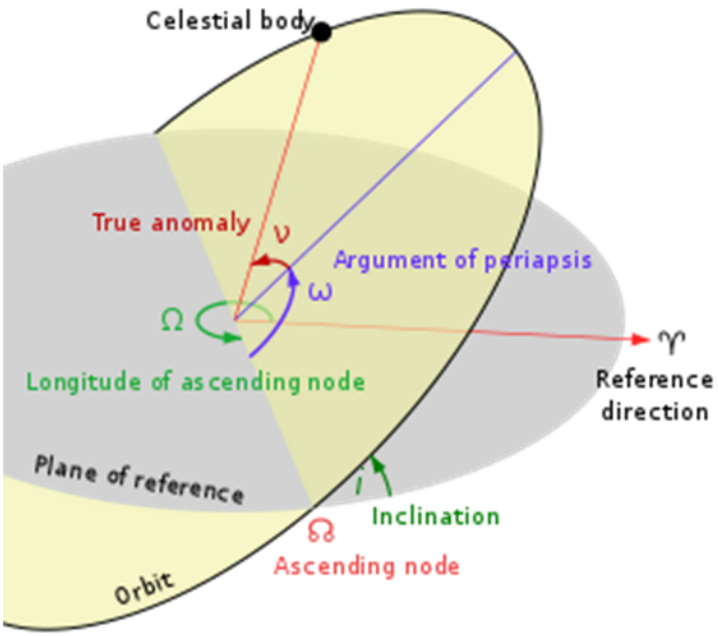


Figure 1.4: Classical orbital elements definition.

The set of orbital elements most commonly used is called *classical orbital elements*[12], which are defined by Fig. 1.4 as it follows:

1. *a semi-major axis*, defines the size of the conic section;
2. *e eccentricity*, defines the shape of the orbit;
3. *i inclination*, is the angle from the plane of reference to the orbital plane, or the angle between the angular momentum and the z-axis;
4. Ω *right ascension (longitude) of the ascending node* or *(RAAN)*, is the angle, measured in the fundamental plane, from the x-axis to the ascending node, a point where the satellite crosses the fundamental plane from the south to the north emisphere at the intersection with the orbital plane;
5. ω *argument of periapsis*, is the angle, measured in the orbital plane, from the ascending node to the periapsis of the orbit;
6. ν *true anomaly*, is the angle from the periapsis to the instantaneous position of the satellite in the orbit, measured at epoch t.

To avoid singularities, other elements shall be used when one of these classical elements cannot be defined. For example, the *longitude of periapsis* $\Pi = \Omega + \omega$ is used for equatorial orbits, the *argument of latitude at epoch* $u = \omega + \nu$ for circular orbits, the *true longitude at epoch* $\ell = \Omega + \omega + \nu = \Pi + \nu = \Omega + u$ if both circular and equatorial. Another orbital element often used in astrodynamics applications is the *mean anomaly* M_e in Eq.(1.10), used instead of ν when it is important to verify the simmetry of an orbit, regardless of its eccentricity.

Another set of orbital elements often used in astrodynamics is the set of Delaunay elements[12], used to describe the motion of a body when the equations of motion are written in the Hamiltonian form[13]. These elements are composed by a set of three "action" variables (L, G, H) derived from the momenta and three "conjugate angle" variables (l, g, h). The relation between the Keplerian orbital elements and the Delaunay elements is the following:

- $L = \sqrt{\mu a}$, related to the energy/size of the orbit;
- $G = L\sqrt{1-e^2} = \sqrt{\mu a(1-e^2)}$, the total angular momentum;
- $H = G\cos i = \sqrt{\mu a(1-e^2)}\cos i$, the z-component of the angular momentum;
- $l = M_e$, the mean anomaly;
- $g = \omega$, the argument of periapsis;
- $h = \Omega$, the longitude of the ascending node, which is equal to the right ascension of the ascending node when the reference frame is inertial, but it has to be corrected if the reference frame is body-fixed.

The classical or the canonical orbital elements are often used to verify if the orbit respects the hypothesis of the KR2BP, because only the true anomaly can change with time according to the theory. This is why analyzing the variation of the classical orbital elements can give us some information about the nature of orbital pertubations.

Orbital Perturbations

A perturbation is a deviation from an integrable system. It is utterly optimistic to think that in the universe the hypothesis of Newton is valid, even though at first glance celestial motion may seem schematic and predictable. The actual path of orbital motion will vary from the analysis of the KR2BP due to orbital perturbations such as the spherical asymmetries of the central body or the presence of other gravitational forces (called 3rd-body perturbations) or non-gravitational

forces, which are neglected in the Keplerian motion. Most of the perturbations that occur in the orbital motion of our interest are analytically tractable and those can be included in the equations of motion to obtain a more accurate representation of the trajectory. In the case of unpredictable perturbations, those should be treated in a stochastic (probabilistic) manner. Some of the perturbations which could be considered are due to the presence of other attracting bodies, atmospheric drag and lift, the asphericity of the Earth or Moon, solar radiation effects, magnetic, and relativistic effects. The study of perturbation analysis was necessary to accomplish orbital flight for artificial satellites, because orbital perturbations are exploited by mission analysts to save fuel utilization for orbit station-keeping by placing the satellite in specific orbits were the perturbations produce periodic stability of the trajectories (i.e. sun-synchronous orbits), but also because the extent of the perturbation must be assessed to evaluate the complexity of the position control system in the case the perturbation has the effect to drift away the trajectory from the desired orbit.

There are two main cathegories of perturbations analysis techniques. Those are referred to as *special perturbations* and *general perturbations*. Special perturbations are techniques which deal with the direct numerical integration of the equations of motion including all necessary perturbing accelerations. General perturbation techniques involve an analytic integration of series expansions of the perturbing accelerations. This is a more difficult and lengthy technique than special perturbation techniques, but it leads to better understanding of the source of the perturbation. In this section, only the special technique is discussed, as it is the most commonly used nowadays thanks to the incessant technological advancement on the computational power of computers.

The *Cowell's Method* is the simplest and most straightforward of all perturbation methods. It was developed by P. H. Cowell in the early 20th century and was used to determine the orbit of the eighth satellite of Jupiter. Cowell and Crommelin also used it to predict the return of Halley's Comet for the period 1759 to 1910. This method has been "rediscovered" many times in many forms. It is especially popular and useful now with faster and larger capacity computers becoming common. The application of Cowell's method simply consists in writing the equations of motion of the object being studied, including all the perturbing accelerationss, and then to numerically integrate them step-by-step. For the *Perturbed Kepler Restricted 2 Body Problem (PKR2BP)*, the equation would be:

$$\ddot{\vec{r}} + \frac{\mu}{r^3}\vec{r} = \vec{a_p} \tag{1.12}$$

For numerical integration this would be reduced to a system of first order

differential equations:

$$\begin{aligned} \dot{\vec{r}} &= \vec{v} \\ \dot{\vec{v}} &= -\frac{\mu}{r^3}\vec{r} + \vec{a_p} \end{aligned} \tag{1.13}$$

where $\|\vec{r}\|$ and $\|\vec{v}\|$ are the radius and velocity vector of a satellite with respect to the larger central body. For numerical integration equation 1.13 would be further written as a first-order system of ODE:

$$\begin{aligned} \dot{x} &= v_x \\ \dot{y} &= v_y \\ \dot{z} &= v_z \\ \dot{v}_x &= -\frac{\mu}{r^3}x + a_{px} \\ \dot{v}_y &= -\frac{\mu}{r^3}y + a_{py} \\ \dot{v}_z &= -\frac{\mu}{r^3}z + a_{pz} \end{aligned} \tag{1.14}$$

where $r = \sqrt{x^2 + y^2 + z^2}$. The perturbing acceleration is usually a function of time, position and velocity and therefore the differential equations need to be integrated numerically. If it is not possible to find an analytical function that is able to represent the perturbing acceleration, then approximations should be made, since our aim is to find a method to predict the trajectory which is the most accurate possible, but again there is no tool that is able to interpretate reality perfectly. Nonetheless, numerical integration is subject to rounding and truncation errors, typical of computers. In the following sections, an example of perturbing acceleration function is formulated in the case of interest of this dissertation, thus the perturbations occurring typically in Lunar orbits.

The main advantage of Cowell's method is the simplicity of implementation, because it is possible to consider any kind of perturbing acceleration if we are able to approximate it with an analytical function. The main disadvantage with respect to other perturbation analysis techniques (i.e. *Encke's method*[10] or *Variation of elements method*) is the solving speed of the computation, due to the necessity of small integration step size to achieve better accuracy. Another drawback of this method is the sensitivity to round-off and truncation errors, which even double precision computer arithmetic could not permanently reduce.

Eq.(1.14) are written in cartesian coordinates within an inertial coordinate system, which must be carefully chosen unless centrifugal and Coriolis forces are

included in the equation of motion. To help a faster computational speed, those equations are often rewritten in polar coordinates, because angles vary slower, leading to less errors and allowing for larger integration step size. The spherical coordinates (r, θ, ϕ) must be written in an equatorial coordinate system; thus the equation of motion becomes:

$$\begin{aligned} \ddot{r} - r(\dot{\theta}^2 \cos^2 \phi + \dot{\phi}^2) &= -\frac{\mu}{r^2} \\ r\ddot{\theta} \cos\phi + 2\dot{r}\dot{\theta} \cos\phi - 2r\dot{\theta}\dot{\phi} \sin\phi &= 0 \\ r\ddot{\phi} + 2\dot{r}\dot{\phi} + r\dot{\theta}^2 \sin\phi \cos\phi &= 0 \end{aligned} \tag{1.15}$$

We must always choose the appropriate coordinate system depending on the application and the type of analysis that we are conducting.

Choosing the right numerical integration method is critical to ensure the appropriate accuracy of the solution, meaning that a wrong integration method could lead to meaningless results, regardless of the accuracy of the analytical foundations of the equation of motion. The goal is to select a method to accomplish higher speed of computation, higher accuracy of the solution, lower data storage and lower complexity of the algorithm. To do so, the following selection criteria must be evaluated:

- The step size must be as large as possible;
- Variable step size makes the algorithm simpler and faster;
- The computing time must be small;
- It must be verified that the error doesn't grow exponentially;
- It must be insensitive to round-off errors;
- It should have a maximum and minimum control over the truncation error;

The desirables qualities cannot be accomplished all simultaneously, because they may be in opposition to each other, therefore the most suitable integration method depends on the problem we are trying to solve and the solution we expect from it. The round-off errors arise from the limitation of computers to store only a finite amount of decimals to represent irrational numbers, thus this kind of error accumulates during the integration. To prevent it, we must choose a method that converges to the solution in the lowest number of integration steps as possible. The truncation error is the result of an inexact solution of the differential equation approximation: the computer solves a differential equation by *difference* operations

of certain series expansion to approximate the function. The truncation error depends on the degree at which the series expansions are interrupted, or truncated. The larger the step size, the larger the truncation error, so this is in opposition to the reduction of round-off errors. We could say that round-off errors are a function of the machine, while the truncation errors are dependant on the method chosen, thus it is unavoidable to have errors in numerical integration and we can only take measures to reduce and limit them.

The next section shifts the focus on the Lunar orbits. To analyze the motion of an artificial satellite around the Moon, and to integrate the trajectory equation, it is necessary to understand the dynamics of the Moon's motion. Moreover, to be allowed to write and solve numerically the PKR2BP, it is necessary to define a conventional reference frame where the hypothesis of the dynamics model are valid, and therefore we need to derive analytically the expression for the perturbing accelerations that often occur in the proximity of the Lunar surface. For Earth orbits, the most relevant perturbations are the atmospheric drag, the non-spherical Earth and the Solar Radiation Pressure. For Lunar orbits, the following section describes the *Lunar Gravity Geopotential Model* and the *Earth's Tidal Acceleration*.

1.1.2 Lunar Orbits

Before delving into the analysis of artificial satellites in orbit around the Moon, it is important to describe the peculiarities of the Moon's motion around the Earth and the complexity of predicting its position in space due to perturbations. Because the hypothesis of the KR2BP are not verified, we need to understand the reasons; this process goes by understanding the gravitational environment in which the Moon is in motion: the Earth-Moon system.

The Moon is the only natural satellite orbiting around the Earth, but it is more correct to state that the Earth and the Moon both co-rotate around their center of mass. The mean distance between the two bodies is 384000 km and the mass of the Moon is around 1/81.3 times of the mass of the Earth; this means the center of mass is located 4671 km away from the center of the Earth. The orbital period of the Moon is not constant but is slowly increasing at the same time the distance between the Earth and Moon is increasing. This is because Earth's tides are rotated eastward by Earth's rotation, and the tidal bulge shifts the center of gravity from the center of mass, causing the Moon to spiral outward[14].

The position of the Moon can be described at any time by the following 6 elements: the semi-major axis a, eccentricity e, inclination i, longitude of the ascending node Ω, argument of perigee ω and right ascension at epoch α. The first

5 are already defined in the previous section as the classical orbital elements, the right ascension at epoch is the angle measured eastward from the vernal equinox to the projection of the Moon's position vector on the equatorial plane of the Earth, as shown in Fig. 1.5.

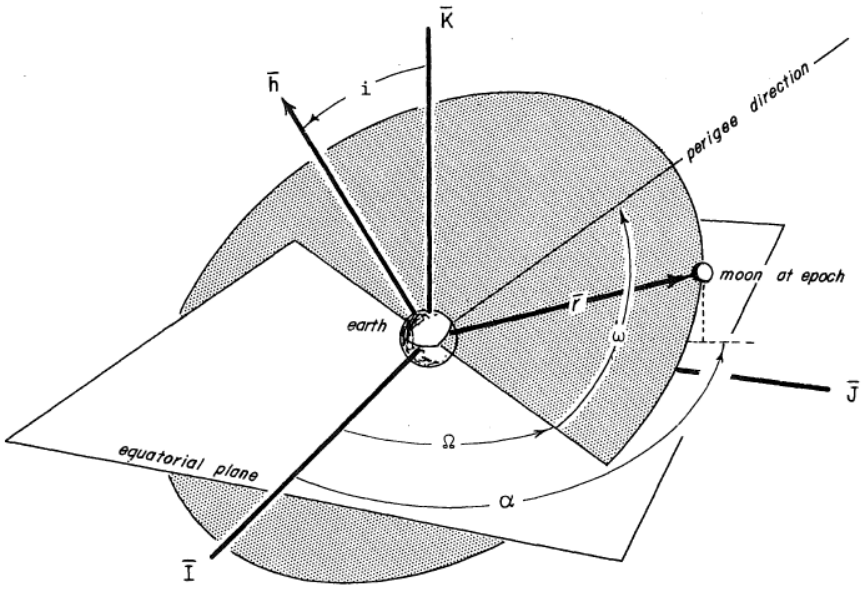


Figure 1.5: Moon's orbital elements representation[10].

Due to the perturbative effect of the Sun, these orbital elements are not constant, but only their average value over time can be evaluated. For the values at a given epoch, accurate ephemeris are constantly updated by NASA[15]. The Table 1.3 summarizes the average values of the Lunar orbital elements, as well as Moon's characteristics.

As mentioned earlier, Sun's perturbation leads to four fundamental frequencies in the rate of change of the orbital elements: the lunar sidereal month is $2\pi/\omega_{\leftmoon} \approx 27.322\,days$; the precession of the longitude of the pericenter in the ecliptic plane is $2\pi/\varpi_{\leftmoon} \approx 8.84\,years$; the precession of the longitude of the ascending node in the ecliptic plane is $-2\pi/\dot{h}_{\leftmoon} \approx 18.6\,years$; the Solar year is $2\pi/\dot{l}_{\odot} \approx 365.25\,days$ [16]. Another peculiar characteristic is the Lunar librations: the Moon's period of revolution is equal to the its period of rotation around its axis, therefore we should always see the same face of the body pointing towards the Earth. In reality, the Moon's equator is inclined by 6.5 deg with respect to the orbit causing the libration in latitude and allowing us to face bigger portions of the north pole in the first half of the sidereal month, alterned by south pole in the second half of the month. Moreover, the small eccentricity causes the libration in

Property		Unit	Value
Mass	$M_{\leftmoon}$	$[kg]$	$7.34767309 \cdot 10^{22}$
Equatorial radius	$R_{\leftmoon}$	[km]	1737.4
Mean Period	$T_{\leftmoon}$	$[days]$	27.31661
Mean semi-major axis	$a_{\leftmoon}$	[km]	384400
Mean eccentricity	$e_{\leftmoon}$	-	0.054900489
Mean inclination (relative to the ecliptic)	$i_{\leftmoon}$	[deg]	5.13
Mean angular velocity	$N_{\leftmoon}$	$[rad/days]$	0.229968

Table 1.3: Moon's characteristics and mean orbital elements.

longitude, allowing us to see up to 7.5 deg more than a perfect synchronized rotation.

Now that the Earth-Moon system has been described, as well as the complexity of the Moon's orbit around the Earth, the next step in the process of deriving the trajectory of an artificial satellite in orbit around the Moon, it is necessary to define a reference frame in which the equation of motion can be expressed and integrated.

Selenocentric Reference Frames

The International Astronomical Union (IAU) defines a reference system as the "theoretical concept of a system of coordinates, including time and standards necessary to specify the bases used to define the position and motion of objects in time and space" and a reference frame as "practical realization of a reference system".[17]. To empower sustained exploration of the Moon, space agencies are cooperating with IAU to establish an International Lunar Reference Frame (ILRF) and ensure interoperability for the future of human missions on the Moon[18][19].
Until the international partners and organizations will demonstrate a formal definition of the latter, the coordinate systems that can be used to analyze the orbital dynamics in proximity of the Moon are the **International Celestial Reference Frame (ICRF)**, the **Mean-Earth Reference Frame (ME)**, the **Principal Axis Lunar Reference Frame (PALRF)** and the **Moon-Centered Inertial (MCI)**.

As showed in [20], the ICRF was determined by hundreds of measurements of extra-galactic radio sources (mainly quasars) observed by a Very Long Baseline Interferometer (VLBI). Its origin is at the baricenter of the Solar System, with the axes which do not show any rotation with respect to the observed quasars and therefore it was declared by IAU as the standard reference frame to define

the position of any astronomical object in the universe. The coordinates are the declination and the right ascension based on the mean celestial equator and the mean celestial equinox at the epoch of J2000[1]. Because the ICRF is inertial, all the body-fixed reference frames in the universe, and thus, the selenocentric coordinate systems, are computed by rotation angles with respect to the ICRF.

The ME is the traditional cartographic frame used since the 18th century to map the surface of the Moon. Its origin is located at the center of mass of the Moon, the mean direction of the Earth position vector identifies the x-axis (zero longitude), the mean direction of the Moon angular velocity determines the z-axis and the y-axis lies on the equatorial plane with the right hand-rule. The ME is body-fixed and therefore non-inertial. This reference frame is used to analyze spatial data, generate terrain and elevation analysis, and to reference surface geological features. For this reason, it is not used in orbital dynamics unless a Moon landing mission is planned.

The PALRF is the most common body-fixed coordinate system used in the dynamics and gravity field modeling. It is defined by the Moon's principal axes of inertia, in order to keep constant and diagonal the tensor of inertia in the computations. Its origin is at the center of mass of the Moon, the x-axis lies on the Moon's equatorial plane in the direction of the Lunar longest meridian and co-rotating with it, the z-axis is in the direction of the mean Moon's rotation axis, pointing towards the Moon's pole, the y-axis is found by the right-hand rule. The PALRF and ME frames are very similar, but they have a small, constant rotational offset from each other. The orientation of PALRF with respect to ICRF is shown in Fig. 1.6, and in order to compute a position vector in the PALRF we must apply a rotation matrix given by the Euler sequence 3-1-3, where the Euler angles ϕ, θ, ψ are calculated as:

$$\begin{aligned} \phi &= \alpha_0 + 90 \text{ deg} \\ \theta &= 90 \text{ deg} - \delta_0 \\ \psi &= W \end{aligned} \tag{1.16}$$

where α_0 and δ_0 are the right ascension and the declination of the North Pole of the Moon at epoch, whereas W is the longitude of the prime meridian with respect to the intersection of the ICRF equator and the Moon's equator, as specified by

[1]J2000 refers to the standard epoch of time, used as a fixed reference to define the orientation of the ICRF. The "J" stands for "Julian epoch", which means the time is computed in Julian years of 365.25 days. The J2000 in Terrestrial Time corresponds to the date 01/01/2000 at 12:00:00.

IAU working group on Coordinate and Rotational Elements[21]. The values of α_0, δ_0 and W are time dependent and the formulas to compute them with high accuracy are defined in [21] and summarized in Fig. 1.7, where the time interval is computed from the standard epoch, the J2000.

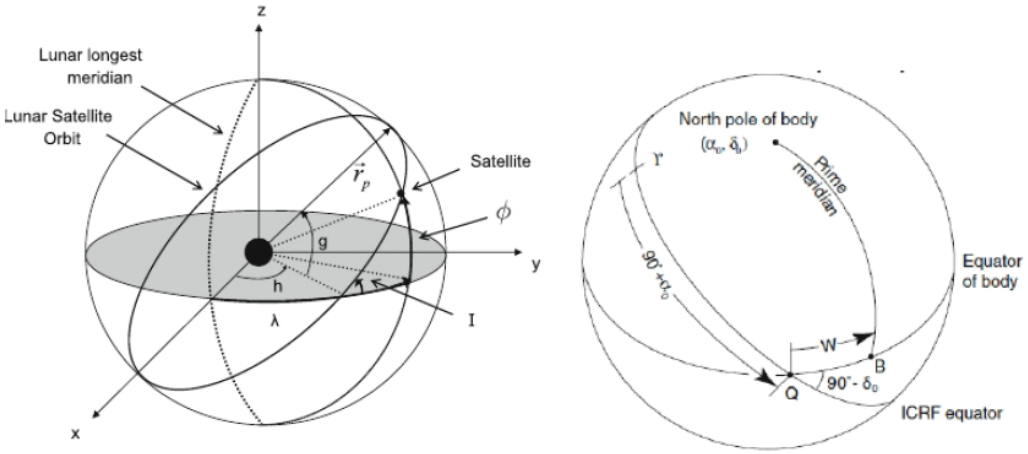


Figure 1.6: Selenocentric coordinates.

The MCI is the general term used to adress any non-rotating frame with the origin at the Moon's center of mass, in analogy with the ECI. On the Moon's proximity it is harder to identify non-rotating axes with respect to the fixed stars, because the rotational motion of the Earth-Moon system is complex. For this reason, the most common way to create an MCI is to choose an epoch (usually J2000) and "freeze" the PALRF axes with the purpose of integrating the perturbed Kepler's problem and find a trajectory which derives from correct orbital dynamics hypothesis. Another typical MCI reference frame to be used is the ICRF itself, because it's easier to be implemented in the numerical integration and NASA JPL defined the mathematical procedure to do the coordinate systems conversion between ICRF and PALRF[22], where the Moon's orientation is derived in the famous Development Ephemerides DE440 and DE441 which are constantly updated. NASA has also developed a tool for implementing this coordinate conversions in a numerical integration code, called *NASA SPICE Toolkit*, which can be downloaded at [23].

Lunar Gravity Geopotential Model

The most relevant perturbation when dealing with Lunar orbits' integration is the non-uniform distribution of the mass inside our only natural satellite. Due to the particular origin of the Moon, the planet presents the so-called *"Mascons"*, or Mass

α_0, δ_0 are ICRF equatorial coordinates at epoch J2000.0.
T = interval in Julian centuries (of 36525 days) from the standard epoch
d = interval in days from the standard epoch
The standard epoch is JD 2451545.0, i.e. 2000 January 1 12 hours TDB

Moon

$$\alpha_0 = 269^\circ.9949 + 0^\circ.0031T - 3^\circ.8787 \sin E1 - 0^\circ.1204 \sin E2 + 0.0700 \sin E3 - 0.0172 \sin E4 + 0.0072 \sin E6 - 0.0052 \sin E10 + 0.0043 \sin E13$$

$$\delta_0 = 66.5392 + 0.0130T + 1.5419 \cos E1 + 0.0239 \cos E2 - 0.0278 \cos E3 + 0.0068 \cos E4 - 0.0029 \cos E6 + 0.0009 \cos E7 + 0.0008 \cos E10 - 0.0009 \cos E13$$

$$W = 38.3213 + 13.17635815d - 1.4 \times 10^{-12} d^2 + 3.5610 \sin E1 + 0.1208 \sin E2 - 0.0642 \sin E3 + 0.0158 \sin E4 + 0.0252 \sin E5 - 0.0066 \sin E6 - 0.0047 \sin E7 - 0.0046 \sin E8 + 0.0028 \sin E9 + 0.0052 \sin E10 + 0.0040 \sin E11 + 0.0019 \sin E12 - 0.0044 \sin E13$$

where

$$E1 = 125^\circ.045 - 0^\circ.0529921d, \quad E2 = 250^\circ.089 - 0^\circ.1059842d, \quad E3 = 260^\circ.008 + 13^\circ.0120009d,$$

$$E4 = 176.625 + 13.3407154d, \quad E5 = 357.529 + 0.9856003d, \quad E6 = 311.589 + 26.4057084d,$$

$$E7 = 134.963 + 13.0649930d, \quad E8 = 276.617 + 0.3287146d, \quad E9 = 34.226 + 1.7484877d,$$

$$E10 = 15.134 - 0.1589763d, \quad E11 = 119.743 + 0.0036096d, \quad E12 = 239.961 + 0.1643573d,$$
$$E13 = 25.053 + 12.9590088d$$

Figure 1.7: The orientation of Moon's north pole and prime meridian after IAU[21].

Concentration, which are localized regions of higher density beneath the lunar surface. The Mascons have been created by strong impacts and collisions with asteroids and comets that created very large craters on some parts of the surface and more dense lumps on other parts of the surface. Thus, the Moon's shape is very far from being a perfect sphere, which is a deviation from the hypothesis of the KR2BP.

As investigated by [24] and [25], the gravity potential can be written as a series expansion of multipole harmonics, a typical approximation for potential fields such as electromagnetic and gravitational. A multipole expansion is a mathematical series representing a function that is dependent on angles, typically the longitude and latitude angles of a sphere. This series expansion is useful because it can be truncated when it is assumed the approximation is accurate enough. Combining the multipole expansion in angles with radius expansion, it is possible to represent a gravitational field in the three-dimensional space. The lunar gravity potential is described by the following expression:

$$V_{\leftmoon}(\vec{r}) = -\frac{\mu_{\leftmoon}}{r}\sum_{n=0}^{\infty}\left(\frac{R_{\leftmoon}}{r}\right)^{n}\sum_{m=0}^{n}P_{nm}(\sin\phi)\left[C_{nm}\cos m\lambda + S_{nm}\sin m\lambda\right] \quad (1.17)$$

where $\mu_{\leftmoon}$ is the Moon's gravitational parameter, $R_{\leftmoon}$ is the equatorial Moon's radius. The angles λ and ϕ respectively the longitude and latitude of the satellite, defined in Fig. 1.6, where r is the selenocentric satellite distance. As justified in [19], the Lunar gravity geopotential model is expressed in spherical coordinates in the PALRF. In order to express the Lunar gravity potential in cartesian coordinates of the PALRF, we must apply the following relations: $\sin\phi = \frac{z}{r}$, $\cos\phi = \frac{\rho}{r}$ with $\rho = \sqrt{x^2+y^2}$, $\cos\lambda = \frac{x}{\rho}$ and $\sin\lambda = \frac{y}{\rho}$. The functions $P_{nm}(x)$ are normalized Legendre polynomials of degree n and order m, defined in [26]. The coefficients C_{nm} and S_{nm} are the zonal ($m = 0$) and tesseral ($m \neq 0$) constants of the lunar gravity potential, which are provided by the GRAIL data[27][28][29]. The GRAIL mission was launched in 2011[30] and its purpose was to understand Moon's internal structure to accurately describe the gravitational field; for the first time the Mascons were identified and a high resolution gravitational model was formulated[31]. It is important to notice that the coefficients corresponding to $n = 0$ identify the point mass gravity, according to the KR2BP, while the data analysis shows that $C_{10} = C_{11} = S_{11} = 0$. Moreover, [24] and [25] describe the optimal truncation of the coefficients to represent with enough accuracy the Lunar gravity at each altitude of the Lunar orbits.

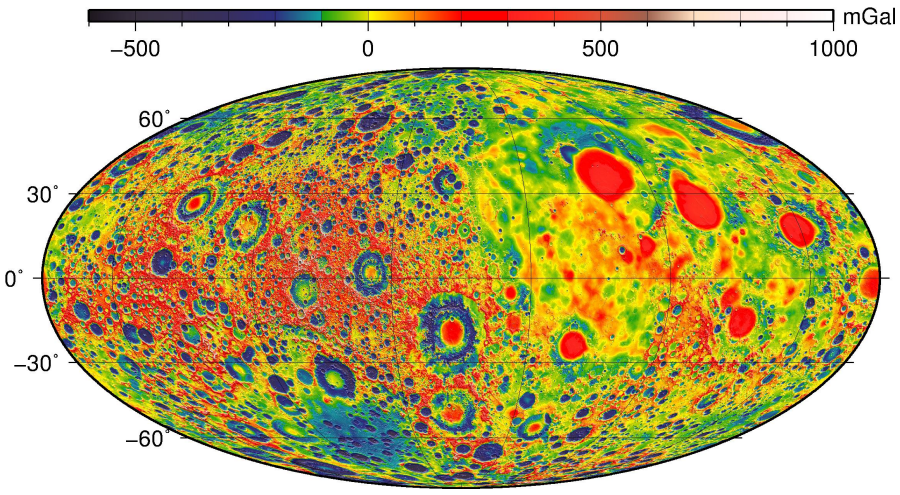


Figure 1.8: The gravity field of the Moon as measured by the NASA GRAIL mission[32].

To compute the perturbing acceleration from the potential, we must apply

$a_p = -\nabla V_{☾}(\vec{r})$. In spherical coordinates, the result of this calculus is $a_p = (a_r, a_\phi, a_\lambda) = -(\frac{\partial V}{\partial r}, \frac{1}{r}\frac{\partial V}{\partial \phi}, \frac{1}{r\cos\phi}\frac{\partial V}{\partial \lambda})$, where we have to substitute Eq.(1.17). Thus:

$$\begin{aligned} a_r &= -\frac{\mu_{☾}}{r^2}\sum_{n=1}^{\infty}(n+1)\left(\frac{R_{☾}}{r}\right)^n \sum_{m=0}^{n} P_{nm}(\sin\phi)\left[C_{nm}\cos m\lambda + S_{nm}\sin m\lambda\right] \\ a_\phi &= \frac{\mu_{☾}}{r^2}\cos\phi\sum_{n=1}^{\infty}\left(\frac{R_{☾}}{r}\right)^n \sum_{m=0}^{n} P'_{nm}(\sin\phi)\left[C_{nm}\cos m\lambda + S_{nm}\sin m\lambda\right] \\ a_\lambda &= \frac{\mu_{☾}}{r^2\cos\phi}\sum_{n=1}^{\infty}\left(\frac{R_{☾}}{r}\right)^n \sum_{m=0}^{n} m\cdot P_{nm}(\sin\phi)\left[S_{nm}\cos m\lambda - C_{nm}\sin m\lambda\right] \end{aligned} \tag{1.18}$$

where $P'_{nm}(x)$ is defined as $\frac{dP_{nm}(x)}{dx}$, with $x = \sin\phi$. The series with $n = 0$ has been neglected because it represents the gravitational attraction of the central body, which is already included in the KR2BP. To include this perturbing acceleration in the PKR2BP, it is necessary to transform the coordinates in the cartesian MCI reference frame.

Earth Tidal Acceleration

The Earth Tidal Acceleration describes the Moon's orbit perturbation due to the tidal interaction with the Earth and it is really common in the planet-satellite dynamics systems. The consequence of this interaction, as described in Sec.1.1.2, is that the Moon is gradually moving further away from the Earth of about 3.78 cm per year (orbital recession), and the Earth's rotation is slowing down by 2.3 ms per century (tidal breaking)[16]. The process can be described by a transfer of angular momentum: the Moon creates the ocean's tides due to its gravitational pull, the faster Earth rotation drifts eastward the tidal bulges helped by the friction between the ocean and surface beneath it. The shape of the Earth is no longer symmetrical and therefore the Moon's orbit is perturbed forward by it, since energy is being added to its orbit[14].

The Earth's Tidal Potential $V_\oplus(\vec{r}, t)$ is given by

$$V_\oplus(\vec{r}, t) = -GM_\oplus\left(\frac{1}{\sqrt{r^2 + r_\oplus^2 - 2\vec{r}\cdot\vec{r_\oplus}}} - \frac{\vec{r}\cdot\vec{r_\oplus}}{r_\oplus^3}\right) \tag{1.19}$$

where $r_\oplus(t)$ is the lunicentric PALRF radius vector of the Earth and $M_\oplus$ is the mass of the Earth. The potential can be approximated by a multipole expansion because the Moon's size is much smaller than the Earth's equatorial radius[33], but for numerical integrators it's sufficient to compute the perturbing acceleration from the exact formula. The procedure is similar to the calculus

of Eq.(1.18), the gradient is applied to the Earth's Tidal Potential with the difference that the vectors are already expressed in cartesian coordinates, therefore $a_p = (a_x, a_y, a_z) = -(\frac{\partial V}{\partial x}, \frac{\partial V}{\partial y}, \frac{\partial V}{\partial z})$. It yields:

$$\vec{a_p} = \mu_\oplus \left(-\frac{\vec{r} - \vec{r}_\oplus(t)}{|\vec{r} - \vec{r}_\oplus(t)|^3} - \frac{\vec{r}_\oplus(t)}{r_\oplus^3(t)} \right) \tag{1.20}$$

which becomes a "classic" third-body perturbing acceleration. Breaking the vector down into components, it yields:

$$\begin{aligned} a_x &= \mu_\oplus \left(-\frac{x - x_\oplus(t)}{|\vec{r} - \vec{r}_\oplus(t)|^3} - \frac{x_\oplus(t)}{r_\oplus^3(t)} \right) \\ a_y &= \mu_\oplus \left(-\frac{y - y_\oplus(t)}{|\vec{r} - \vec{r}_\oplus(t)|^3} - \frac{y_\oplus(t)}{r_\oplus^3(t)} \right) \\ a_z &= \mu_\oplus \left(-\frac{z - z_\oplus(t)}{|\vec{r} - \vec{r}_\oplus(t)|^3} - \frac{z_\oplus(t)}{r_\oplus^3(t)} \right) \end{aligned} \tag{1.21}$$

With the same procedure, even the Sun's third-body perturbations can be numerically implemented without any effort, which could make an orbital propagator more accurate but less efficient. For an accurate representation of the Earth's position vector in a numerical integration, the state-of-the-art ephemeris like DE440 are provided by NASA SPICE Toolkit [23].

Lunar Frozen Orbits

The previous sections have described the complex gravitational environment encountered by an artificial satellite in orbit around the Moon. For this reason, the orbital dynamics of Lunar orbits is often unstable and the osculating orbital elements of the satellite drift away from the initial conditions in only a few revolutions. For this purpose, multiple attempts have tried to find classes of stable orbits that can become suitable for orbital applications.

The Lunar orbits can be classified as it follows:*Low-Lunar-Orbits (LLO)* characterized by an altitude up to 500 km,*Medium-Lunar-Orbits (MLO)* ranging from 500 to 5000 km of altitude and *High-Lunar-Orbits (HLO)* with altitude above 5000 km[24]. These type of orbits can be analyzed using the PKR2BP, adding the perturbations discussed in Sec. 1.1.2 and sometimes adding the Sun's 3rd body perturbation and the Solar Radiation Pressure in extremely accurate integrators. Other particular type of orbits are found near the Lagrange points of the Earth-Moon system, defined as the points in space where the combined gravitational and centripetal forces of the Three-Body Problem compensate each other[34]. In the

Three-Body orbital dynamics, *Halo* and *Near-Rectilinear-Halo-Orbits (NRHO)* can be found, as well as *Distante Retrograde Orbits (DRO)*[35]. These type of orbits are dynamically stable, but they are too far from the Moon's surface to be interesting in the context of constellations in the terms of Moon's observation, but become useful in terms of navigation and communication with Ground Stations from Earth[36].

Several studies have pointed out the necessity to find stable orbits in LLOs. They all resulted in the definition of *Lunar Frozen Orbits (LFO)*, where the long-term drift of the eccentricity vector and the argument of periapsis are constant, or nearly constant[37]. In the frozen orbits, a particular combination of altitude, eccentricity and inclination is chosen in order to cancel out the average of the perturbations over a long period of time[38]. This process is called as "double-averaging method", a mathematical technique where the perturbation forces are averaged a first time over an orbital period, and the second time over a Moon's revolution period, in order to find the equations of the rate of change in the orbital elements. Then, the rate of change of the eccentricity and the argument of periapsis are forced equal to zero for the frozen condition to occur[39]. After the mean orbital elements that identify a frozen orbit are found, it is necessary to verify if these conditions are correct with a high-fidelity orbital propagator. Finally, an analytical transformation can be done to convert the mean orbital elements to precise osculating elements for even more accurate initial state definition[40]. The main source of perturbation to be averaged depends on the altitude of the orbit, in fact in LLOs the most relevant perturbation is the Lunar Gravity model, in HLOs the averaging technique is dominated by the Third-Body perturbations of the Earth. For this reason, HLOs double-averaging technique leads to high eccentricity results, called *Elliptical Frozen Lunar Orbits (ELFO)*[37]. These type of orbits are analyzed in [41] to create polar constellations where the argument of periapsis librates around a stable point. Finally, the numerical process to find candidates for LFOs is deeply investigated in [42].

A simple analytical model to find preliminary families of LFOs is described in [43], in which the dynamics is simplified with the Hill approximation[44][45]: the Earth's trajectory is assumed to be co-planar and circular with respect to the Moon's equatorial plane, and the rotational speed of the Moon is "tidally locked" with the Earth revolution. This means that the $\pm 5.5\%$ variation in the Earth-Moon distance, the $\pm 8\,deg$ librations of the Moon, and the 5.2 deg inclination of the Moon's equator with respect to its revolution plane are neglected. The analytical process, longly described in [43], consists in writing the perturbing potential under the Hill's problem approximation, than averaging the first time to cancel out the dependence on the mean anomaly (l) and the dependence on the tesseral and sectorial harmonics of the lunar gravity field, yielding:

$$\langle \mathcal{Z} \rangle_l = \frac{\mu_{\leftmoon}}{2a} \sum_{n \geq 2} C_{n,0} \left(\frac{R_{\leftmoon}}{a} \right)^n \frac{1}{2^{n-1} \eta^{2n-1}} S_n(e, I, \omega) \tag{1.22}$$

where $\eta = \sqrt{1 - e^2}$ is the eccentricity function, $C_{n,0}$ are the zonal coefficients ($m = 0$), while $S_n(e, I, \omega)$, after calling $n_2 = \mod(n,2)$, is defined as:

$$S_n(e, I, \omega) = \sum_{j=n_2}^{n-2} \tilde{\alpha}_{j,n} e^j \sum_{i=n_2}^{n} \tilde{\beta}_{i,n} \sin^i I \left[\frac{n_2 - 1}{2} \tilde{\gamma}_{i,j,0} + \sum_{k=n_2}^{i} \mathbb{i}^{k-n_2} \tilde{\gamma}_{i,j,k} \cos\left(k\omega - \frac{\pi}{2} n_2 \right) \right] \tag{1.23}$$

where i, j, k are summations with step 2, therefore $\mathbb{i} = \sqrt{-1}$ is always raised to an even number, solving the problem of having an imaginary part in the equation. The following helper math functions are defined:

$$\tilde{\alpha}_{j,n} = \frac{1}{2^j} \binom{n-1}{j}, \quad \tilde{\beta}_{i,n} = (2\mathbb{i})^{n-i} \frac{(n-1+i)!!}{(n-i)!!i!}, \quad \tilde{\gamma}_{i,j,k} = 2 \binom{i}{\frac{i-k}{2}} \binom{j}{\frac{j-k}{2}} \tag{1.24}$$

The double averaging cancels out the dependence on the argument of the ascending node (h), expressed in the rotating frame, but it doesn't change the averaged gravity potential. By doing so, the total averaged perturbing potential (zonal+Hill model) $\tilde{\mathcal{P}}$ becomes:

$$\tilde{\mathcal{P}} = \langle \mathcal{P} \rangle_{l,h} = \langle \mathcal{Z} \rangle_l + \frac{\mu_{\leftmoon}}{2a} \left(\frac{N_{\leftmoon}}{N} \right)^2 \frac{1}{8} \left[\left(2 - 3 \sin^2 I \right) \left(2 + 3e^2 \right) + 15 e^2 \sin^2 I \cos 2\omega \right] \tag{1.25}$$

where $N = \sqrt{\frac{\mu}{a^3}}$ is the mean motion of the spacecraft.

In order to derive an expression where it's possible to extract orbital elements that generate a frozen orbits family, it is necessary to express the perturbing potential as a function of the Delaunay orbital elements, described in Sec.1.1.1. In the Hill approximation, the conjugate angle h is modified becaused the reference frame is rotating with the Earth, therefore $h = \Omega - N_{\leftmoon}\, t$. To find the frozen orbit, it is necessary to evaluate where $\dot{g} = \dot{G} = 0$, a process that involves writing the equations of motion in Hamiltonian form[46]. The conclusion is that $\dot{G} = 0$ for $g = \pm \frac{\pi}{2}$, therefore the search for a frozen condition that allows the eccentricity and the inclination to remain secularly stable is restricted to a 1-dimensional numerical search in $\dot{g}$. It yields:

$$\dot{g} = N \left(\frac{N_{\leftmoon}}{N} \right)^2 \frac{3}{8\eta} \left[4\eta^2 + 5(e^2 - \sin^2 I)(1 - \cos 2g) \right] + N \sum_{n \geq 2} C_{n,0} \left(\frac{R_{\leftmoon}}{a} \right)^n \frac{\mathcal{S}_n^*(e, I, g)}{2^n \eta^{2n}} \tag{1.26}$$

where $S_n^\star$ are constructed from S_n simply by substituing the $\tilde{\beta}_{i,n}$ with the following function:

$$\Psi_{i,j,n} = \left(1 + j - i - 2n + \frac{i}{\sin^2 I} - \frac{j}{e^2}\right)\tilde{\beta}_{i,n} \tag{1.27}$$

The solution of $\dot{g} = 0$ can be searched with any root-finding method, by keeping in mind that the "negative e" solution is allowed by stating that, instead of flipping g in the equations from 90 deg to 270 deg, it is numerically more convenient to allow the negative eccentricity to exist thanks to $-e = e\sin\left(-\frac{\pi}{2}\right)$.

1.2 Earth Satellite Constellations

A satellite constellation is a network of satellites operating in coordinated orbits to provide a specific service or function that a single satellite could not provide. If the satellites are flying in the same orbit close to each other, it is rather called a *cluster* or *formation*[47]. One of the key aspects that led engineers to design satellite constellations for the first time is the need to provide continuous coverage of some regions of the Earth, therefore one satellite is not enough to accomplish mission goals and objectives. In the context of satellites constellations, coverage is defined as the ability of the system to provide service to a specified area on the planet's surface, which is achieved when one or more satellites are visible from any point of that area regardless of the visibility constraints[48]. Constellations are needed because it is possible to achieve global or near-global Earth coverage, continuous service in which at least one satellite is in line of sight with the ground target, higher revisit frequency because observation becomes more accurate, redundancy and reliability of the mission. The evolution of satellite systems is trending towards smaller and lower-cost satellites while keeping the reliability to high standards imposed by regulations, allowing to increase the number of Earth-orbiting constellations for observations, communications, navigation, and scientific purposes. Consequently, constellation design has become a challenging topic for both fundamental and applicative research, as constellations become more achievable and as the potential problems of collision avoidance and debris mitigation become more critical.

In general, it is not possible to affirm rules in the satellites constellation design, because the distribution of the spacecraft in orbit is strictly dependant on the mission goals. For this reason, satellites constellations are often labeled by the purpose of the mission, as shown in the Table 1.4, where some of the most famous examples of successful missions are listed. The year reported next to the mission operator is referred to the date of Full Operational Capability (FOC), meaning that all the satellites reached the operational orbits, that they have all been tested and the in-orbit operations have been completed. For example, the first launch

of a GPS satellite was declared in 1993, but all 24 satellites were available for the mission's purpose on December 8, 1995[49]. In order to understand the Table 1.4, it is necessary to specify the classification of Earth's orbits based on the altitude from the surface: Low-Earth-Orbits (LEO) range from 100 to 2000 km, Medium-Earth-Orbits (MEO) range from 2000 to 31570 km, Geostationary-Earth-Orbit (GEO) range from 35586 to 35986 km of altitude to match the mean rotation of the Earth, Inclined-Geostationary-Sun synchronous-Orbit (IGSO) are a particular GEO inclined from the equatorial plane to match also the revolution speed around the Sun[50]. We can realize from the table that many countries have commissioned their own navigation constellation (GPS, GLONASS, BeiDou, Galileo), needed for civilian and military purposes to locate the position of Earth's facilities with extremely accurate precision. Another mission goal of satellites constellations can be private telecomunication and internet providers such as Iridium, TDRSS and Starlink., as well as military comunications such as WGS. Moreover, Earth observation can provided by constellations like Meteosat, Sentinel and DMC, usually for meteorological forecast, environmental quality monitoring or forecast of natural disasters. Those are only the most representative examples, but studies indicate the number of satellites constellation could trespass the treshold of 10000 by 2026 [51].

Table 1.4: Examples of operative Earth Satellite Constellations[47].

Name	**Operator**	**Purpose**	**Orbit types**
Global Positioning System (GPS)	USSF (USA), 1995	Navigation	24 satellites in 6 planes, MEO
GLONASS	Roscosmos (Russia), 2011	Navigation	24 satellites in 3 planes, MEO
Galileo	EUSPA, 2016	Navigation	24 satellites in 3 planes, MEO
BeiDou Navigation System	China, 2020	Navigation	24 satellites in 3 planes MEO, 3 sats GEO and 3 sats IGSO
Iridium	Motorola (USA), 1998	Communication	66 satellites in 6 planes, LEO

Next Page

Table 1.4 – continuation from previous page.

Colonna 1	**Colonna 2**	**Colonna 3**	**Colonna 4**
Starlink	SpaceX (USA), 2020	Communication	over 5000 satellites in LEO
Wideband Global SATCOM (WGS)	USSF (USA), 2008	Military Communication	10 satellites in GEO
MeteoSat Second Generation	EUMETSAT (EU), 2004	Earth Observation	4 satellites in GEO
Disaster Monitoring Constellation (DMC)	DMC International Imaging, 2002	Earth Observation	4 satellites in LEO
MUOS (Mobile User Objective System)	USSF (USA), 2019	Military Communications	4 satellites in GEO
TDRSS	NASA (USA), 1983	Communication	10 satellites in GEO
Copernicus / Sentinel	ESA (EU), 2014	Earth Observation	5 satellites in LEO, 1 sat in GEO

For instance, a random distribution of satellites in space could guarantee the satisfaction of the mission goals, if system redundancy is enough. In reality, it is relevant to mention that the purpose of the constellation is often the main driver of its design, and usually a Performance Vs. Cost analysis is conducted to choose the constellation parameters, where the performance capabilities are often measured in terms of coverage percentage, but at any occasion other Figures of Merit could be analyzed. For example, a constellation used for GNSS (Global Navigation Satellite Systems) needs at least 3 or 4 satellites visible at the same time from the ground station, and there is often a need for continuous global coverage. This is why the number of satellites is considerably high, the satellites are distributed in more than one orbital plane, and the altitude of the orbit is usually MEO ($\approx 20000\,\text{km}$) with carefully chosen inclination. For communications services, a LEO constellation will need thousands of satellites (like Starlink) to guarantee signal for the whole world, in MEO a few dozens could be enough, in GEO the number significantly decreases to 4-5 only. On the other hand, despite the cost of the systems is reduced linearly with the number of satellites involved, other kinds of costs become relevant, such

as the launch cost to bring a satellite in GEO or the complexity of the radiation shield in MEO.[2]



Figure 1.9: Artistic representation of the GPS constellation.

Since the constellations' size and structure strongly affect system cost and performance, we must carefully assess alternative designs and document the reasons for trades which are made. The trade-off analysis allows the constellation design process to continue in order to achieve the system objectives at minimum cost and risk. While there are no rules, there are a number of key issues which dominate constellation design trades, as listed in Table 1.5. Because virtually any multi-satellite system will be inherently expensive, all constellation design trades are ultimately based on cost vs. performance. Therefore, it's crucial to identify the constellation design aspects that affect the cost, the performance, or both. The Table describes the main issues that occur in the design process, why they influence the performance and cost analysis, and they are defined as it follows: **coverage** is the portion of the planet's surface that is accessible in a determined period of time by the payload of the spacecraft. It is usually the main objective of any space mission and figure of merit for the performance analysis; the **number of satellites** is the major cost driver of the constellation. On the contrary, increasing the altitude

[2]MEO satellites orbit inside or near the Van Allen radiation belts, regions of high-energy charged particles trapped by Earth's magnetic field. This exposure demands robust radiation shielding, radiation-hardened components, and careful mission planning to protect systems and extend satellite lifetime.

while aiming at a constant coverage determines a lower number of satellites; **launch requirements** depend on the altitude of the selected constellation. Placing your satellites in multiple orbital planes will increase the number of launches needed to move the constellation into an operational status, and the cost of the mission will increase accordingly; the **space environment** is a key issue in the cost of the subsystems of the spacecraft, and it depends on the altitude and inclination of the orbit; **orbital perturbations** are dynamic effects of the environment which modify the desired trajectory of the spacecraft obtained in the KR2BP, as already described in Sec. 1.1.1. Typical perturbations in LEO are atmospheric drag, J2 effect and solar pressure, which increase the cost of the attitude and orbit control system; **collision avoidance** is the key issue for constellations, because multiple satellites are required to cross the intersection points of the orbital planes. The more planes are involved, the more risk is involved in the mission, therefore it is critical to design the entire system; the **constellation deployment** is the process of placing each satellite in the desired orbit and it's not an easy task when the number of satellites is high. The **replenishment** is the process of keeping the constellation in a complete status, replacing failed satellites or ensuring redundancy. The **end-of-life** is the process of removing the satellites from the nominal orbit, choosing between a de-orbit in the atmosphere or a graveyard orbit. These processes influence the operational cost of the mission; the **number of orbit planes** is critical because it causes high operational costs related to launch and build-up, higher mission risk due to increased possibility of collisions but it definitely provides better coverage options. A more comprehensive definition and a mathematical analysis of the coverage, and satellite relative motion is done by Wertz[47].

Table 1.5: Constellation design aspects based on a performance vs. cost analysis.

Issue	**Why important**	**What determines it**	**Principal options**
Coverage	Principal performance figure of merit	Altitude, minimum elevation angle, inclination, geometry pattern	Choose the gap times for discontinuous coverage, or the minimum number of satellites in view for continuous coverage

Continues in the next page

Table 1.5 - continuation from previous page.

Issue	**Why important**	**What determines it**	**Principal options**
Number of Satellites	Principal cost driver	Altitude, minimum elevation angle, inclination, geometry pattern	Altitude, minimum elevation angle, inclination, geometry pattern
Launch Options	Major cost driver	Altitude, inclination, spacecraft mass	It is preferable to minimize altitude and inclination
Environment	Radiation level requirements	Altitude, eccentricity	Choose between staying below, in or above the Van Allen Belts
Orbit Perturbations (Stationkeeping)	Propulsion system requirements	Altitude, inclination, eccentricity	Keep all spacecraft at the same altitude
Collision Avoidance	Possibility to destroy the constellation	Geometry pattern, orbit control	Major design driver, you must avoid collisions
Constellation Build-up, Replenishment, and End-of-Life	Determines the mission lifetime	Altitude, geometry pattern	Sparing: on-orbit spares vs. launch on demand; End-of-Life: deorbiting vs. graveyard orbit
Number of Orbit Planes	Determines performance plateaus	Altitude, inclination	It is preferable to minimize the number of planes for better degradation

1.2.1 Coverage in adjacent planes

Before discussing the costellation patterns, it is important to define some parameters that are used to describe the geometry of constellations, and make possible a mathematical description of the relative motion in a constellation. As mentioned in Table 1.5, the key design performance parameter of a constellation is the coverage

capability. With the purpose of analyzing the total performance, we need to analyze mathematically the coverage capability of a single spacecraft and the overlapping coverage regions of adjacent spacecraft. Two spacecraft can be considered adjacent if they fly in succession following the same orbit, or if they belong to different orbital planes that are close enough for their coverage areas to overlap. This configuration is called as "Street of Coverage", and it gives name to a particular cathegory of constellations.

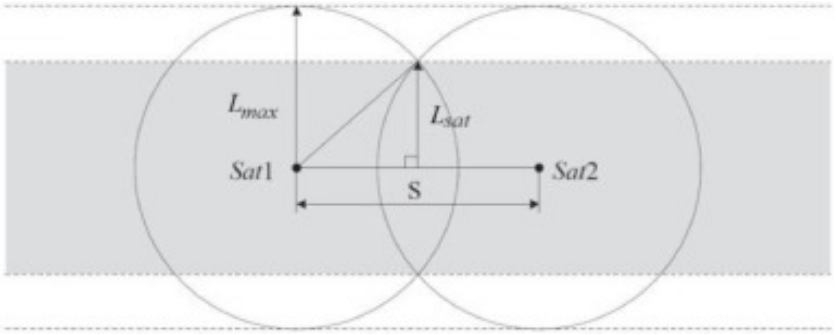


Figure 1.10: Street of Coverage geometric representation.

If we consider N satellites equally spaced at $S = 360/N$ deg apart in a given orbital plane and with L_{max} being the maximum central angle, defined as the angular radius of a satellite's ground coverage circle, measured with respect to Earth's center, there will be intermittent coverage throughout a swath of half-width L_{max}. If $S > 2L_{max}$, the coverage is intermittent throughout the entire swath. If $S < 2L_{max}$, a narrower area is formed where the coverage is continuosly provided because there is always overlapping of the two spacecraft's swaths. This area is called "Street of Coverage", it is centered on the ground trace and of width $2L_{street}$. The width is easily obtainable by applying geometric relationships of adjacent circles with two intersection points, and it yields:

$$\cos L_{street} = \frac{\cos L_{max}}{\cos(S/2)} \tag{1.28}$$

One way to cover the intermittent coverage gaps that appear outside of the SoC, is to carefully select an adjacent orbital plane with satellites in the same direction of motion, then the "bulge" in one orbit can be used to offset the "dip" of the adjacent orbit, as shown in Fig. 1.11.

In this case, the maximum perpendicular separation, D_{maxS}, between orbit planes with continuous coverage is:

$$D_{maxS} = L_{street} + L_{max} \quad \text{(same direction)}. \tag{1.29}$$

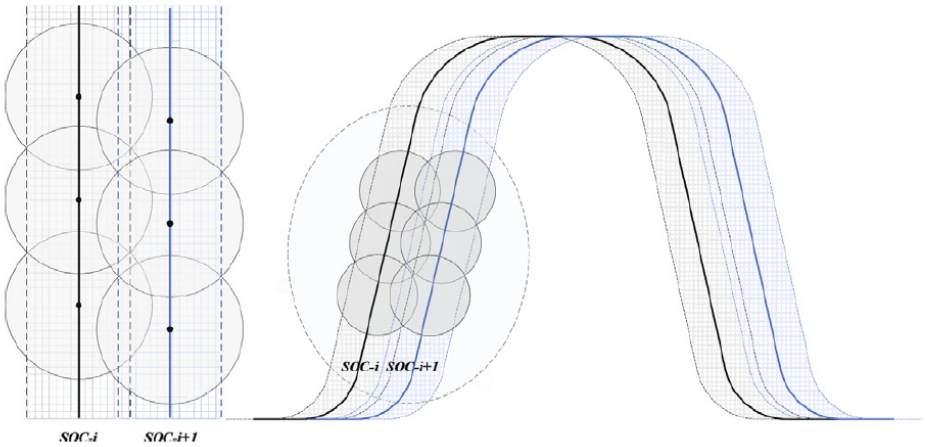


Figure 1.11: Streets of Coverage geometries of adjacent orbital planes.

If the satellites are moving in opposite direction, the bulge and the dip cannot be made to continuously line up, therefore:

$$D_{maxO} = 2\,L_{street} \quad \text{(opposite directions)}. \tag{1.30}$$

The equations above are correct only in terms of perpendicular separation distance. This means the situation for which the distance between the two orbital planes is maximum is verified only twice along the orbits, in particulare 90 degrees apart (in both directions) from the intersection points of the two adjacent planes. For most constellations, all the orbital planes will have the same inclination in order to mantain the same node rotation rate. Consequently, the relevant constellation parameters to define are the *ascending node angular spacing* ΔN, the common *inclination* of the orbits i, and the *relative inclination* i_R. The relative inclination is defined as the angle at which the orbits of the two planes intersect, which is also the angular separation between the orbital planes, measured at 90 degrees from their intersection. To better understand the definition of these parameters, the Fig. 1.12 represents a 3-dimensional representation of adjacent orbital planes with their geometric relationship[47].

From Fig. 1.12 it is possible to determine the relationship between i_R, ΔN and i:

$$\sin(i_R/2) = \sin(\Delta N/2)\,\sin i \tag{1.31}$$

Similarly, we define the *phase offset*, $\Delta\phi$, between two orbits as the difference in path length along the two orbits from the nodes to the point at which the orbits intersect. Applying the geometric relationships of spherical triangles, it yields:

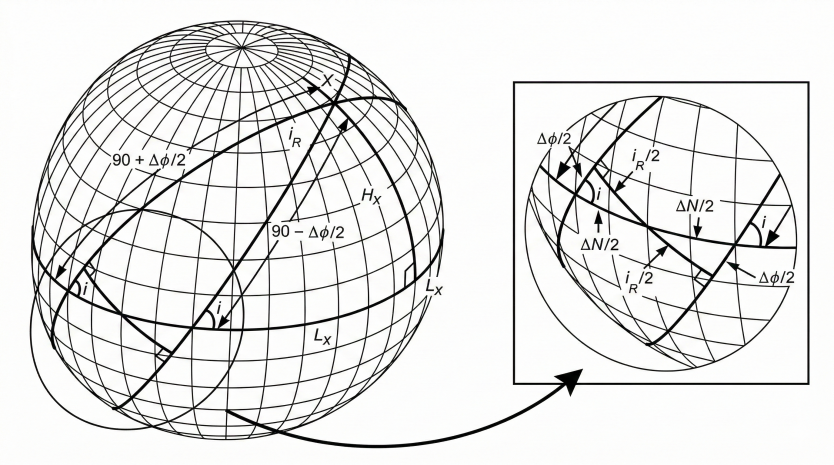


Figure 1.12: Relative geometry between two orbital planes at the same inclination.

$$\tan(\Delta\phi/2) = \tan(\Delta N/2)\,\cos i \tag{1.32}$$

It is importante to notice that the maximum spacing between two orbit planes, defined in Eq.(1.29) and Eq.(1.30), is equal to the relative inclination i_R. Thus:

$$D_{max} = i_R \tag{1.33}$$

These relationships are helpful when some of these variables are determined by mission requirements, yielding to a simple definition of constellation parameters. Other useful relationships determine the longitude and latitude of the intersection point between the orbits:

$$L_x = 90\,\text{deg} - \Delta N/2 \tag{1.34}$$

$$\tan H_x = \cos(\Delta N/2)\,\tan i \tag{1.35}$$

A particular combination of the aforementioned parameters defines a constellation pattern cathegory.

1.2.2 Constellation Patterns

This section is dedicated to list the most common patterns used by mission analysts in the last decades until today, on Earth. The examples written in Table 1.4 have highlighted the diversity of both constellation patterns and methods of analysing them. Conceptually, we want to reduce the alternatives to a few regular geometric patterns, so that the number of satellites would decrease as the altitude increases.

In fact, the coverage area provided by one satellite is larger if the satellite is in a higher orbit. Unfortunately, the problem is more complex than that, because multiple mission requirements are in conflict with each other and the solution is not unique for a particular set of conditions to be met. In principle, specifying a constellation pattern means specifying the number of satellites and the six orbital elements for each of them. Thus, the process of constellation design is the process of filling an $n \times 6$ matrix where n is the number of satellites and 6 are the degrees of freedom of a free-flyer in 3-dimensional space. In practice, the problem can be simplified looking for geometrical simmetries, locking some parameters. For example, if all the satellite are flying the same orbit, 5 orbital elements will be equal to all the spacecraft, whereas the true anomaly will be a parameter to be designed for each satellite (but in practice it's convenient to distribute the satellites evenly spaced along the trajectory, therefore we would need to know only the true anomaly of one satellite to know the others). In addition, the *swath width* and the *minimum working elevation angle* is a key element of constellation design and should be specified as a constellation parameter, although this is rarely done. The swath width is defined as width of the ground-track covered by a satellite's sensor as it passes over the Earth's surface. In other words, it's the projection on the Earth's surface of the sensor's FOV and it determines the total area that can be covered and the revisit time of the satellite. The minimum working elevation angle is a constraint of the swath width, as it is the lowest angle above the horizon at which the ground location can be accessed by the satellite for the coverage computation, and usually the value ranges from 5 to 10 degrees[52]. It follows a classification of common constellation patterns and the parameters involved in the design.

Geosynchronous Constellations

A geosynchronous constellation is a set of satellites placed in a geosynchronous orbit (GSO), meaning that the orbital revolution of every spacecraft matches the Earth's rotational period ($23\,h\ 56\,min\ 4\,s$, or one sidereal day). This type of constellation is used to provide global Earth coverage without time gaps between observations. To have the orbital period equal to a sidereal day it means the semi-major axis of the orbit is close to 35786 km of altitude. If the eccentricity and the inclination of the orbit is 0, the orbit is called geostationary. In this way, the satellite's coverage area for a GSO is constant in time.

Geosynchronous constellations are used for communications, such as TDRSS, weather coverage and even to track LEO satellites. They require very few satellites, for example 3 spacecraft in a single geostationary orbit equally spaced by 120 deg. Unfortunately, these constellations are in very high energy orbits (around $-4.7\,MJ/kg$) and the best coverage is only for equatorial and mid latitude regions,

while northern latitudes (the most populated) are often poorly covered.

Streets of Coverage Constellations

A Streets of Coverage (SoC) constellation is a type of satellite constellation in which spacecraft orbiting in adjacent planes are spaced so that their ground coverage swaths are lined up side by side, like parallel streets. To design this constellation, we need to distribute n satellites over m orbital planes to provide continuous global coverage. The best type of orbit to accomplish this goal is a polar or quasi-polar orbit in order to minimize the amount of planes needed. A polar orbit is defined as the orbit in which a satellite passes above the both poles of the planet at each revolution, formally identified by an orbital inclination of 90 deg[11].

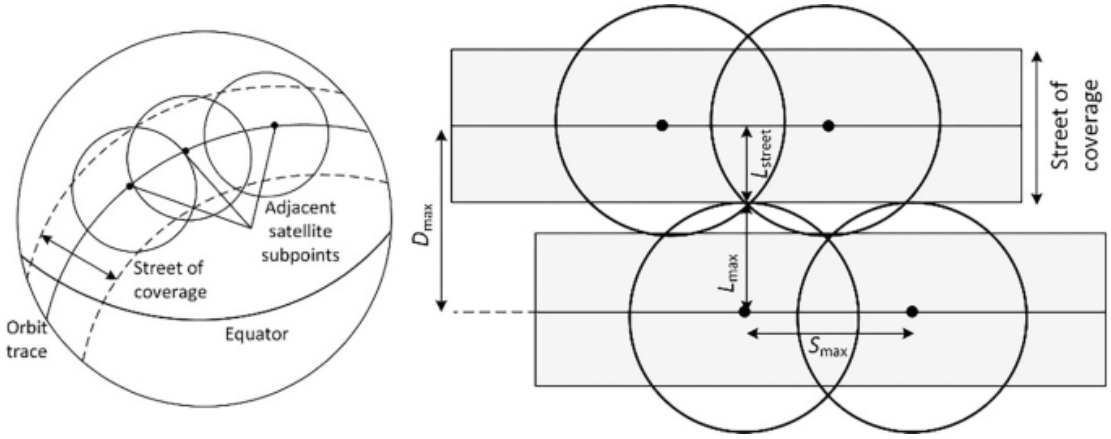


Figure 1.13: Design of a Streets of Coverage constellation.

Each orbital plane contains several satellites evenly spaced along the trajectory, whereas adjacent placed are phased by a node shift. In order to provide global continuous coverage for a streets of coverage pattern using m planes of polar orbit, we must have:

$$(m+1)L_{street} + (m-1)L_{max} > \pi \tag{1.36}$$

where L_{street} is the width of the coverage street created by two adjacent satellites in the same orbital plane and L_{max} is the maximum swath width provided by the payloads of the spacecraft. As shown in the Fig. 1.13, the condition $L_{street} < L_{max}$ is always verified, unless the two satellites are located in the same spot, which is not convenient.

Looking at the distribution of the orbital planes from the north pole of the planet, we can easily derive the Eq.(1.36), taking into account that in order to provide global coverage the angular space occupied by the total swath of the streets of coverage of each plane must be at least 180 degrees, because the other portion of the seam is covered by the same planes by the satellites below the ascending node.

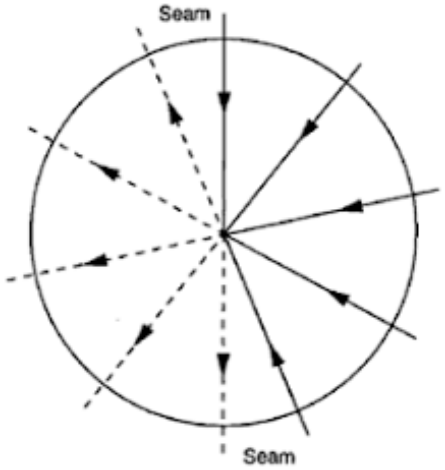


Figure 1.14: View of a Street of Coverage constellation seen from the north pole.

Notice that it is the swath width and not the altitude which determines the number of orbital planes and ultimately the number of satellites required to provide global coverage. Therefore we can affirm that the most critical drawback of SoC is that coverage does not vary continuously and smoothly with the altitude. Conversely, it is possible to verify discrete jumps in coverage which depend primarily on the swath width of the single spacecraft, but also on the minimum elevation angle (a ground constraint). Another drawback highlighted by Fig. 1.14 is the presence of a unique point of intersection for all the orbital planes. This increases the collision probabilities and as a result we must design more carefully the phase shift between adjacent satellites. This type of constellation is very efficient and it provides overall good overlap of swaths, but the ability of over-coverage of the poles must be exploited especially if needed by the mission requirements.

Walker Constellations

The Walker Constellation is the most symmetrical type of the satellites patterns and it gives its name after John Walker, who conducted an extensive study of their properties from the 1960s to the 1980s[53][54].

A Walker Constellation is usually defined by the notation:

$$(i : T/P/F)$$

where i is the inclination of the orbits, T is the total number of satellites of the constellation, P is the number of orbital planes and F is the relative phase factor. To achieve simmetry, the ascending nodes of each plane are uniformly distributed around the equator at intervals of $360\,\mathrm{deg}/P$ of longitude; within each orbital plane, the satellites are uniformly distributed at intervals of $360\,\mathrm{deg}/S$ where $S = \frac{T}{P}$ is the number of satellites in one plane. In order to describe the F factor accordingly, we define the *phase difference* $\Delta\phi$ as the angle in the direction of motion from the ascending node to the nearest satellite at a time when another satellite is crossing the ascending node of the next most westerly plane. In conclusion, if we need to create simmetry among all the planes, $\Delta\phi$ has to be an integral multiple F of $360\,\mathrm{deg}/T$, and therefore F can be any integer from 0 to $P-1$.

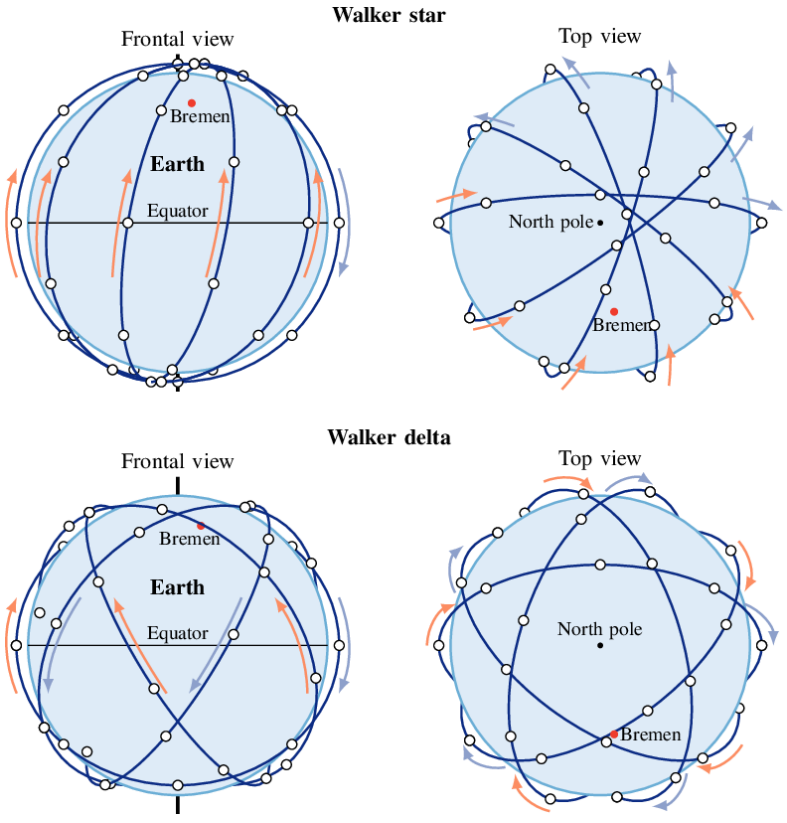


Figure 1.15: Walker Constellations: star and delta configuration.

The most common types of Walker patterns are the **Walker delta**, **Walker star** and **Hybrid/custom** patterns. In the Walker delta, the satellites are evenly

spaced in both RAAN (along the longitude) and true anomaly (along the orbit), allowing for regular phasing across planes. All the orbits are circular, with the same inclination and the same altitude. It provides global or near-global coverage, and for this reason it's the most common Walker constellation (i.e. the GPS and Galileo constellations)[53][55]. In the Walker star pattern, the RAANs are not evenly spaced, but rather create a symmetric pattern at the poles. The intersection of the planes appears near the poles, creating a star-like shape if viewed from above. Satellites are usually placed at polar or sun-synchronous inclinations, to achieve better coverage of polar regions, but leading to more complicated ground-tracks[53][55]. Finally the hybrid/custom patterns are particular configurations optimized to satisfy specific mission objectives. Some examples are the Inclined Walker constellation (it maximizes coverage of mid-latitudes, from 45 deg to 60 deg), Elliptical Walker constellation (uses Molniya orbits) or Multi-shell Walker constellations (several Walker constellations at different altitudes).

The best advantage of Walker constellations is the complete symmetry and that there is only a finite amount of combinations that comply with the definition, making the analysis and investigation much easier. For this reason the Walker patterns have gained popularity among mission analysts and the most used for mission design.

Elliptical Orbit patterns

Elliptical orbits constellations are used to provide prolonged coverage of northern latitudes which cannot be successfully served from geosynchronous orbits. The first example of the type of constellation was the Molniya constellation, a set of highly elliptical orbits used by former Soviet Union for communication and surveillance[56].

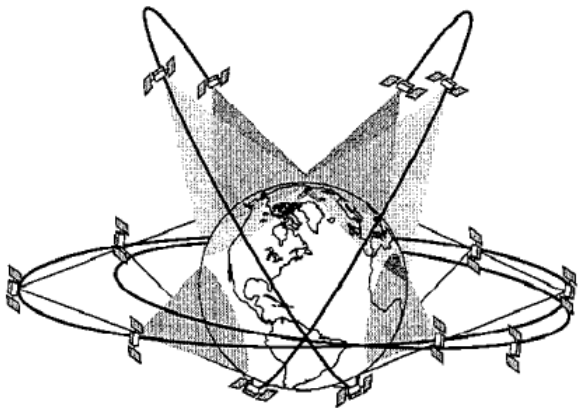


Figure 1.16: Elliptical orbits constellation example[47].

Elliptical orbits have the advantage to provide an additional free parameter to optimize the constellation performance in terms of coverage of specific latitudes, longitudes and times of day, because the altitude of the satellite varies drastically within a single revolution. The penalty for this freedom is the increase of the spacecraft's complexity, because the relative distance and attitude between satellites is harder to determine. Furthermore, elliptical orbits on Earth cross the Van Allen Belts for the majority of the orbital period, forcing the designers to add extensive radiation shielding.

Other Constellation patterns

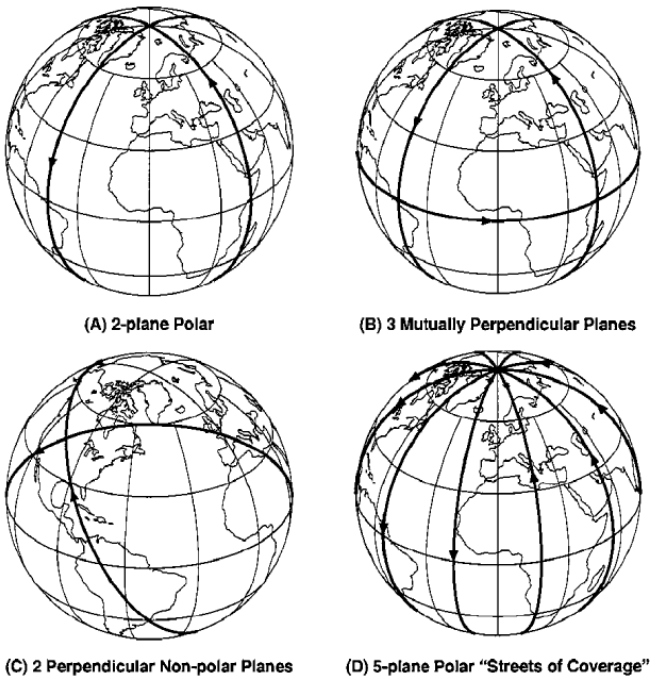


Figure 1.17: Examples of typical "Non-Walker" Constellations[47].

As already mentioned at the beginning of the chapter, any set of satellites acting simultaneously to achieve a common goal is considered a constellation. Following this philosophy, mission designers can tailor a specific set of orbits to optimize performance, reduce mission costs, or both. Those types of constellations are typically referred as "Non-Walker Constellations", because their typical characteristics are to break specific symmetries until the creation of constellations made of randomly placed orbits.

1.2.3 Selection of Constellation Parameters

The selection of the Constellation parameters allows us to define the best satellites pattern in space as a result of a cost vs. performance trade-off. The orbital elements $(a, e, i, \omega, \Omega, \nu)$[57] of the satellites are most frequently thought as parameters. In this section other key parameters are discussed, defining how much they affect the overall performance of the system in terms of coverage.

1. **Swath Width (Maximum Earth Central Angle)**
   The "Maximum Earth central angle" (MECA) in the context of coverage swath (for satellites, sensors, or remote-sensing instruments) is a geometric parameter that describes how far from the subsatellite point the sensor can still "see" the Earth's surface, measured as the angle at Earth's center between the subsatellite point and the edge of the sensor's coverage. It's a key parameter in satellites constellation because it determines directly the area that can be covered by each spacecraft. It is strictly dependent on payload's *Field Of View (FOV)*[55], a property of an optic instrument needed to scan the Earth surface. In a constellation that requires continuous coverage, the maximum Earth central angle represents the circle of coverage that can be seen by the satellite and the minimum swath width or width of the SoC represents the required spacing between orbital planes.

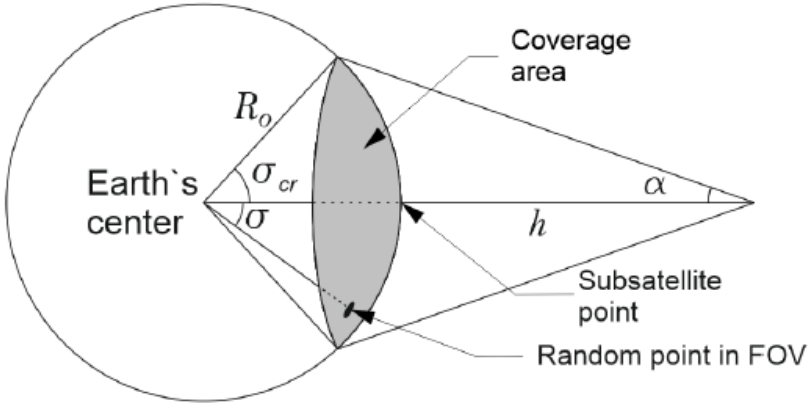


Figure 1.18: Relationship between FOV and Earth Central Angle.

The Maximum Earth Central Angle (σ_{cr} in the Fig. 1.18) is a function of both the altitude and the FOV of the satellites. The MECA is limited by the *minimum elevation angle* ε_{min}, defined as the angle above the local horizontal plane (tangent to Earth's surface at the ground station or target point) between the line of sight to the satellite and the local horizon. Geometric relationships yield:

$$\sigma_{cr} = \arccos\left(\frac{R_E}{R_E + h}\cos\varepsilon_{min}\right) - \varepsilon_{min} \tag{1.37}$$

$$\alpha = \frac{FOV}{2} = \arcsin\left(\frac{R_E}{R_E + h}\cos\varepsilon_{min}\right) \tag{1.38}$$

$$L_{max} = 2\,\sigma_{cr} \quad \text{or} \quad L_{max} = 2R_E\,\sigma_{cr} \tag{1.39}$$

where R_E is the Earth radius, h is the altitude and α is half the FOV of the satellite. If the minimum elevation angle contraint is considered, the MECA and the swath width are drastically reduced, therefore it is important to include this contraint, related to ground visibility properties, in the coverage analysis.
At last, we define the *maximum swath width* as twice the MECA, the maximum area that can be covered by the payload, and the *minimum swath width* is the swath width where the coverage is continuous thanks to overlapping coverage of adjacent satellites, therefore it is the L_{street} of the SoC.

2. **Altitude**
   The altitude is a key performance parameter because it defines the MECA and consequently the maximum swath width. Generally, it is recommended to place all the satellites of the constellation at the same altitude in order to have the same orbital period. This feature provides a pattern that repeats at each orbit, allowing for repeating observations. Otherwise, at each orbit the constellation will be in a different configuration, increasing the probability of collision and making more difficult for engineers to plan future operations. Another reason why the satellites should be placed at the same altitude is that the rotation rate of the nodes is coordinated, reducing the risk that different orbital planes collide.
   Given a fixed minimum elevation angle of the payload, then the altitude the key driver for constellation design. Specifically, higher altitudes will mean a smaller number of satellites and a smaller number of orbital planes. However, the number of satellites and planes is not a continuous function of the altitude, therefore we can identify some *altitude plateaus* below which an additional plane needs to be added. Altitude plateaus will be a function of the minimum elevation angle and the inclination of the orbit, but other limitations related to the spacecraft's systems can modify the results (for example launch costs, stationkeeping boxes or environment).

3. **Inclination**
   The inclination has a strong impact on both how coverage patterns are formed

and on coverage as a function of latitude. Different types of orbits determine various latitude-coverage functions. For example, an equatorial orbit has a constant latitude and therefore the coverage is maximum in the SoC and zero outside of the bounds of the SoC. For a polar orbit, the coverage increases with latitude and it is maximum at the poles. For a mid inclination orbit, the coverage is asymmetric with a peak at $Lat = i - L_{max}$ and it is nullified at $Lat = i + L_{max}$.
Another reason why inclination represents a key design aspect is the compensation of orbital perturbations on Earth. As described in [57], the oblateness of the Earth causes the node and the argument of perigee rotation. This rotation rate is function of the altitude, the inclination and the eccentricity. However, the rotation is not a problem as long as every satellite of the constellation undergoes the same rate. Thus, it is recommended to place all the satellites of the constellation at the same altitude, inclination and preferably the same eccentricity. For constellations, the orbits will have the critical inclination of 63.4 deg, where the rotation of the argument of perigee is balanced.

4. **Node Spacing**
   The node is defined as the point in the orbital plane where the satellite crosses the emisphere of the Earth from south to north (ascending) or from north to south (descending). Typically, it is not important to determine the nodes location of the planes, since they will rotate due to J2 effect[57], but the distribution of the nodes along the equator is a key design aspect.
   Four types of nodes spacing are commonly used:ù

   - Equal node spacing over the complete equator ($\Delta N = (360\,\text{deg})/m$), typical for Walker Constellations;
   - Equal node spacing over half the equator ($\Delta N = (180\,\text{deg})/m$), typical for Elliptical Constellations to avoid coverage gaps between orbits;
   - Equal node spacing except for a seam between satellites going up and coming down, like in Streets of Coverage polar Constellations;
   - Node spacing adjusted in pairs or triplets to provide "fill-in" coverage for successive satellites.

1.2.4 Constellation Design Process

The key requirement in the process of constellation design is to understand the mission objectives and what is needed to fullfil the mission, particularly in terms of coverage. It means to understand the coverage needs for the mission and the spacecraft needs to provide that coverage, for example subsystems design requirements as a consequence of coverage requirements. The constellation design can be

described by the following algorithm:

Algorithm 3 The Constellation Design process.

1: Establish constellation-related mission requirements, particularly:
   - Latitude-dependent coverage
   - Goals for growth and degradation plateaus
   - Requirements for different modes or sensors
   - Limits on system cost or number of satellites
2: Do all single satellite orbit trades except coverage.
3: Do trades between swath width (or MECA), coverage, and number of satellites. Evaluate candidate constellations for:
   - Coverage Figures of Merit vs. Latitude and mission mode
   - Coverage excess
   - Growth and degradation
   - Altitude plateaus
   - End-of-Life options

   Consider the constellation patterns at Sec. 1.2.2.
4: Evaluate ground track plots for potential coverage holes or methods to reduce the number of satellites.
5: Adjust inclination and in-plane phasing to maximize the intersatellite distances at plane crossings for collision avoidance.
6: Review the rules of constellation design.
7: Document reasons for choices and iterate.

The principal factors to be defined during the constellation design are listed in Table 1.6, along with the major selection criteria. A key point to note is that constellation design consists of more than just orbit elements. The minimum working elevation angle is perhaps the most critical parameter in defining constellation coverage. Collision avoidance parameters, including the station-keeping method and the size of the station-keeping box are key to ensuring the integrity of the constellation over its lifetime. Sometimes, even a combination of multiple constellation patterns can be the best solution to satisfy the mission objectives at lower cost and risk. An example of the previous statement is the BeiDou Navigation System constellation, which is composed by a combination of 3 patterns coordinated at different altitude and inclination (Table 1.4) or the Starlink constellation, with multiple shells of Walker patterns (Table 1.4).

Typically the purpose of creating a constellation is to provide Earth coverage, with the drawback of requiring more than one satellite, increasing the number of systems to be manifactured and assembled, leading to high overall costs. We

Factor	Effect	Selection Criteria
Principal Design Variables:		
Number of Satellites	Principal determinant of cost and coverage	Minimize number consistent with meeting other criteria
Constellation pattern	Determines coverage vs. latitude, plateaus	Select for best coverage
Minimum Elevation Angle	Principal determinant of single satellite coverage	Minimum value consistent with payload performance and constellation pattern
Altitude	Coverage, environment, launch and transfer cost	System level trade of cost vs. performance
Number of Orbit Planes	Determines coverage plateaus, growth and degradation	Minimize consistent with coverage needs
Collision Avoidance Parameters	Key to prevent constellation destruction	Maximize the intersatellites distance at plane crossings
Secondary Design Variables:		
Inclination	Determines latitude distribution of coverage	Compare latitude coverage vs. launch costs
Between Plane Phasing	Determines coverage uniformity	Select best coverage among discrete phasing options
Eccentricity	Mission complexity and coverage vs. cost	Normally zero; non-zero may reduce number of satellites needed
Size of Stationkeeping Box	Coverage overlap needed; cross-track pointing	Minimize consistent with low cost maintenance approach
End-of-Life Strategies	Elimination of orbital debris	Any mechanism the elimination of debris

Table 1.6: Principal Factors to be defined during Constellation Design.

can state the main goal of a constellation is to provide the needed coverage while minimizing the number of satellites involved. Therefore, the principal system

trade-off is a measure of coverage (performance) vs. number of satellites (cost).

It is possible to classify satellite constellations in those that require global coverage and those that do not. The first type is the most straightforward in mission design and the most common in space. We can define an interesting figure of merit for continuous coverage constellations, called *excess coverage*. It is defined as the total instantaneous coverage available as a percentage of the total required, meaning that we want it to be 1. For N satellites in circular orbits at the same altitude with coverage defined as the area included in the circle with radius of L_{max} centered at the subsatellite point, the total instantaneous coverage (C_{tot}) is given by:

$$C_{tot} = N \frac{(1 - \cos(L_{max}))}{2K} \tag{1.40}$$

where K is the multiplicity of coverage needed, defined as the number of satellites within the constellation that can simultaneously access, or mantain a line-of-sight, with a specific region on the planet's surface[58].

Finally, it is important to determine a cause-effect graph showing the direct relationship between constellations parameters and factors of the performance vs. cost analysis. The parameters have been described in previous subsections and can be summarized as: altitude h, inclination i, the node spacing between different orbital planes ΔN, the phase difference between two satellites in the same orbital plane ΔS, the maximum swath width L_{max} and the eccentricity e, where a combination of these parameters is required to generate a constellation geometric pattern. Other parameters are not included because they are secondary parameters derived by the latter, for example the relative inclination i_R and the phase offset $\Delta\phi$ are function of ΔN and i (Eq.(1.31) and (1.32)), the FOV and the MECA are function of L_{max} (Eq. (1.37) and (1.39)). The design factors determined by the parameters are the following: the number of orbital planes m, the total number of satellites T, the orbital perturbations, the environment, the launch options, the collision avoidance parameters and the constellation deployment, replenishment and end-of-life options. To conclude, the design factors are the Figures of Merit (FoM) that determine the results of the Performance vs. Cost trade-off, where the performance is identified by the coverage. In the Diagram, the blue blocks represent constellation parameters, identified by the orbital parameters of the satellites and their geometric pattern in orbit, the green blocks represent the constellation factors or issues that are of the main interest in the trade-off analysis, and finally the red blocks are the main FoM of the design process, the coverage and the mission cost.

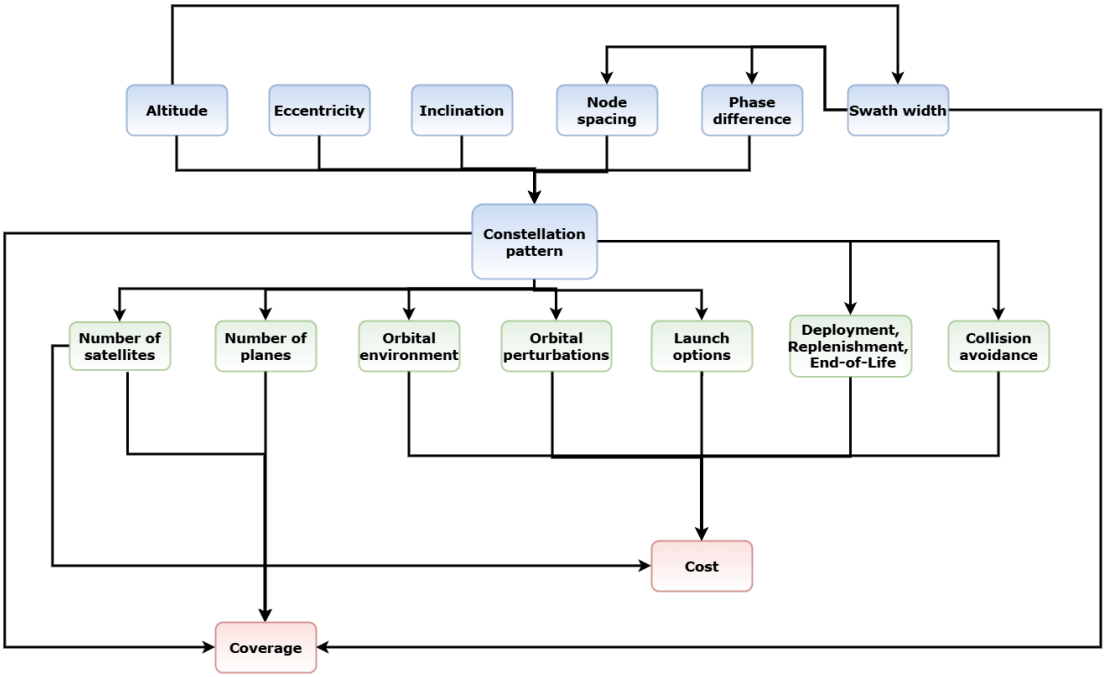


Figure 1.19: Cause-effect diagram of the Constellation Design Process.

Chapter 2

Methods

This chapter is devoted to the methodology we apply to achieve the results that this thesis aims to obtain. In particular, I do not aim to create a trade-off analysis based on a Performance VS Cost criteria, but to study the propagation of the orbital motion for lunar satellites under the effect of the main perturbations experienced near the Moon. In particular, we aim at analyzing if a constellation of satellites, deployed in an "Earth-like" configuration, survives after a period of time reasonable for typical operational services, like observation or navigation.

To obtain the satellites' initial configurations we use the state-of-the-art of Earth Satellite Constellations, as thoroughly described in Sec. 1.2, to describe feasible constellations' patterns that have been already successful on Earth's orbital environment. Later, it was important to decide the propagation method, which involved the study of the equations of motion and the orbital environment which defined the relevant perturbations to include in the analyses. Specifically, numerical integration is fundamental to achieve precise orbit propagation under perturbations like the Lunar Perturbations described in Sec. 1.1.2. In this chapter we describe and provide the algorithms adopted, and Python was chosen as the programming language to implement into practice the theory discussed in the previous chapter. Another crucial part of the work is to decide which factors are important to visualize and interpretate, in order to comment the result of the numerical propagation. For this reason, another section of this chapter describes the constellations' performance and stability metrics that have been fathomed to discuss the results and reach the conclusions.

This method made it possible to draft a simulation plan, because each time the main code was ran, different initial conditions were chosen. The initial conditions to differ each time were the constellation pattern, the initial altitude, the initial inclination, the number of satellites, the number of planes and the phasing factor,

which gave a global understanding of the behaviour of Lunar Satellite Constellations.

2.1 Python Code Organization

Python was chosen for the implementation of all the algorithms because of the several advantages that it provides with respect to other languages popular in Aerospace Engineering applications. First, the main advantage is to be an open-source language, free and with English-like syntax, while mantaing a relatively high computational speed. Python overcomes the problem of using multiple languages for computations, data analysis and plotting, by integrating in one single software the possibility to wrap the lines of code into specific packages, where each package can wrap "pre-compiled" algorithms interpreted in Fortran/C++ or MatLab languages[59].

The Python packages used in this thesis are the following: **`math`**, a Python-embedded package used to perform basic mathematical operations; **`numpy`**, needed to deal with N-dimensional arrays, as well as vectors and matrix operations[60]; **`scipy`**, needed for mathematical calculus and numerical integration[61]; **`matplotlib`** and **`mpl_toolkits`**, used for the best 2D and 3D graphic representation of data[62]; **`pandas`**, to read and load `.csv` and `.txt` files[63]; **`spiceypy`**, the Python wrapper of the NASA SPICE toolkit which includes all the planetary constants and ephemeris of the celestial bodies[64][65][66]; **`pyshtools`**, needed to compute the series expansion of the gravitational spherical harmonics[67]; **`os`**, **`functools`** and **`time`**, which are Python-embedded packages helpful to measure the computational speed, deal with filenames and paths, handling the cache and RAM during a process.

All the Python files are stored in a folder called "Functions", which contains also subfolders to store the images of the results, subroutines or for example the NASA SPICE Toolkit files. The main code is called `Simulations.py`, where all the other functions are imported and called to start the simulation with user input parameters. The numerical integrator function is located in the file `Perturbed_KR2BP.py`, whereas the computation of the perturbing acceleration in the Moon's orbital environment is found in the file `Lunar_Perturbations.py`. Other functions located in the folder are: a series of function which initialise the orbital elements of the satellites of a constellation given the needed inputs, called `Lunar_Constellations.py`, and a code which stores the inclination-eccentricity diagrams of the frozen orbits theory, called `Lunar_Frozen_Orbits.py`. Another important Python file is `Lunar_RF_Transformations.py`, which is recalled in all of the previous codes whenever it is necessary to convert the state vector from one reference frame to another. Next subsections will give more detailed information about each of the

functions and the algorithms I wrote for this thesis.

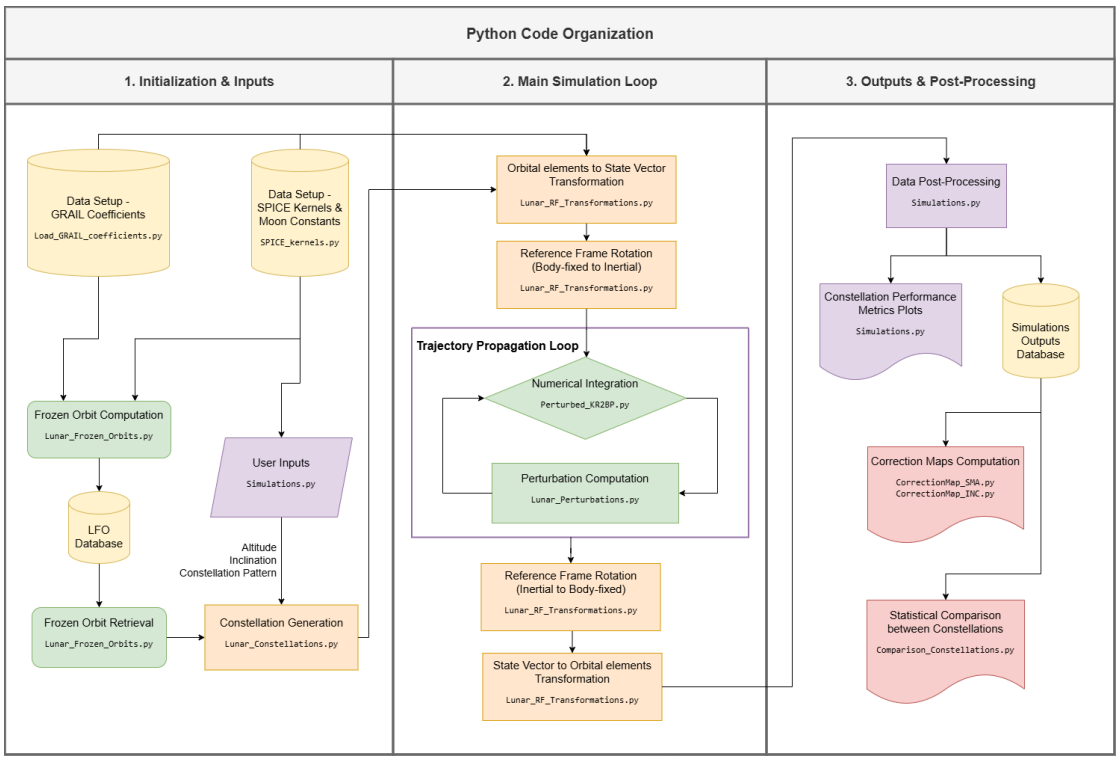


Figure 2.1: Python code organization represented with a system architecture flowchart.

2.1.1 `Perturbed_KR2BP.py`

The first step is to create a numerical integrator for the equations of motion of an artificial satellite in orbit about the Moon. For the derivation of the equations of motion, different formulations can be adopted, such as the Hamiltonian Mechanics or the Circular Restricted 3-Body Problem. We decide to adopt the hypothesis of the Cowell's Method, thoroughly described in Sec. 1.1.1, where Eq. (1.14) are numerically integrated in the 6 degrees of freedom that belong to any 3-dimensional trajectory. The equations are written in Cartesian coordinates for a Moon-Centered Inertial reference frame, which was chosen at J2000. In this way, it is easier to proceed with the integration because the axes are fixed in space and time as defined by IAU[21] and it is not necessary to compute the centrifugal and Coriolis contribution.

As showed by the algorithmic representation of the lines of code in Alg. 4 and 5, the numerical integration of the equations of motion with Cowell's method is performed by a function that takes as input the initial state vector y_0 and the

Algorithm 4 Equations of Motion for Perturbed Two-Body Problem

procedure PERT_KR2BP($t, \mathbf{y}, \mu, f_{pert}$)
  Input: Time t, State vector $\mathbf{y}$, Gravitational parameter μ, Func f_{pert}
  Output: State derivative $\dot{\mathbf{y}}$
  $\mathbf{r} \leftarrow \mathbf{y}[0:3]$ ▷ Extract position
  $\mathbf{v} \leftarrow \mathbf{y}[3:6]$ ▷ Extract velocity
  $r \leftarrow \|\mathbf{r}\|$
  $\mathbf{a}_{grav} \leftarrow -\frac{\mu}{r^3}\mathbf{r}$ ▷ Compute Keplerian acceleration
  $\mathbf{a}_{pert} \leftarrow f_{pert}(t, \mathbf{y})$ ▷ Call perturbation model
  $\mathbf{a}_{total} \leftarrow \mathbf{a}_{grav} + \mathbf{a}_{pert}$
  $\dot{\mathbf{y}} \leftarrow [\mathbf{v}, \mathbf{a}_{total}]$ ▷ Concatenate derivative vectors
  return $\dot{\mathbf{y}}$
end procedure

Algorithm 5 Numerical Integration of the Perturbed KR2BP (Cowell's Method)

procedure INTEGRATE_PERT_KR2BP($\mathbf{y}_0, [t_0, t_f], \mu, f_{pert}$)
  Input: Initial state $\mathbf{y}_0$, Timespan $[t_0, t_f]$, Grav. parameter μ, Func f_{pert}
  Output: Solution structure $\mathcal{S}$ ▷ *Bunch* object with dictionary-like attributes
  ▷ We select the integration method and the tolerances (absolute and relative)
  $Method \leftarrow$ DOP853
  $Tols \leftarrow \{\text{rtol} = 10^{-12}, \text{atol} = 10^{-12}\}$
  ▷ Pass parameters to the ODE solver
  $Args \leftarrow (\mu, f_{pert})$
  ▷ Solve using the derivative model from Alg. 4
  $\mathcal{S} \leftarrow$ SolveIVP(Pert_KR2BP, $[t_0, t_f], \mathbf{y}_0, Args, Tols$)
  return $\mathcal{S}$ ▷ We can extract time-series with $\mathcal{S}.t$ and $\mathcal{S}.y$
end procedure

time span, and takes as arguments the gravitational parameter μ and the callable perturbation function. The integration is done with the function `solve_ivp` from the `scipy.integrate` module, using as default relative and absolute tolerance 10^{-12}. The callable perturbation function f_{pert} takes as an input the time t and the instantaneous state vector y, in the same way as the ODEs are integrated, as defined by Alg. 4. The output of the function is a `scipy.integrate.OdeResult` object, where the time vector and the solution vector have to be extracted in the post-processing.

Algorithm 6 Equations of Motion for Unperturbed KR2BP

procedure KR2BP($t, \mathbf{y}, \mu$)
  Input: Time t, State vector $\mathbf{y}$, Gravitational parameter μ
  Output: State derivative $\dot{\mathbf{y}}$
  $\mathbf{r} \leftarrow \mathbf{y}[0:3]$ ▷ Extract position
  $\mathbf{v} \leftarrow \mathbf{y}[3:6]$ ▷ Extract velocity
  $r \leftarrow \|\mathbf{r}\|$
  $\mathbf{a} \leftarrow -\frac{\mu}{r^3}\mathbf{r}$ ▷ Compute Keplerian acceleration
  $\dot{\mathbf{y}} \leftarrow \text{Hstack}(\mathbf{v}, \mathbf{a})$ ▷ Concatenate derivative vectors
  return $\dot{\mathbf{y}}$
end procedure

Algorithm 7 Numerical Integration of KR2BP

procedure INTEGRATE_KR2BP($\mathbf{y}_0, [t_0, t_f], \mu$)
  Input: Initial state $\mathbf{y}_0$, Timespan $[t_0, t_f]$, Grav. parameter μ
  Output: Solution structure $\mathcal{S}$ ▷ *Bunch* object with dictionary-like attributes
  ▷ We select the integration method and the tolerances (absolute and relative)
  $Method \leftarrow$ RK45
  $Tols \leftarrow \{\text{rtol} = 10^{-12}, \text{atol} = 10^{-12}\}$
  $Args \leftarrow (\mu)$
  ▷ Solve using the derivative model from Alg. 6
  $\mathcal{S} \leftarrow \text{SolveIVP}(\text{KR2BP}, [t_0, t_f], \mathbf{y}_0, Args, Tols)$
  return $\mathcal{S}$ ▷ We can extract time-series with $\mathcal{S}.t$ and $\mathcal{S}.y$
end procedure

In order to prove the validity of the algorithms the functions have been tested by passing as a perturbing acceleration $f_{pert} = 0$ and the result compared with the output of the numerical integration of the unperturbed KR2BP, which was implemented in Alg. 6 and 7. The main difference between the two numerical integrators is that in the unperturbed functions the state vector is already unstacked in the position and velocity components, while the perturbed propagator code is more honed and refined for easier implementation. Another difference is the integration method, set to the standard Runge-Kutta 45 ('RK45') for the unperturbed case and to the high precision Dormand-Prince 8-53 ('DOP853') for the perturbed case, because the perturbation functions are non-linear and the precision of the integration needs to be increased. The comparison test was successful, therefore I proceeded with the creation of the perturbation functions

that could compute the orbital perturbations relative to the Lunar gravitational environment.

2.1.2 `Lunar_Perturbations.py`

As mentioned in previous chapters, in order to represent the Lunar orbital environment accurately, it is necessary to approximate with a mathematical function the perturbing acceleration that act on a spacecraft in LLOs, MLOs and HLOs. Since the purpose of the thesis is to analyse the dynamics of constellations up to 5000 km of altitude, the Solar third-body effect and the SRP can be neglected to keep a high level the accuracy of the propagator.

In order to create the f_{pert} for the Lunar Gravity Field and Earth's Tidal Acceleration, it was first necessary to load the spherical harmonic coefficients and secondly retrieve the high-precision ephemerides of the Moon and the Earth. The GRAIL Spherical Harmonic Coefficients are open-source and located in the website[1] of the NASA Planetary Data System (PDS) Geosciences Node[68], up to 1200 degree. The following algorithm shows how the `.csv` file is loaded, the coefficients are extracted up to the maximum degree 50 and stored in `.npy` matrices called C_{nm} and S_{nm}. It is worth mentioning that the coefficients are 4pi-geodesy normalized, therefore they are ready to be used in the Eq.(1.18), because the Legendre polynomials, present in the series expansion and computed by the function `pysh.legendre.PlmBar_d1`, accept only this type of normalization.

Before introducing the perturbing functions, it is necessary to explain how the most updated Moon and Earth ephemerides (DE440 and DE441[69]) are used in the code. At the incipit of each code is necessary to load some files provided by the NASA SPICE Toolkit[23] called "kernels". The kernels are files containing information about the geometry, timing, rotation matrices and physical properties of the most important space missions and Solar System celestial bodies. As described by Alg. 9, it is necessary to pass a list of kernel files as well as the directory where those files are stored, in order to load them and keep them in memory ready to be called with the Python functions of the `spiceypy` package. The kernels loaded to accomplish the purpose of this thesis are the following:

- '`naif0012.tls`', a Leapseconds kernel (LSK) that is needed to convert the time from Universal Coordinated Time (UTC) to Ephemeris Time (ET);
- '`pck00011.tpc`', a Text Planetary Constants kernel (PCK) which contains the standard physical constants of the planets, such as the radii and the prime meridian orientation;

[1] https://pds-geosciences.wustl.edu/

Algorithm 8 Processing and Extraction of GRAIL Spherical Harmonic Coefficients

Require: Source data file $\mathcal{F}$ (containing columns n, m, C, S), Maximum degree N_{max}
Ensure: Coefficient matrices $\mathbf{C}_{nm}$ and $\mathbf{S}_{nm}$

Initialization:
Define matrix size $K \leftarrow N_{max} + 1$
Initialize $\mathbf{C} \leftarrow \mathbf{0}_{K \times K}$ ▷ Matrix of zeros
Initialize $\mathbf{S} \leftarrow \mathbf{0}_{K \times K}$ ▷ Matrix of zeros
$\mathbf{C}[0, 0] \leftarrow 1.0$ ▷ Set degree 0 term by convention
Data Loading:
$D \leftarrow \text{ReadCSV}(\mathcal{F})$ ▷ Skip header row
Population:
for each row r in D **do**
    $n \leftarrow r_n$
    $m \leftarrow r_m$
    if $n \leq N_{max}$ **then**
        $\mathbf{C}[n, m] \leftarrow r_C$
        $\mathbf{S}[n, m] \leftarrow r_S$
    end if
end for
Output:
Save $\mathbf{C}, \mathbf{S}$ to binary files (.npy)

- `'gm_de440.tpc'`, a Text Planetary Constants kernel (PCK) which contains the standard gravitational parameters of the planets;
- `'de440.bsp'`, a Spacecraft & Planets kernel (SPK) that contains all the data about the positions (trajectories) of the Sun, Earth and Moon;
- `'moon_pa_de440_200625.bpc'`, a Binary PCK that contains the high-precision data for the orientation (Euler Angles) of the Moon's Principal Axes (PALRF), including the librations;
- `'moon_de440_250416.tf'`, a Frame kernel (FK) where the reference frames ME and PALRF ('MOON_ME' and 'MOON_PA' in the SPICE notation) are defined and how they mathematically relate to the inertial J2000 frame;
- `'moon_assoc_me.tf'` and `'moon_assoc_pa.tf'` are FK that set the default reference frame for the Moon, choosing between ME and PALRF.

After the SPICE kernels are loaded, it is possible to use the following callable function that calculates the perturbing acceleration at each instant of the integration,

Algorithm 9 Loading SPICE Kernels

Require: List of kernel filenames $\mathcal{L}$, Directory path $\mathcal{D}$
Ensure: Boolean status indicating success or failure
Initialization:
$N_{loaded} \leftarrow 0$
Processing:
for each kernel k in $\mathcal{L}$ **do**
    $P \leftarrow \text{JoinPath}(\mathcal{D}, k)$ ▷ Construct full file path
    if File P does not exist **then**
        Error: "Cannot find kernel file"
        return False
    end if
    try:
    FURNSH(P) ▷ Load kernel using SPICE toolkit
    $N_{loaded} \leftarrow N_{loaded} + 1$
    Log: "Successfully loaded P"
    Catch: SPICE Error or Exception
    Error: Log specific exception details
    return False
    end try
end for
Success:
Log: "All N_{loaded} kernels loaded successfully"
return True

described by Alg.10.

First, the Moon constants are initialized using `spiceypy.bodvrd`; then, the position vector at time t is rotated from the inertial J2000 reference frame to the body-fixed MOON_PA frame, thanks to the instantaneous rotation matrix retrieved with `spiceypy.pxform` function. The body-fixed coordinates are converted to spherical (radial, latitude, longitude), and passed to the function `pysh.gravmag.MakeGravGridPoint`, which computes the acceleration in spherical coordinates using Eq.(1.18). Lastly, the acceleration is converted back to cartesian coordinates and then rotated using the inverse rotation matrix.

The Earth's Tidal Acceleration is computed using the same logic: the position vector is extracted and rotated to the 'MOON_PA' frame, the gravitational constant of the Earth is retrieved with `spiceypy.bodvrd` and the ephemeris of the Earth relative to the Moon's origin is retrieved using `spiceypy.spkpos`. Before applying Eq.(1.21), it is necessary to compute the position of the spacecraft with

Algorithm 10 Lunar Gravity Perturbation Calculation

Require: t: Current simulation time
Require: $\mathbf{x}_{MCI}$: State vector in Moon Centered Inertial frame $[x, y, z, v_x, v_y, v_z]^T$
Require: C_{nm}, S_{nm}: Normalized spherical harmonic coefficients
Require: N_{max}: Maximum degree of harmonics
Ensure: $\mathbf{a}_{MCI}$: Perturbing acceleration in MCI frame
Constants Retrieval: ▷ From SPICE
$\mu_{moon} \leftarrow$ GetGravitationalParameter('MOON')
$R_{ref} \leftarrow$ GetEquatorialRadius('MOON')
Frame Transformation (Inertial to Body-Fixed):
$\mathbf{r}_{MCI} \leftarrow \mathbf{x}_{MCI}[1:3]$ ▷ Extract position vector
$R_{J2k \to PA} \leftarrow$ RotationMatrix$(t$, 'J2000', 'MOON_PA') ▷ From SPICE
$\mathbf{r}_{PA} \leftarrow R_{J2k \to PA} \cdot \mathbf{r}_{MCI}$ ▷ Rotate position to Principal Axes
Cartesian to Spherical Conversion:
$x, y, z \leftarrow \mathbf{r}_{PA}$
$r \leftarrow \sqrt{x^2 + y^2 + z^2}$
$\phi \leftarrow \arcsin(z/r)$ ▷ Latitude
$\lambda \leftarrow \arctan 2(y, x)$ ▷ Longitude
Spherical Harmonics Gradient: ▷ From pyshtools
▷ Compute acceleration components in spherical basis $(\hat{e}_r, \hat{e}_\phi, \hat{e}_\lambda)$
$(a_r, a_\phi, a_\lambda) \leftarrow$ SphericalHarmonicsGravity$(r, \phi, \lambda, \mu_{moon}, R_{ref}, C_{nm}, S_{nm}, N_{max})$
Spherical Basis to Cartesian PA Conversion:
$a_{x,PA} \leftarrow a_r \cos\phi \cos\lambda - a_\phi \sin\phi \cos\lambda - a_\lambda \sin\lambda$
$a_{y,PA} \leftarrow a_r \cos\phi \sin\lambda - a_\phi \sin\phi \sin\lambda + a_\lambda \cos\lambda$
$a_{z,PA} \leftarrow a_r \sin\phi + a_\phi \cos\phi$
$\mathbf{a}_{PA} \leftarrow [a_{x,PA}, a_{y,PA}, a_{z,PA}]^T$
Frame Transformation (Body-Fixed to Inertial):
$R_{PA \to J2k} \leftarrow (R_{J2k \to PA})^T$ ▷ Inverse rotation
$\mathbf{a}_{MCI} \leftarrow R_{PA \to J2k} \cdot \mathbf{a}_{PA}$
return $\mathbf{a}_{MCI}$

respect to the Earth. Finally, the resulting acceleration is converted back to the inertial J2000 coordinates to be used in Alg.4.

The functions were also tested to verify the correct logic of the code, and in fact several modifications were made before reaching the final version of the algorithms presented. The most relevant change is the introduction of the `pyshtools` package, which sped up the lunar gravity computation by 2 orders of magnitude with respect to the manual summation. The total perturbing acceleration is computed by simply defining a final function "total_moon_perturbation" that calls both and sum them,

Algorithm 11 Earth Third-Body Perturbation Calculation

Require: t: Current simulation time
Require: $\mathbf{x}_{MCI}$: Satellite state vector in Moon Centered Inertial frame
Ensure: $\mathbf{a}_{MCI}$: Perturbing acceleration in MCI frame

Initialization and Constants: ▷ From SPICE
$\mu_{earth} \leftarrow$ GetGravitationalParameter('EARTH')
Frame Transformation (Inertial to Body-Fixed):
$\mathbf{r}_{sat,MCI} \leftarrow \mathbf{x}_{MCI}[1:3]$ ▷ Extract satellite position
$R_{J2k \to PA} \leftarrow$ RotationMatrix(t, 'J2000', 'MOON_PA') ▷ From SPICE
$\mathbf{r}_{sat,PA} \leftarrow R_{J2k \to PA} \cdot \mathbf{r}_{sat,MCI}$ ▷ Rotate position to Principal Axes
Retrieve Third-Body Ephemeris: ▷ From SPICE
▷ Get Earth position relative to Moon
$\mathbf{r}_{earth,PA} \leftarrow$ GetEphemeris(t, Target='EARTH', Obs='MOON', 'MOON_PA')
Compute Acceleration (in PA frame):
$\mathbf{d} \leftarrow \mathbf{r}_{sat,PA} - \mathbf{r}_{earth,PA}$ ▷ Calculate distance vector from Earth to Satellite
$d \leftarrow \|\mathbf{d}\|$
$r_{earth} \leftarrow \|\mathbf{r}_{earth,PA}\|$
▷ Third-body perturbation formula: Eq.(1.20)
$\mathbf{a}_{PA} \leftarrow -\mu_{earth}\left(\frac{\mathbf{d}}{d^3} + \frac{\mathbf{r}_{earth,PA}}{r_{earth}^3}\right)$
Frame Transformation (Body-Fixed to Inertial):
$R_{PA \to J2k} \leftarrow (R_{J2k \to PA})^T$ ▷ Inverse rotation
$\mathbf{a}_{MCI} \leftarrow R_{PA \to J2k} \cdot \mathbf{a}_{PA}$
return $\mathbf{a}_{MCI}$

and then in the main code it is given to the numerical integrator.

2.1.3 `Lunar_Frozen_Orbits.py`

It is necessary to develop an algorithm that can find the orbital elements valid for stable orbits under the lunar perturbations aforementioned. The following algorithms, written in Python, allow to search for LFOs with the method of M.Lara[43], therefore it is of uttermost importance to understand the differences between the perturbation model used in this thesis and the preliminary design for the search of LFOs developed by Lara. In fact, the LFOs are found by searching the roots of Eq.(1.26) which is an equation derived analytically by double-averaging the Hamiltonian equations of motion. To apply the averaging and simplifying the expressions, further hypothesis have been made to derive the final form of the equation, therefore the physical domain where these results are valid is more

approximated than the domain where the equations of motion of the orbital propagator are integrated. The main difference lies on the reference frames in which the equations are solved: while I write the equations of motion in the J2000 reference frame, with the perturbations that are computed after rotating the position vector using the most accurate DE440 and DE441 ephemeris of the Moon, the equations that are described in Sec.1.1.2 assume a much simpler reference frame that neglects the perturbations in the Earth-Moon semi-major axis, the mean motion, the inclination with respect to the ecliptic and also the rotation axis librations.

The purpose of this code is to assign, given the altitude and the inclination of the orbit, the corresponding eccentricity and the argument of periapsis that make that orbit frozen and stable for a long period of time. In this analysis it has been neglected the influence of the RAAN on the stability of the frozen condition, assuming that for constellations the orbital planes are evenly distributed and RAAN is forced to assume all the values from 0 deg to 360 deg. Unfortunately, given the great differences about the hypothesis, it is almost impossible to find a LFO analytically that remains stable after the orbit is propagated numerically. Still the following algorithms describe how to take an initial guess on the starting orbital elements before the frozen stability is analyzed.

The Alg.14 describes how the double-averaging theory, described in Sec.1.1.2, is applied to find initial orbital elements for a preliminary frozen orbit. To do so, it is necessary to find the root for the Eq.(1.26) that makes $\dot{g}(e) = 0$, while the time derivative of the eccentricity is already solved because $\dot{G} = 0$ when the argument of periapsis $g = \pm\frac{\pi}{2}$. Before solving the equation, the functions are defined outside of the main function, as it is described by Alg.12 and Alg.13 (the definition of the helper math functions is obvious and therefore neglected). After the equation to solve has been defined, the reference argument of periapsis is initialized to 90 deg, while the code is adapted to allow for negative eccentricity solution. Then, the search bounds are defined as the impact eccentricity[2] at the given altitude ($e_{max} = 1 - \frac{R_{\leftmoon}}{a}$) and a tolerance near zero to avoid singularities caused by the presence of e in the denominator of a fraction (ϵ). Using the Brent's Method[70] to solve the equation, the root is then searched first in the positive interval $[\epsilon, e_{max}]$, defined as the interval which corresponds to $\omega = 90$ deg. If the solution is found, the eccentricity and $\omega = 90$ deg are returned as the output, otherwise the search in the negative interval $[-e_{max}, -\epsilon]$ starts, defined as the interval which corresponds to $\omega = 270$ deg. In this case the outputs are the absolute value of the eccentricity,

[2]The eccentricity at which the radius of periapsis is lower than the surface radius of the Moon for a given semi-major axis.

Algorithm 12 Computation of the summation term $S_n^\star$

Require: Spherical Harmonic degree n, Eccentricity e
Ensure: $S_n^\star$
$S_{total} \leftarrow 0$
$n_2 \leftarrow n \pmod 2$
for $j \leftarrow n_2$ **to** $n-2$ **step** 2 **do**
    Compute coefficient $\tilde{\alpha}_{j,n}$
    $Sum_i \leftarrow 0$
    for $idx \leftarrow n_2$ **to** n **step** 2 **do**
        Compute $\psi(idx, j, n, e)$ using $\tilde{\beta}$ coefficients
        $Sum_k \leftarrow 0$
        for $k \leftarrow n_2$ **to** idx **step** 2 **do**
            Compute $\tilde{\gamma}_{idx,j,k}$ and trigonometric terms
            Update Sum_k
        end for
        Update Sum_i using ψ and Sum_k
    end for
    $S_{total} \leftarrow S_{total} + \tilde{\alpha}_{j,n} \cdot e^j \cdot Sum_i$
end for
return S_{total}

Algorithm 13 Differential equation $\dot{g}(e)$

Require: Eccentricity e
Ensure: $\dot{g}(e)$
$e \leftarrow \text{clip}(|e|, \epsilon, 1.0)$ ▷ Singularity protection
$\eta \leftarrow \sqrt{1-e^2}$
Compute Third Body Perturbation:
$\dot{g}_{hill} \leftarrow N \cdot \left(\frac{N_{moon}}{N}\right)^2 \cdot \frac{3}{8\eta} \cdot [4\eta^2 + 5(e^2 - \sin^2 i)(1 - \cos 2g)]$
Compute Zonal Harmonic Perturbation:
$\dot{g}_{zonal} \leftarrow 0$
for $n \leftarrow 2$ **to** n_{max} **do**
    $S_n^* \leftarrow$ CALCULATE_S_STAR(n, e)
    $term_n \leftarrow C_{n,0} \cdot (R_{moon}/a)^n \cdot \frac{S_n^*}{2^n \eta^{2n}}$
    $\dot{g}_{zonal} \leftarrow \dot{g}_{zonal} + term_n$
end for
return $\dot{g}_{hill} + (N \cdot \dot{g}_{zonal})$

and the argument of periapsis flipped to $\omega = 270$ deg.

Algorithm 14 Calculation of Frozen Orbit Eccentricity

Require: Semi-major axis a, Inclination i, Reference argument of periapsis ω_{ref}
Ensure: Eccentricity e, Argument of periapsis ω

$N \leftarrow \sqrt{\mu_{moon}/a^3}$
$g \leftarrow \omega$
function CALCULATE_S_STAR(n, e)
    Execute Alg.12
end function
function G_DOT(e) ▷ Differential equation dg/dt
    Execute Alg.13
end function
$e_{max} \leftarrow 1 - (R_{moon}/a)$ ▷ Impact eccentricity to bound the search
$\epsilon \leftarrow 10^{-9}$ ▷ Tolerance to avoid singularities
Attempt 1: Search in Positive Interval $[\epsilon, e_{max}]$
if $\dot{g}(\epsilon) \cdot \dot{g}(e_{max}) < 0$ **then** ▷ Check if root exists
    $e_{sol} \leftarrow \text{BrentQ}(\dot{g}, \epsilon, e_{max})$
    return $e_{sol}, 90$ deg
end if
Attempt 2: Search in Negative Interval $[-e_{max}, -\epsilon]$
if $\dot{g}(-e_{max}) \cdot \dot{g}(-\epsilon) < 0$ **then** ▷ Check if root is bracketed
    $e_{sol} \leftarrow \text{BrentQ}(\dot{g}, -e_{max}, -\epsilon)$
    return $|e_{sol}|, 270$ deg
end if
Failure: No root found in valid domain
return None, **None**

In order to have an easy data storage, for a given altitude the Brent's Method is applied in a `for` cycle for each inclination in the range of [0,90] deg with step of 0.1 deg, to search the eccentricity of the frozen orbit for all the possible inclinations at once and store the results for a later use. After initializing the Moon's constants using the SPICE kerneks, the GRAIL coefficients are un-normalized by a coefficient $\sqrt{2n+1}$, and then the user selects the desired altitude to start searching the frozen eccentricity.

The main feature about Alg.15 is that the zonal coefficients used to compute the perturbations are stopped up to degree 20, because the helper math functions which rely on factorials and double factorials would cause numerical instability for too high n, and also to speed up the calculations. Considering that the the gravity coefficients themselves have uncertainties and estimated errors, it is convenient

Algorithm 15 Computation of LFOs and Inclination-Eccentricity Diagram

Require: SPICE Kernels, Gravity Model Coefficients C_{nm}, User's input altitude h
Ensure: LFO Dataset (I, e, ω), Eccentricity-Inclination Diagram

Initialization:
Load SPICE kernels
Retrieve Moon constants: μ_{moon}, R_{moon}
Load and un-normalize gravity coefficients $C_{n,0}$ up to degree $n_{max} = 20$
Define Orbit Parameters:
$a \leftarrow R_{moon} + h$ ▷ Semi-major axis
$\omega_{ref} \leftarrow \pi/2$ ▷ Initial Argument of Periapsis
$i_{vec} \leftarrow [0, 0.1, \ldots, 90]$ ▷ Inclination vector in degrees
Initialize empty arrays e_{vec}, ω_{vec}
Simulation Loop:
for each i_{deg} **in** i_{vec} **do**
    $i \leftarrow \text{deg2rad}(i_{deg})$
    $e, \omega \leftarrow \textsc{FrozenOrbitEccentricity}(a, i, \omega_{ref})$ ▷ Execute Alg.14
    if e is not None **then**
        Append e to e_{vec}, Append ω to ω_{vec}
    else
        Append NaN to e_{vec}, ω_{vec}
    end if
end for
Post-Processing: ▷ Store the LFO results
Filter $i_{vec}, e_{vec}, \omega_{vec}$ to remove NaN values
$LFO \leftarrow \text{ColumnStack}(i_{vec}, e_{vec}, \omega_{vec})$
Save LFO to binary file (based on value of a)
Visualization: ▷ Inclination-Eccentricity Diagram
Plot scatter: $x = i_{vec}$, $y = e_{vec} \cdot \sin(\omega_{vec})$
Save figure: "LFO_a[altitude].png"

to use a lower number of harmonics, while the drawbacks of this decision will be explained later when discussing the Inclination-Eccentricity diagrams we obtained.

Finally, the latest algorithm is used in the main code `Simulations.py` to retrieve the values of the orbital elements to initialize the propagation of the trajectory. The main advantage of this code's logic is that it is necessary to calculate the eccentricity of the frozen orbit only once, because the results are stored in dedicated `numpy` matrices and it is possible to access the results whenever they are needed.

Algorithm 16 Retrieve Frozen Orbit Elements

Require: Semi-major axis a, Inclination i
Ensure: Eccentricity e, Argument of periapsis ω

function GET_LFO_ELEMENTS(a, i)
  Process inputs: ▷ It is assumed a in meters and i in radians
  $i_{deg} \leftarrow \text{round}(\text{rad2deg}(i), 1)$
  $a_{km} \leftarrow \text{int}(a/1000)$
  Load Data Matrix:
  $Path \leftarrow$ ".../LFO_results/LFO_a" + string(a_{km}) + ".npy"
  if File at $Path$ does not exist **then**
    return None, **None**
  end if
  $LFO_Matrix \leftarrow \text{LoadNumpy}(Path)$
  Search for Inclination Match:
  $I_{vec} \leftarrow LFO_Matrix[:, 0]$ ▷ Extract inclination column
  $Matches \leftarrow$ Find indices where $|I_{vec} - i_{deg}| < 10^{-5}$
  if $Matches$ is empty **then**
    return None, **None**
  end if
  $idx \leftarrow Matches[0]$
  Extract Elements:
  $e \leftarrow LFO_Matrix[idx, 1]$
  $\omega_{deg} \leftarrow LFO_Matrix[idx, 2]$
  return $e, \text{deg2rad}(\omega_{deg})$
end function

2.1.4 `Lunar_Constellations.py`

The following functions have been created to generate the initial states of the satellites belonging to a constellation, in order to create a state vector matrix to

feed to the orbital propagator. The initial states are first computed in the form of Keplerian Orbital Elements $[a, e, i, \Omega, \omega, \nu]$, and later converted in the main `Simulations.py` before integration.

Algorithm 17 Generation of Walker Delta Constellation

Require: Altitude h, Inclination i, Total Satellites T, Planes P, Phasing Factor F
Ensure: State Matrix $\mathcal{X}$ $(T \times 6)$ containing $[a, e, i, \Omega, \omega, \nu]$

Input Validation:
if $T \pmod P \neq 0$ **then**
    Error: "T must be divisible by P"
end if
Initialization:
Retrieve R_{moon} from planetary constants
$S \leftarrow T/P$ ▷ Satellites per plane
$a \leftarrow R_{moon} + h$
$e, \omega \leftarrow \text{GetLFOElements}(a, i)$ ▷ Retrieve frozen orbit parameters
Calculate Spacings:
$\Delta\Omega \leftarrow 2\pi/P$ ▷ Node spacing (Delta)
$\Delta S \leftarrow 2\pi/S$ ▷ In-plane (Mean Anomaly) spacing
$\Delta\Phi \leftarrow F \times (2\pi/T)$ ▷ Inter-plane phase offset
Initialize $\mathcal{X}$ as zeros matrix of size $(T, 6)$
$k \leftarrow 0$ ▷ Global satellite index
Generation Loop:
for $p \leftarrow 0$ **to** $P - 1$ **do** ▷ Loop over planes
    $\Omega \leftarrow p \times \Delta\Omega$
    for $s \leftarrow 0$ **to** $S - 1$ **do** ▷ Loop over satellites in plane
        $M \leftarrow (s \times \Delta S + p \times \Delta\Phi) \pmod{2\pi}$
        $\nu \leftarrow \text{MeanToTrueAnomaly}(M, e)$ ▷ Execute Alg.22
        $\mathcal{X}[k] \leftarrow [a, e, i, \Omega, \omega, \nu]$
        $k \leftarrow k + 1$
    end for
end for
return $\mathcal{X}$

The Walker Delta generation requires as input the altitude and inclination desired, as well as the parameters defined by Walker: T, P, and F. By definition, it is necessary first to ensure that T is divisible by P, because of the simmetry required in each orbital plane. Additionally, to adapt the concept of constellations to LFOs, the eccentricity and argument of periapsis are retrieved from the saved dataset containing the matching between inclination and frozen orbital elements. Due to

the fact that Walker Constellations are assumed to be circular, the adaptation to frozen orbits where the eccentricity is not null, requires that the symmetric angular spacing within the same orbital plane must be done by Mean Anomaly instead of the True Anomaly. A custom function converts M_e to ν before saving the State Matrix χ. The node spacing logic is the same described in Sec.1.2, therefore the angular spacing is constant and defined as $\Delta\Omega = 2\pi/P$: it might seem that if the number of planes is even (i.e. $P = 2$), then the orbital planes will be coincident for polar orbits, while for different inclinations the planes will be shifted.

Algorithm 18 Generation of Walker Star Constellation

Require: Altitude h, Inclination i, Total Satellites T, Planes P, Phasing Factor F
Ensure: State Matrix $\mathcal{X}$ $(T \times 6)$ containing $[a, e, i, \Omega, \omega, \nu]$

Input Validation:
if $T \pmod P \neq 0$ **then**
    Error: "T must be divisible by P"
end if
Initialization:
Retrieve R_{moon} from planetary constants
$S \leftarrow T/P$
$a \leftarrow R_{moon} + h$
$e, \omega \leftarrow \text{GetLFOElements}(a, i)$
Calculate Spacings:
$\Delta\Omega \leftarrow \pi/P$ ▷ Node spacing (Star)
$\Omega_{offset} \leftarrow \Delta\Omega/2$ ▷ Centering offset
$\Delta S \leftarrow 2\pi/S$
$\Delta\Phi \leftarrow F \times (2\pi/T)$
Initialize $\mathcal{X}$ of size $(T, 6)$
$k \leftarrow 0$
Generation Loop:
for $p \leftarrow 0$ **to** $P - 1$ **do**
    $\Omega \leftarrow \Omega_{offset} + (p \times \Delta\Omega)$
    for $s \leftarrow 0$ **to** $S - 1$ **do**
        $M \leftarrow (s \times \Delta S + p \times \Delta\Phi) \pmod{2\pi}$
        $\nu \leftarrow \text{MeanToTrueAnomaly}(M, e)$
        $\mathcal{X}[k] \leftarrow [a, e, i, \Omega, \omega, \nu]$
        $k \leftarrow k + 1$
    end for
end for
return $\mathcal{X}$

The main difference between the Walker Delta and the Walker Star generation

Algorithm 19 Generation of Streets of Coverage (SoC) Constellation

Require: Altitude h, Inclination i, Minimum Elevation Angle ε_{min} (deg)
Ensure: State Matrix $\mathcal{X}$, Parameters T, P, F

Derive Plane Parameters:
Convert ε_{min} to radians
$L_{max} \leftarrow \arccos\left(\frac{R_{moon}}{R_{moon}+h}\cos\varepsilon_{min}\right) - \varepsilon_{min}$
$S \leftarrow \lfloor \pi / L_{max} \rfloor + 1$ ▷ Optimal number of satellites per plane
$\Delta S \leftarrow 2\pi / S$
if $\Delta S \geq 2L_{max}$ **then**
    Error: "Intra-plane gaps exist"
end if
Calculate Street Width: $L_{street} \leftarrow \arccos(\frac{\cos(L_{max})}{\cos(0.5\Delta S)})$
Derive Constellation Geometry:
$m \leftarrow \lfloor \frac{\pi - L_{street} + L_{max}}{L_{street} + L_{max}} \rfloor + 1$ ▷ Optimal number of planes
$P \leftarrow m$
$\Delta\Omega \leftarrow \pi / m$ ▷ Constellation seam
$\Omega_{offset} \leftarrow \Delta\Omega / 2$
Check Coverage: $D_{max} \leftarrow 2\arcsin(\sin(0.5\Delta\Omega)\sin(i))$
if $D_{max} > L_{max} + L_{street}$ **then**
    Error: "Insufficient planes for continuous coverage"
end if
Derive Phasing:
$\Delta\Phi \leftarrow 2\arctan(\tan(0.5\Delta\Omega)\cos(i))$
$T \leftarrow S \times m$
$F \leftarrow (\Delta\Phi \times T)/2\pi$ ▷ F is not an integer
Orbit Initialization:
$a \leftarrow R_{moon} + h$
$e, \omega \leftarrow$ GetLFOElements(a, i)
Initialize $\mathcal{X}$ of size $(T, 6)$
$k \leftarrow 0$
Generation Loop:
for $p \leftarrow 0$ **to** $P - 1$ **do**
    $\Omega \leftarrow \Omega_{offset} + (p \times \Delta\Omega)$
    for $s \leftarrow 0$ **to** $S - 1$ **do**
        $M \leftarrow (s \times \Delta S + p \times \Delta\Phi) \pmod{2\pi}$
        $\nu \leftarrow$ MeanToTrueAnomaly(M, e)
        $\mathcal{X}[k] \leftarrow [a, e, i, \Omega, \omega, \nu]$
        $k \leftarrow k + 1$
    end for
end for
return $\mathcal{X}, T, P, F$

is the logic of the node spacing: in the second case the ascending nodes of the orbital planes are evenly distributed in the interval $[0, \pi]$ along the equator, unlike the Walker Delta pattern where the nodes were evenly distributed along the [0,2π] interval.

The generation of SoC constellations is strictly dependant on the performance of the payload, especially the FOV. To analyse the performance of the constellations based purely on the initial conditions of the orbits where the satellites are deployed, we assume the Minimum Elevation Angle to be constant as $\varepsilon_{min} = 10$ deg, and the payload performance is adjusted as a consequence. In this way, the MECA and the Swath Width are a function of the only altitude, as calculated by the L_{max} step of the following algorithm. The equations described at Sec.1.2 are implemented in the Alg.19 to generate the SoC constellation according to their definition. Additionally, the Walker parameters (T,P,F) are extracted by the function as outputs, for a better comparison with analogous Walker constellations at the fixed altitude and inclination. In this case, due to the fact that the purpose of the SoC is to provide continuous coverage, unlike the Walker constellations whose purpose is to be geometrically symmetric, the phasing factor F will not be an integer but rather a float number. The node spacing is similar to the Walker Star: after computing the minimum number of orbital planes that ensure the overlapping of the SoC in the $[0, \pi]$ seam, the planes are evenly spaced in the interval in order to evenly distribute the excess coverage provided by the respected inequalities. The seam is cut into m slices, and the node of each plane is placed in the middle of slice.

2.1.5 `Lunar_RF_Transformations.py`

This code is a list of functions that are used in the main logic to rotate position and velocity vectors, to convert the state vector from orbital elements to cartesian coordinates and also convert a state vector from a reference frame to another.

The first function, described in Alg.20, is used to take as input the Keplerian orbital elements $[a, e, i, \Omega, \omega, \nu]$ and return as the output the state vector in cartesian coordinates $[x, y, z, v_x, v_y, v_z]$, expressed in the reference frame where the orbital elements are defined (Fig.1.4). First the code checks if the orbit is closed ($e < 1$), and continues by applying the definition of semi-latus rectum and radius magnitude of the conic orbit. Applying Eq.(1.6), the position and velocity vectors in the perifocal frame are computed. It is worth mentioning that the velocity components of the step 11 are derived using the vis-viva equation (conservation of mechanical energy), therefore it is a velocity vector expressed in an inertial reference frame, regardless of its orientation.

Algorithm 20 Conversion from Keplerian Elements to Cartesian State Vector

Require: Keplerian Elements $\boldsymbol{\alpha} = [a, e, i, \Omega, \omega, \nu]$, Gravitational Parameter μ
Ensure: Cartesian State Vector $\boldsymbol{X} = [\boldsymbol{r}, \boldsymbol{v}]^T$ in the inertial reference frame

Unpack Elements:
$a, e, i, \Omega, \omega, \nu \leftarrow \boldsymbol{\alpha}$
Compute Orbital Parameters:
if $e = 1.0$ **then**
    Error: Parabolic orbits not supported
end if
$p \leftarrow a(1 - e^2)$ ▷ Semi-latus rectum
$r_{norm} \leftarrow p/(1 + e\cos\nu)$ ▷ Radius magnitude
Compute State in Perifocal Frame (PQW):
$\boldsymbol{r}_{PQW} \leftarrow [r_{norm}\cos\nu,\ r_{norm}\sin\nu,\ 0]^T$
$\boldsymbol{v}_{PQW} \leftarrow \sqrt{\frac{\mu}{p}} \cdot [-\sin\nu,\ (e + \cos\nu),\ 0]^T$
Rotation to Definition Frame:
Compute rotation matrix $R_{313} = R_z(\Omega)R_x(i)R_z(\omega)$
$\boldsymbol{r} \leftarrow R_{313} \cdot \boldsymbol{r}_{PQW}$
$\boldsymbol{v} \leftarrow R_{313} \cdot \boldsymbol{v}_{PQW}$
$\boldsymbol{X} = \text{concatenate}(\boldsymbol{r}, \boldsymbol{v})$
return $\boldsymbol{X}$

The orbital elements, for Earth applications, are usually usually defined in the ECI reference frame, while for the Moon it is more convenient to measure the angle of RAAN from the prime meridian of the Moon (*longitude of the ascending node*) and the inclination from the equatorial plane: the rotation angles are defined in the PALRF reference frame (body-fixed). The prime meridian of the Moon, in fact, is considered by convention the intersection of the equator with the axis of major inertia of the planet, hence the longitude is measured in the PALRF.

The next function does the opposite process: Alg.21 converts a state vector in cartesian coordinates in the 6 Keplerian orbital elements. This process requires particular attention, because the code needs to handle singularities, like circular or equatorial orbits and apply the standard conventions for the undefined angles. In the normal case, when all the orbital elements are defined, it is necessary to first compute the energy of the orbit from the magnitude of the position and velocity vectors, applying the vis-viva equation. Then it is possible to proceed computing the fundamental vectors that define the orbit size and orientation, the angular momentum, node and eccentricity vectors. From these vectors it is possible to extract the RAAN, the argument of periapsis and the true anomaly, like demonstrated in [10].

Algorithm 21 Conversion from Cartesian State Vector to Keplerian Elements

Require: Cartesian State Vector $\boldsymbol{X} = [\boldsymbol{r}, \boldsymbol{v}]^T$, Gravitational Parameter μ
Ensure: Keplerian Elements $\boldsymbol{\alpha} = [a, e, i, \Omega, \omega, \nu]$
Compute Magnitudes and Energy:
$r \leftarrow \|\boldsymbol{r}\|, \quad v \leftarrow \|\boldsymbol{v}\|$
Specific Energy $\mathcal{E} \leftarrow \frac{v^2}{2} - \frac{\mu}{r}$
Semi-major axis $a \leftarrow -\mu/(2\mathcal{E})$
Compute Fundamental Vectors:
Angular Momentum $\boldsymbol{h} \leftarrow \boldsymbol{r} \times \boldsymbol{v}$
Node Vector $\boldsymbol{n} \leftarrow \hat{k} \times \boldsymbol{h}$
Eccentricity Vector $\boldsymbol{e}_{vec} \leftarrow \frac{1}{\mu}\left((v^2 - \frac{\mu}{r})\boldsymbol{r} - (\boldsymbol{r} \cdot \boldsymbol{v})\boldsymbol{v}\right)$
$e \leftarrow \|\boldsymbol{e}_{vec}\|$
Compute Angles:
Inclination $i \leftarrow \arccos(h_z/\|\boldsymbol{h}\|)$
RAAN $\Omega \leftarrow \arccos(n_x/\|\boldsymbol{n}\|)$
if $n_y < 0$ **then** $\Omega \leftarrow 2\pi - \Omega$
end if
Argument of Periapsis $\omega \leftarrow \arccos(\frac{\boldsymbol{n} \cdot \boldsymbol{e}_{vec}}{\|\boldsymbol{n}\| e})$
if $e_z < 0$ **then** $\omega \leftarrow 2\pi - \omega$
end if
True Anomaly $\nu \leftarrow \arccos(\frac{\boldsymbol{e}_{vec} \cdot \boldsymbol{r}}{er})$
if $\boldsymbol{r} \cdot \boldsymbol{v} < 0$ **then** $\nu \leftarrow 2\pi - \nu$
end if
Handle Singularities:
If $e \approx 0$ or $i \approx 0$, apply standard conventions (set undefined angles to 0)
return $\boldsymbol{\alpha} = [a, e, i, \Omega, \omega, \nu]$

Another useful function is the conversion from mean to true anomaly, described in Alg.22. Even though this function is defined in this subsection, it has been already called in Alg.17, 18 and 19 to initialize the orbital elements for all the satellites of the constellation, after the in-plane spacing relies upon the distribution over the mean anomaly. The function uses the Newton-Raphson method to find numerically the root of the transcendental Kepler's Equation in Eq.(1.10), which doesn't have closed-form solution. The numerical method solves for the eccentric anomaly and then applies the formula to derive the true anomaly, avoiding the quadrant check.

Algorithm 22 Conversion from Mean Anomaly to True Anomaly

Require: Mean Anomaly M, Eccentricity e, Tolerance ϵ
Ensure: True Anomaly ν
Input Check:
$M \leftarrow M \pmod{2\pi}$
if $e \geq 1$ **then return** Error (Non-elliptical)
end if
Solve Kepler's Equation (Newton-Raphson):
$E_0 \leftarrow M$ ▷ Initial guess
repeat
    $f \leftarrow E - e\sin(E) - M$
    $f' \leftarrow 1 - e\cos(E)$
    $E \leftarrow E - \frac{f}{f'}$
until $|f/f'| < \epsilon$
Compute True Anomaly:
$\beta \leftarrow \sqrt{(1+e)/(1-e)}$
$\nu \leftarrow 2\arctan(\beta \cdot \tan(E/2)) \pmod{2\pi}$
return ν

Algorithm 23 Geometric-Only Frame Transformation

Require: Input State $\boldsymbol{X}_{in} = [\boldsymbol{r}_{in}, \boldsymbol{v}_{in}]^T$, Source Frame F_{src}, Target Frame F_{dest}, Epoch t
Ensure: Transformed State $\boldsymbol{X}_{out}$
Retrieve Rotation Matrix:
Call SPICE kernel to get 3×3 position rotation matrix:
$R_{3\times3} \leftarrow \text{PXFORM}(F_{src}, F_{dest}, t)$
▷ Matrix accounts for instantaneous orientation only
Apply Rotation:
$\boldsymbol{r}_{out} \leftarrow R_{3\times3} \cdot \boldsymbol{r}_{in}$
$\boldsymbol{v}_{out} \leftarrow R_{3\times3} \cdot \boldsymbol{v}_{in}$ ▷ Velocity direction rotated, magnitude preserved
return $\boldsymbol{X}_{out} = [\boldsymbol{r}_{out}, \boldsymbol{v}_{out}]^T$

Last function (Alg.23) performs a geometric vector rotation, just by multiplying the input vector for the desired rotation matrix at time t. The user should define the name of the source and the target reference frame as defined by the NASA SPICE notation, then the rotation matrix at epoch t is retrieved with the function `spiceypy.pxform`, which stands for position transform. The rotation is applied to the 3-elements position vector and velocity vector separately, as the orientation matrix is a 3x3 matrix. This function is useful when we want to simply express

the same vector in another coordinate system, preserving the magnitude of the velocity vector without adding any undesired components given by the non-inertial phenomena. The Alg.24, instead, uses the `spiceypy.sxform` to transform the entire state vector from the origin reference frame to the target. If one of the frame is not inertial, the transformation matrix will account for the rotation rate between the two coordinate systems.

Algorithm 24 Full State Vector Transformation via SPICE

Require: Input State $\boldsymbol{X}_{in}$, Source Frame F_{src}, Target Frame F_{dest}, Epoch t
Ensure: Transformed State $\boldsymbol{X}_{out}$ in F_{dest}
Retrieve Transformation Matrix:
Call SPICE kernel to get 6×6 state transformation matrix:
$T_{6\times6} \leftarrow \text{SXFORM}(F_{src}, F_{dest}, t)$
▷ Matrix accounts for rotation and rotation rate
Apply Transformation:
$\boldsymbol{X}_{out} \leftarrow T_{6\times6} \cdot \boldsymbol{X}_{in}$
return $\boldsymbol{X}_{out}$

2.1.6 `Simulations.py`

The main simulation code is called `Simulations.py` and it performs the full analysis of the dynamics of a user designed Lunar Constellation. The logic of the code is described in Alg.25: the user enters the main parameters of the constellation in the inputs, such as the altitude h and the inclination i of the orbits, and the constellation pattern's name, being one of the Earth's constellations described in Sec.1.2. Depending on the constellation type, other parameters are asked to the user, for example the number of satellites, the number of planes and the phasing factor in the case of Walker, or the minimum elevation angle in the case of SoC. The functions described by Alg.17,18 and 19 generate the initial states matrix which contains, for each row, the 6 orbital elements of the initial condition of the spacecraft. For each satellite, its initial state is transformed first in cartesian state vector, where the axes will match the Mean-Earth reference frame, and later rotated to the inertial J2000 frame. The simulation can start by propagating the trajectory of each satellite in the inertial frame, while the total perturbing acceleration is computed in the Principal Axis frame as shown in Alg.10. All the trajectories are store in a 3-dimensional array, with size T, N_{steps},6) being the total number of satellites, the number of time steps and the 6 degrees of freedom of the state vector, for an easier post processing of the data.

Algorithm 25 Full Lunar Constellation Simulation

Require: Altitude h, Inclination i, Constellation Type C_{type}, Simulation Duration T_{sim} ▷ User defined
Ensure: Trajectories $\mathcal{T}$, Stability Metrics, Performance Figures
Initialization:
Load SPICE kernels (Planetary Constants, Ephemerides, Frames)
Retrieve Moon constants: $\mu_{moon}, R_{moon}, \omega_{moon}$
Set Simulation's Start Epoch: $t_0 \leftarrow$ "2026-01-01 00:00:00 UTC"
$t_{end} \leftarrow t_0 + T_{sim}$
$a \leftarrow R_{moon} + h$
Constellation Generation: ▷ $\mathcal{OE}_{init}$ stands for Initial Orbital Elements
if C_{type} = "Streets of Coverage" **then**
    Input ϵ_{min} (Min Elevation Angle)
    $\mathcal{OE}_{init}, T, P, F \leftarrow \textsc{GenerateSoC}(h, i, \epsilon_{min})$
else if C_{type} = "Walker Star" **then**
    Input T, P, F
    $\mathcal{OE}_{init} \leftarrow \textsc{GenerateWalkerStar}(h, i, T, P, F)$
else if C_{type} = "Walker Delta" **then**
    Input T, P, F
    $\mathcal{OE}_{init} \leftarrow \textsc{GenerateWalkerDelta}(h, i, T, P, F)$
end if
Frame Transformation (Initial State):
Initialize inertial state array $\mathbf{X}_{init}$ of size $(T, 6)$
for $s \leftarrow 0$ **to** $T - 1$ **do**
    $\mathbf{X}_{PA} \leftarrow \textsc{KeplerianToState}(\mathcal{OE}_{init}[s], \mu_{moon})$ ▷ Principal-Axes Frame
    $\mathbf{X}_{J2000} \leftarrow \textsc{GeometricTransform}(\mathbf{X}_{PA}, \text{"MOON_PA"}, \text{"J2000"}, t_0)$
    $\mathbf{X}_{init}[s] \leftarrow \mathbf{X}_{J2000}$
end for

The visualization of the results is discussed in the following section, where the strategy to analyse the dynamics of the constellations is delved. It is described how the defined performance and stability are computed started from the post-processing of the trajectories and why these metrics are important when analysing the lunar constellations.

Algorithm 26 Full Lunar Constellation Simulation (Part 2)

Numerical Propagation:
Define time vector $\mathbf{t}_{eval}$ from t_0 to t_{end}
Initialize Trajectory Tensor $\mathcal{T}$ of size $(T, N_{steps}, 6)$
for $s \leftarrow 0$ **to** $T-1$ **do**
    $\mathcal{T}[s] \leftarrow \text{IntegratePerturbedKR2BP}(\mathbf{X}_{init}[s], [t_0, t_{end}], \mu_{moon}, \mathbf{t}_{eval})$
    ▷ Includes Lunar Gravity (C_{nm}, S_{nm}) and Earth 3rd Body
end for
Post-Processing & Analysis:
Initialize Orbital Elements Tensor $\mathcal{OE}_{hist}$
for $s \leftarrow 0$ **to** $T-1$, $t \leftarrow 0$ **to** $N_{steps}-1$ **do**
    $\mathbf{X}_{curr} \leftarrow \mathcal{T}[s, t]$
    $\mathbf{X}_{PA} \leftarrow \text{GeometricTransform}(\mathbf{X}_{curr}, \text{"J2000"}, \text{"MOON_PA"}, \mathbf{t}_{eval}[t])$
    $\mathcal{OE}_{hist}[s, t] \leftarrow \text{StateToKeplerian}(\mathbf{X}_{PA}, \mu_{moon})$
end for
Metric Computation:
Compute Relative Energy Error $\Delta\mathcal{E}/\mathcal{E}_0$
Compute Perilune Altitude $h_p(t) = a(1-e) - R_{moon}$
Compute Inter-satellite Distances $D_{ij}(t)$ and Global Min Distance
Compute Relative Geometry Drifts (Mean Anomaly Spacing, RAAN Spacing)
Visualization:
Generate Stability Plots (SMA, Eccentricity Vector, Inclination)
Generate Safety Plots (Perilune survival, Collision avoidance)
Save Figures to results directory

2.2 Constellations Performance&Stability Metrics

The following subsections explain which metrics have been displayed at the end of the simulation to evaluate the performance and the stability of the constellation. It is important to notice that the output trajectories of the orbital propagator are transformed to the Principal-Axes reference frame with a geometric rotation described by Alg.23, because this is the frame in which the orbital elements are defined. In this way the inclination is defined with respect to the equatorial plane and the RAAN is measured in the equatorial plane from the prime meridian, therefore it is more appropriate to call it longitude of the ascending node.

2.2.1 Constellation Survival and Degradation

The first group of figures show the capability of the constellation to survive after a long propagation time without crashing on the planet's surface. In particular, we need to verify if the altitude of the satellites decrease after 1-year simulations.

Specific Mechanical Energy Variation

This plot displays the relative variation of the spacecraft's specific mechanical error $\mathcal{E}$ over time with respect to the initial energy at time $t = 0$. The specific mechanical energy, as defined by Eq.(1.4), is constant for a Keplerian orbit. In a high-fidelity orbital simulator, where the perturbations of the lunar gravity and the Earth's third-body interactions are added, the forces are conservative in the inertial frame and for this reason the expected behaviour of the specific mechanical energy is a physical oscillation.

The energy error is computed by extracting the semi-major axis from the orbital elements array, the instantaneous mechanical energy is computed from the semi-major axis at epoch t, and the relative energy error is defined as:

$$\Delta\varepsilon(t) = \frac{\varepsilon(t) - \varepsilon_0}{\varepsilon_0} \tag{2.1}$$

The mean energy variation of the constellation is computed as the average of the satellite i-th energy and plotted with a solid red line, while the error of the single satellite is plotted in the background with a fainted grey line. This figure is important to visualize because it is primarily a **validation tool** of the numerical integrator: in fact, for an unperturbed Keplerian orbit, the mechanical energy is conserved and a linear drift means that the integrator is accumulating numerical error, indicating that the step-size is too large or that the method is not accurate.

Semi-major Axis Statistics

This plot shows the evolution in time of the global semi-major axis of the constellation, which means the mean semi-major axis value among all the satellites. Additionally, the minimum and the maximum value of a is displayed at each instant of time to have an understanding of the maximum de-synchronization of the orbital periods between the satellites of the constellation. In fact, the perturbations such as third-body perturbations can add more energy into an orbit, leading to significant changes in the satellite dynamics and contributing to the **degradation or growth** of the constellation. The time evolution of the semi-major axis is also visualized by creating a subplot for each of the planes, allowing us to visualize more easily which

satellite is drifting from the initial deployment of the constellation, as demonstrated by Fig.3.19.

Perilune Altitude Statistics

This metric measures the evolution in time of the perilune altitude, which is the lowest altitude the satellites reach during their orbit. It is important to visualize the time evolution because it shows at each instant of time the minimum distance from a spacecraft to the surface of the planet and therefore it is the critical safety check for the constellation **survival** and a crash detection check. The perilune altitude is calculated as:

$$h_p = a\,(1 - e) - R_{\leftmoon} \tag{2.2}$$

Typically, the lunar mascons often increase eccentricity while keeping the semi-major axis roughly constant, leading to h_p decreasing in time. This is the reason why the global minimum altitude is displayed to check at each instant of time what is the minimum perilune altitude of the constellation, as well as the planes breakdown to identify which of the satellite is risking the most a collision with the surface (visualized by a red line).

2.2.2 Frozen Stability Analysis

The second group of figures represent the stability of the orbits to withstand the prolonged exposition to the gravitational perturbations of the Moon and the Earth, therefore the capability of the orbits to remain frozen for the entire duration of the simulation.

Eccentricity Vector Phase-Space

The eccentricity vector phase-space is a standard tool to analyze the frozen stability of a lunar orbit. It is a polar plot where the x-axis is $(e \cdot \cos\omega)$ and the y-axis is $(e \cdot \sin\omega)$, which are the components of the eccentricity vector in the perifocal frame. The frozen orbit should appear as single point or a closed loop in the phase-space, meaning that the orbit's shape and orientation is stationary. If the evolution of the vector is an open loop which spirals out of the starting point, the orbit is unstable and the initial orbital elements (a, e, i, ω) do not lead the spacecraft to a locked configuration. To visualize this feature, the orbital elements are extracted and the components of the eccentricity vector are calculated as:

$$e_x = e\cos\omega \qquad e_y = e\sin\omega \tag{2.3}$$

It is decided to extract the data only for the first satellite per plane, assuming all the satellites in the same orbit shall follow the same path in the phase-space and avoiding the clutter of the lines. Additionally, the frequency of the data is smoothed out to neglect the short-period oscillations which create jitter in the solution, leaving only the **secular frozen stability**, meaning that only long-period drift is visualized. The arrays are filtered with the function `scipy.uniform_filter1d`, which takes one element of the array every 10 orbital periods. Also the iso-eccentricity grid is plotted, as well as the raw data in faint lines to understand the entity of the short-period oscillations.

Argument of Perilune Evolution

This plot displays the evolution in time of the argument of peri-apsis for all the satellites of the constellation. The value of the angle is wrapped from 0 to 360 deg to distinguish between **libration and circulation** of the orbit. Libration means the argument of periapsis oscillates around the ideal value (90 deg or 270 deg), meaning the orbit is frozen; if the angle drifts linearly and continuosly it means that the orbit is unstable or worse, not frozen as the periapsis circulates along the orbit. To better visualize the oscillations, dashed lines corresponding to the ideal values of the argument of periapsis is added, which identify the theoretical solution of the frozen orbit.

Kozai-Lidov Coupling

The Kozai-Lidov coupling is a particular phenomena in which the perturbing acceleration given by C_{22} term of the lunar gravity field interacts with the perturbing acceleration derived by the third-body attraction of the Earth[71]. This creates a coupling between the eccentricity and the inclination of the orbit, given by the conservation of the z-component of the angular momentum due to the axi-symmetric gravitational field:

$$H = \sqrt{\mu_{\leftmoon}\, a\,(1 - e^2)}\cos i \tag{2.4}$$

To visualize the Kozai-Lidov resonance, the eccentricity is plot on the x-axis and the inclination on the y-axis, both smoothed out with the same logic of the phase-space plot to cancel out the jitter and avoid cluttering the lines. If the **eccentricity-inclination resonance** is strong, e can grow too large leading to high instability of the frozen condition and possibly a crash of the satellite on the surface. By plotting the Kozai-Lidov coupling for at least one satellite of each orbital plane, it is possible to identify a correlation between the eccentricity-inclination resonance with the longitude of the ascending node of the plane, showing which planes suffer the most from this phenomena.

2.2.3 Geometry Maintenance (Station-Keeping)

The third group of figures represent the maintenance of the geometric pattern of the constellation, selected before initializing the orbital elements of the spacecraft. The geometric stability is strictly related to the coverage performances and to the station-keeping analysis.

Inclination Statistics

This plot shows how the orbital planes are with respect to the Moon's equator over time. It is important to visualize the inclination drift because it exposes coverage gaps in the constellation, creating a distortion of the geometric pattern and potentially creating blind spots on the surface where no satellite is available. The global statistics are displayed by computing at each instant of time the average inclination of the constellation and filling up the gap between the global minimum inclination and the global maximum, helpful to identify the maximum distortion of the constellation and estimate the **across-track station-keeping**. The single spacecraft data is plotted plane by plane to understand if, among the satellites in the same orbit, some are drifting away too much with respect to the initial condition.

Relative Mean Anomaly Drift

This plot displays the angular spacing error between adjacent satellites within the same orbital plane, also defined **in-plane phasing**. In a constellation, satellites must remain evenly spaced to mantain the symmetry of the geometric pattern and create a Street of Coverage without gaps. The mean anomaly of all the satellites is computed thanks to Alg.22 from the true anomaly, and then unwrapped to handle the operation of subtraction between an angle close to 0 degrees and another close to 360 degrees. Considering S the number of satellites in the same plane, the angular spacing drift of the i-th spacecraft is computed, with respect to the antecedent j-th (following the direction of rotation of the trajectory), as:

$$\Delta M_{i,j}(t) = (M_i(t) - M_j(t)) - (M_i(t_0) - M_j(t_0)) \tag{2.5}$$

If the relative angular spacing is positive, the two satellites are drifting apart, exposing potential coverage gaps or tightening the width of the SoC; otherwise, the two satellites are getting closer increasing the risk of collision. The index is also wrapped between first and last spacecraft to "close the loop" of the orbital plane.

Relative Node Spacing Drift

This plot shows the difference in the longitude of the ascending node between adjacent orbital planes. It checks if the planes are rotating (precessing or regressing) at the same rate because, due to the Moon's oblateness described by the zonal coefficient C_{20}, the nodes regress along the equator completing a full revolution in approximately one lunar month ($T_{\leftmoon}$ in Table 1.3). If adjacent planes have different semi-major axis or inclination, the consequence will be a different regression rate destroying the symmetric shape of the constellation, which leads to the creation of gaps in coverage.

The RAAN is extracted from the orbital elements output and the mean RAAN among all the satellites orbiting within the same plane is calculated. Then, the difference between the plane i-th and the antecedent plane j-th is computed as:

$$\Delta\Omega_{P_i-P_j}(t) = (\bar{\Omega}_{P_i}(t) - \bar{\Omega}_{P_j}(t)) - (\bar{\Omega}_{P_i}(t_0) - \bar{\Omega}_{P_j}(t_0)) \tag{2.6}$$

If the relative node drift overcomes a certain warning gap defined by mission requirements, it is necessary to actively control the **inter-plane station-keeping**.

2.2.4 Collision Avoidance Safety

The last group of figures represents the evaluation of the risk of collision among the satellites and it is critical for the mission failure.

Global Minimum Inter-Satellite Distance

This plot shows, for each instant of time, the global minimum distance between two satellites of the constellation, calculated as the minimum Euclidean distance between the position vectors of the spacecraft. For every satellite, the position vector $\vec{x} = [x, y, z]$ is extracted, a distance matrix $\mathcal{D}(t)$, with shape (number of satellites, number of satellites), is computed at every time step, where in each row i and column j the distance is:

$$d_{i,j}(t) = ||\vec{x_i}(t) - \vec{x_j}(t)||_2 \tag{2.7}$$

where $d_{i,i}$ is set to `inf` to consider in the calculation of the minimum only the distance from other satellites of the constellations. For each row, the minimum distance is computed and inserted in a matrix $\mathcal{D}_{min}$ with shape (num. satellites, num. time steps), where at the for each satellite (row i-th) and each time step (column k-th), the following value is inserted:

$$d_{min_{i,k}} = \min\left(d_{i,j}(t)\right) \tag{2.8}$$

The visualization of the global minimum distance ensures that satellites don't collide, or that they don't enter the selected collision avoidance safety radius (usually 1 km).

Chapter 3

Results

This chapter delves into the details of the lunar dynamics, concerning the search for frozen orbits, the verification of the orbital stability of the preliminary found LFOs, the dependency of the performance metrics on the number of satellites of the constellation. The first section describes the results of the double-averaging perturbation theory applied to the Lunar Gravity Field with the Hill's Third-Body acceleration, and the eccentricity-inclination diagrams are presented as a frozen orbits solution space for a wide range of altitude regimes. The second section analyzes the actual stability after a 1-year propagation period for a pool of 60 selected orbits, chosen within a range of altitudes and inclinations valuable for potential constellation applications. The results of the stability performances are presented to rank the orbits from the most suitable for stable and safe applications and in order to discard problematic orbits that can lead to a failure of the mission. Another feature of the dynamics that is revealed is the dependency of the constellations performances, in terms of SMA degradation and geometric pattern stability, on the initial orbital elements of each satellite. This result made it possible to compute the "Correction Maps", contour plots which link the mean SMA deviation and the inclination drift to the initial Keplerian orbital elements. Finally, 5 candidate orbits which showed the best stability results are chosen to verify the variability of the performance metrics as the number of satellites is increased. For each candidate, a Constellation Design Space is generated as a combination of the number of orbital planes (P) and the number of satellites in one plane (S), and the results are shown to identify some patterns regarding the geometric stability and safety of the constellations.

3.1 Search for Frozen Orbits

The first step of the analysis of the dynamics of Lunar Constellations is to find stable orbits where the gravitational perturbations do not lead to crashes on the

surface or where the orbital elements do not drift away too rapidly. For a complete set of altitudes, the perturbation theory of M.Lara [43] is applied to search for the existence of the frozen condition at every possible inclination. For this purpose, the code `Lunar_Frozen_Orbits.py` is used: the user selects the altitude from the Lunar surface at which to conduct the numerical search of the frozen condition, then a `for` cycle iterates along the inclinations in the interval [0.1,90] deg with step 0.1 deg. At each inclination step, Alg.15 is applied, and the set $(e_{frozen}, \omega_{frozen})$ is found and saved in the corresponding matrix.

The frozen orbits solution space is derived as an Inclination-Eccentricity diagram where $e < 0$ corresponds to the condition of $\omega = 270$ deg. On the x-axis of the diagram there is the inclination interval in degrees, on the y-axis the y-component of the eccentricity vector is reported, $e \cdot \sin\omega$. If the frozen condition is above the x-axis on the positive domain, it means $\omega = 90$ deg; otherwise, $\omega = 270$ deg. If a gap is observed in the solutions' space, it means the Brent's solver was not able to find a viable frozen eccentricity within the impact limit given by the chosen altitude. A first example of how the LFO solution space is presented is reported in Fig.3.1: the semi-major axis is the same as the quasi-frozen orbit of the Lunar Reconnaissance Orbiter[37] for a better comparison with other sources and research.

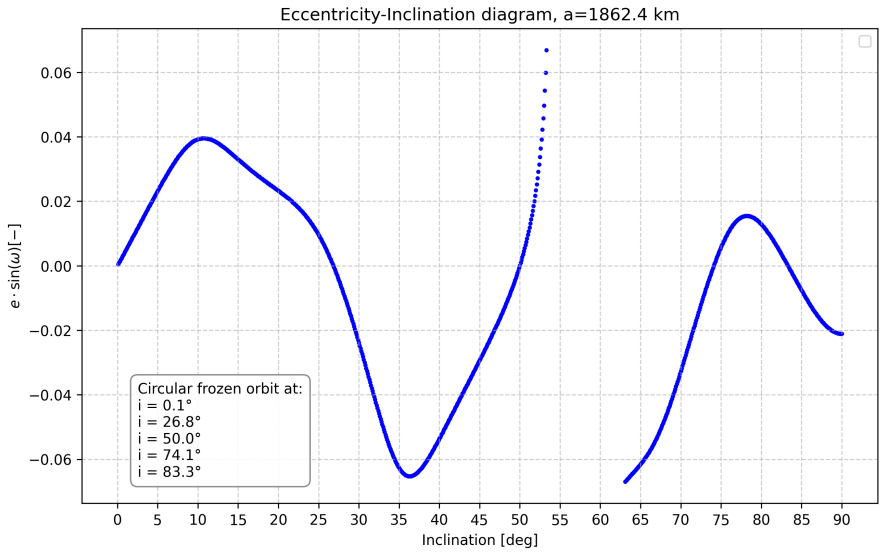


Figure 3.1: Frozen Orbits solutions space for semi-major axis $a = 1862.4$ km. Zonal Harmonics up to degree $n = 20$.

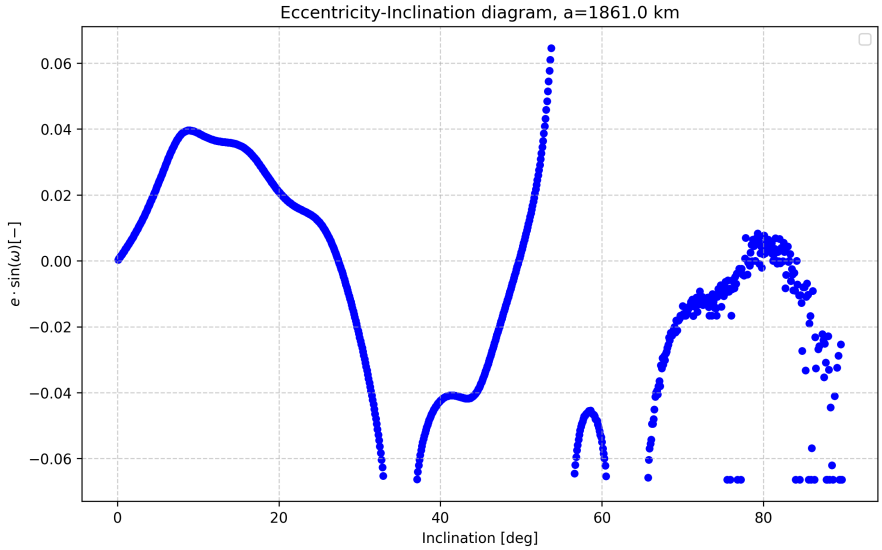


Figure 3.2: Frozen Orbits solutions space for semi-major axis $a = 1861\,\text{km}$. Zonal Harmonics up to degree $n = 50$.

The number of harmonics used to find the roots of $\dot{g}(e) = 0$ influences severely the computation time and the accuracy of the solution. For example, Fig.3.2 shows the solution space at approximately the same altitude of the previous example, in the case of considering all the zonal harmonics up to degree $n = 50$. It is true that the solution is qualitatively more accurate, because more harmonics reveal more local minimum and maximum in the behaviour of the eccentricity, and even new solutions exist in the region where previously no solutions were found, for example in the region around $i = 60$ deg. However, the solution space becomes quantitatively inaccurate, because the uncertain error on the harmonics coefficients grows bigger when multiplied by the helper math functions described by Eq.(1.24), because they imply factorials and combinations which become numerically imprecise when n is high. For these reasons, $n = 20$ has been chosen as a good compromise between the numerical accuracy of the Brent's solver and the precision of the frozen solution found.

To proceed with further analysis of the dynamics of lunar orbits, the search of the frozen eccentricity is conducted for every altitude of interest, to create a database for the frozen orbits where the correlation between semi-major axis a, inclination i, eccentricity e and argument of periapsis ω of a frozen orbit solution is created and stored. In the next sections, whenever an orbit is initialized by defining its altitude and inclination, the frozen eccentricity and argument of periapsis are recalled with Alg.16 without specifying it every time. The creation of this database gives a

qualitative understanding about the predominance of the Lunar Gravity Field with respect to the Earth Third-Body attraction: the following eccentricity-inclination diagrams demonstrate the altitude at which Zonal coefficients become neglectable and the Hill contribution becomes the main source of perturbation.

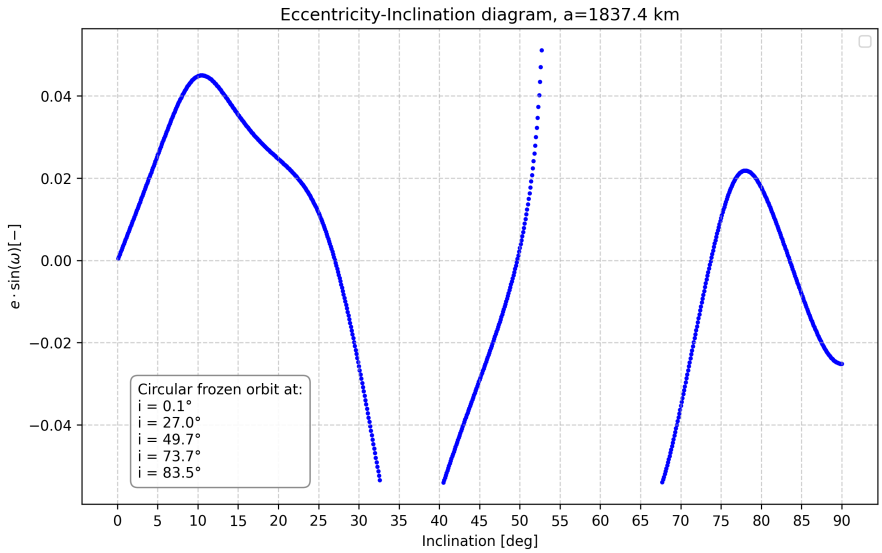


Figure 3.3: Frozen Orbits solutions space for altitude $h = 100\,\text{km}$.

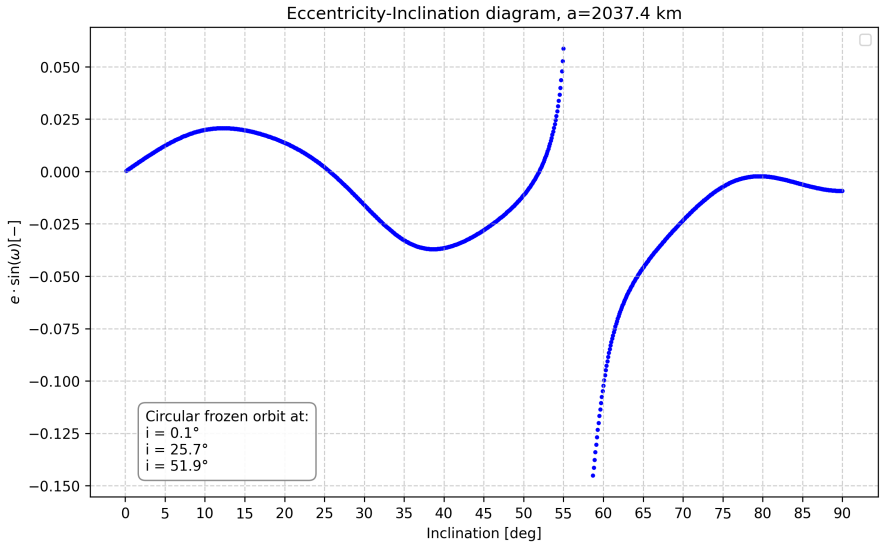


Figure 3.4: Frozen Orbits solutions space for altitude $h = 300\,\text{km}$.

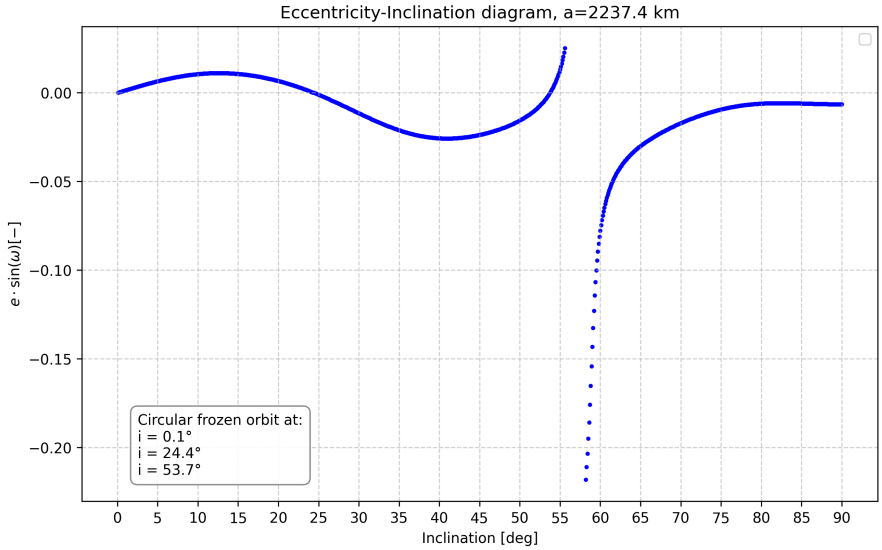


Figure 3.5: Frozen Orbits solutions space for altitude $h = 500\,\text{km}$.

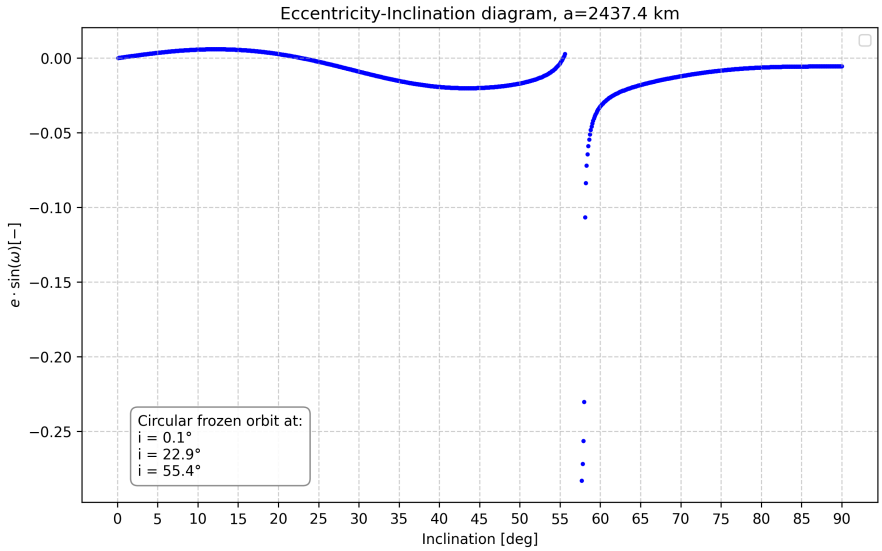


Figure 3.6: Frozen Orbits solutions space for altitude $h = 700\,\text{km}$.

For orbits with altitude below 700 km, the Eccentricity-Inclination diagram presents a frozen circular orbit when the inclination is zero, then the frozen eccentricity is found in the positive domain with a local maximum around $i = 10$ deg or 15 deg. As the inclination increase, the x-axis is always crossed at an inclination around $i = 25$ deg where another circular frozen orbit is individuated, and then

the eccentricity increases in the negative domain up to a local minimum around $i = 40$ deg (for $h = 100$ km, this local minimum exceeds the boundary of the impact eccentricity). The solution space crosses again the x-axis towards the positive domain, usually around $i = 50$ deg, then a gap without solutions exist usually around $i = 57$ deg, and the gap gets wider in the lowest altitudes because negative solutions appear only if the degree of the harmonics is increased like in Fig.3.2.

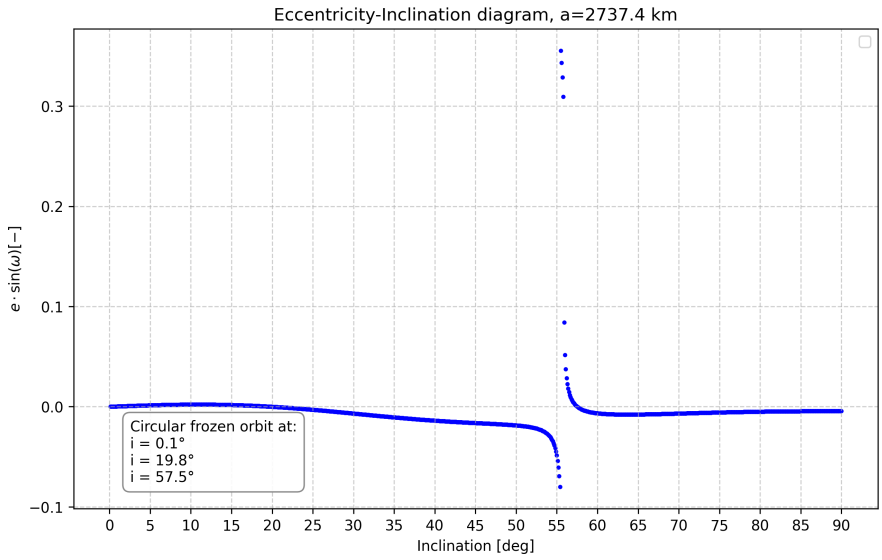


Figure 3.7: Frozen Orbits solutions space for altitude $h = 1000$ km.

Above 700 km of altitude, the impact eccentricity becomes higher and the region where the solution is searched becomes wider. For this reason, the solution space looks flatter with very low frozen eccentricities with respect to the maximum allowed by the physics. The interval with no solutions still exists at an inclination near $i = 57$ deg, but is important to mention that the search of frozen orbits presented in this thesis is preliminary and approximated, therefore a dot of the solution space does not guarantee that the orbit will be frozen after a long period of time, or that a frozen orbit is locked in a stable configuration. For this reason, a stability analysis is conducted to verify if the frozen solution found with a root-finding method is verified when the orbit is propagated with the high-fidelity integrator described by Alg.5.

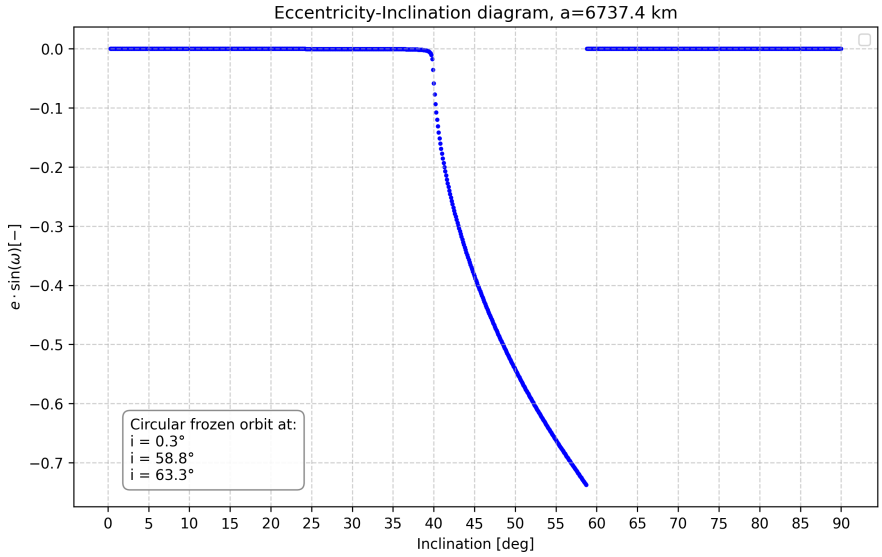


Figure 3.8: Frozen Orbits solutions space for altitude $h = 5000\,\text{km}$.

3.2 Stability Analysis

The purpose of the stability analysis is to verify if the orbits, starting from an initial set of orbital elements chosen from the database of the LFOs, are truly frozen and therefore the orbital elements are constant or oscillates stable around the equilibrium point. To verify the frozen stability of the orbit, it is necessary to show the following plots: the eccentricity vector phase-space, the argument of perilune time evolution, the eccentricity-inclination coupling and the stability of the perilune altitude. As mentioned in the previous chapter, the perilune stability is more related to the safety and survival of the satellite, but it is influenced by the frozen stability of the orbit so it is showed in this section.

Some examples of frozen stability are reported below: in Fig.3.9 it is shown a perfectly frozen orbit where the argument of periapsis librates slightly around the frozen condition, which is $\omega = 270$ deg in this case, indicating a highly-stable LFO; in Fig.3.10 we can see that choosing an inclination near the gap without solutions is a bad idea due to the inaccuracy of the frozen eccentricity found, and in fact the solution is unstable because the argument of periapsis circulates (it shows a linear drift) from the initial frozen $\omega = 90$ deg towards $\omega = 270$ deg, meaning that the non-linear solver found the frozen eccentricity in the wrong domain (positive instead of negative) and the unstable solution tends towards the argument of periapsis the provides stability; in the Fig.3.11 the argument of periapsis is highly unstable and it shows both behaviour of libration and circulation, with the amplitude of the

oscillations growing rapidly, a behaviour really common for low altitudes (typically below 500 km) where the lunar mascons highly perturbate the satellite dynamics.

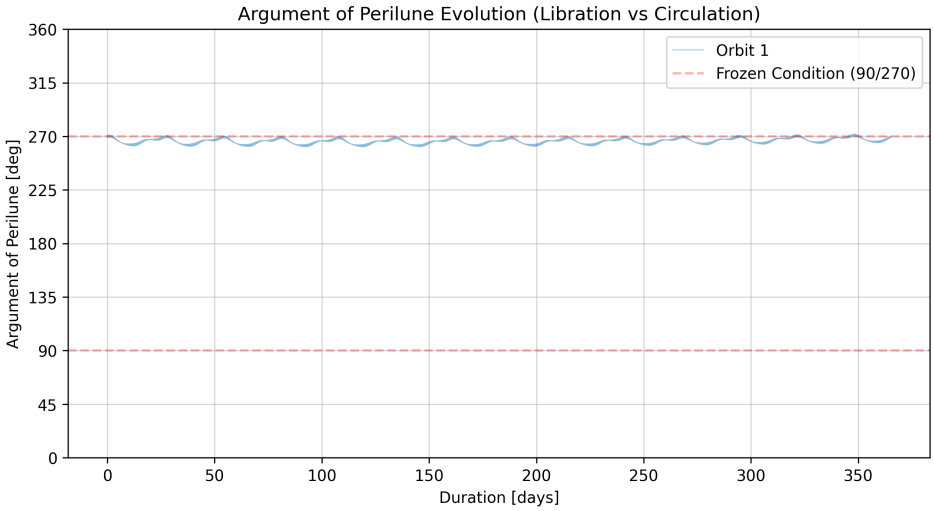


Figure 3.9: Evolution of the argument of Peri-apsis (ω) over 1-year, for a LFO with $h = 1000\,\text{km}$ and $i = 35$ deg.

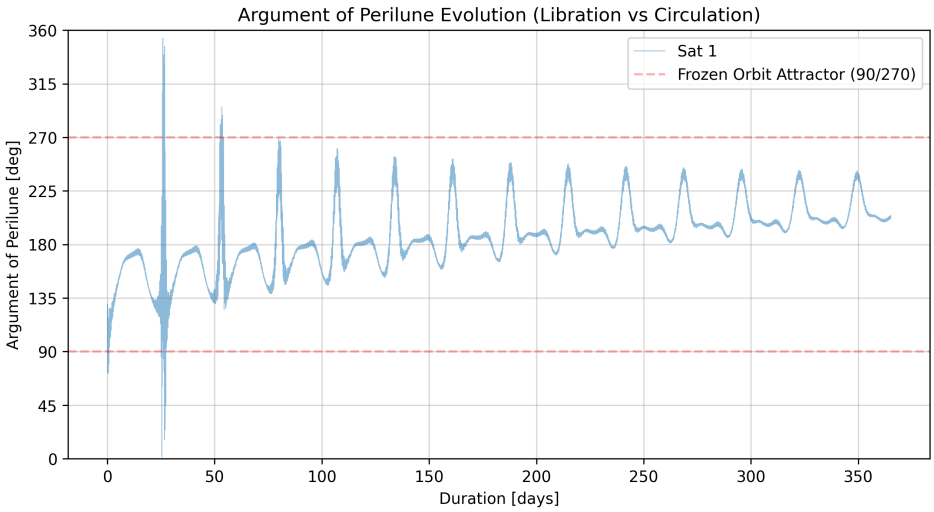


Figure 3.10: Evolution of the argument of Peri-apsis (ω) over 1-year, for a LFO with $h = 1000\,\text{km}$ and $i = 57.5$ deg.

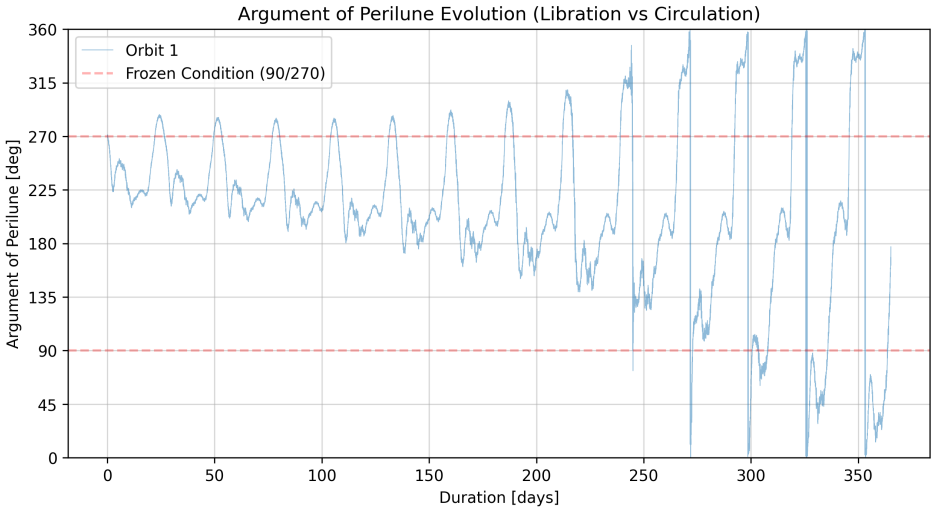


Figure 3.11: Evolution of the argument of Peri-apsis (ω) over 1-year, for a LFO with $h = 200\,\text{km}$ and $i = 85$ deg.

The frozen stability is also examined by the evolution of the eccentricity vector $(e\cos\omega, e\sin\omega)$ in the phase-space. For an orbit to be frozen and stable, the argument of periapsis and the mean eccentricity are constant or slightly oscillating around the equilibrium point in a bounded region due to the balance of the gravitational perturbations. In the phase-space, the eccentricity vector shall be bounded by a closed region around the starting eccentricity, identified by a green dot in the following figures. After 1-year propagation of the trajectory, it is possible to identify four possible behaviours of the eccentricity vector.

In Fig.3.12, some examples of the stability behaviour of the LFOs is reported. In the top-left image, an orbit with initial condition $h = 1000\,\text{km}$ and $i = 35°$ is initialized with the following frozen orbital elements: $e = 0.01068$, $\omega = 270$ deg. After 1-year trajectory propagation, the eccentricity vector is bounded in a small region around the target eccentricity and it evolves in tight loops around the target. This means the orbit's shape is consistent over time and that secular perturbations cancel out each other. In the top-right corner, an orbit with $h = 800\,\text{km}$ and $i = 79$ deg has initial orbital elements $e = 0.006165$ and $\omega = 270$ deg. The eccentricity vector is bounded in a closed region of the phase-space, wider than the orbit mentioned earlier, meaning that the orbit is quasi-frozen but relatively stable and it is possible to place a satellite in this trajectory without risking to lose the configuration. In the bottom-left corner, an orbit with $h = 1000\,\text{km}$ and $i = 57.5$ deg has the corresponding frozen elements $e = 0.000027$ and $\omega = 90$ deg. The eccentricity vector does not oscillate around a locked target, but it drifts away due to the perturbations. In this case the orbit is unstable and it means the preliminary

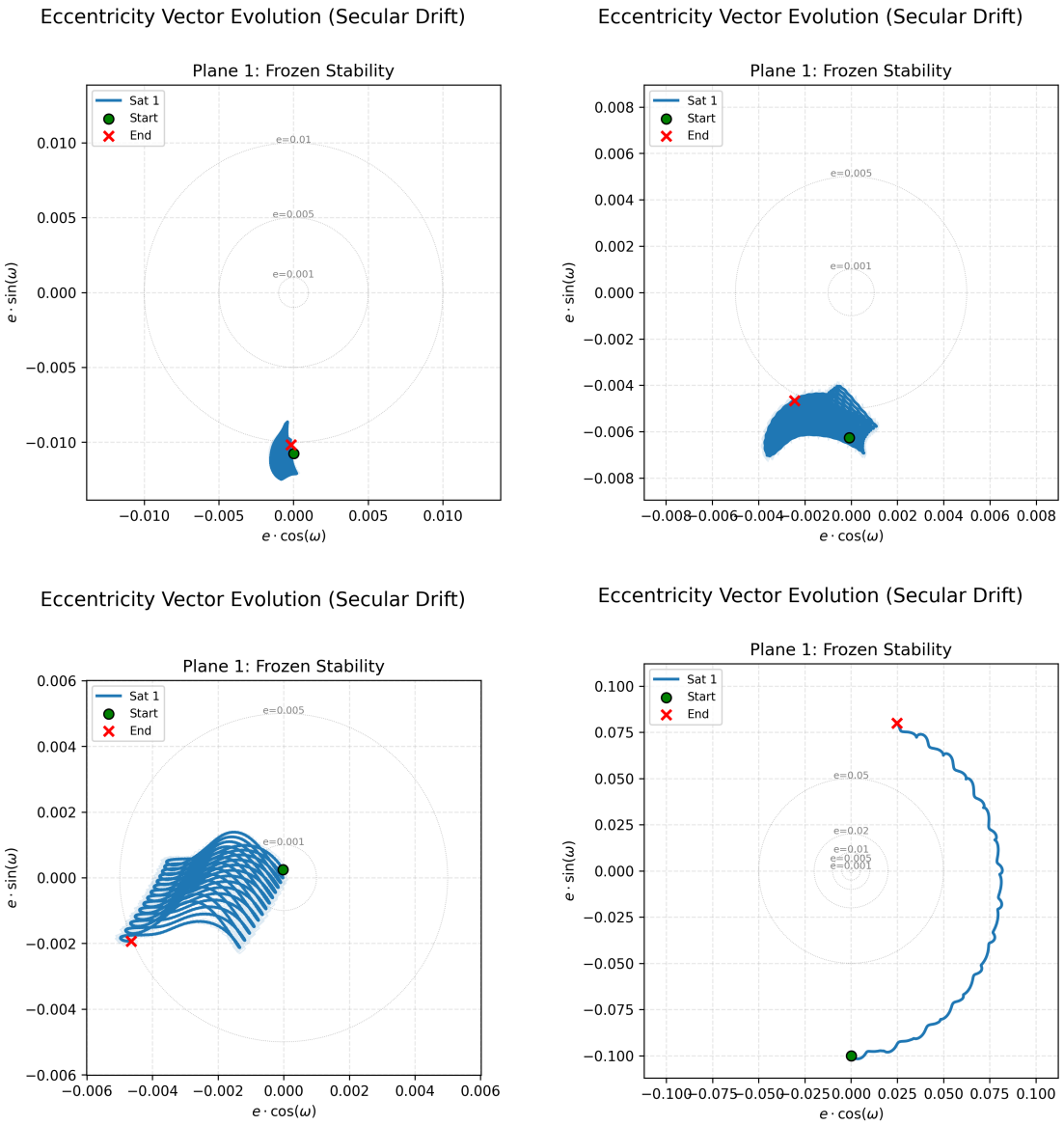


Figure 3.12: Eccentricity Vector Phase-Space Evolution for the following orbits: Top left: $h = 1000\,\text{km}$, $i = 35$ deg; Top right: $h = 800\,\text{km}$, $i = 79$ deg; Bottom left: $h = 1000\,\text{km}$, $i = 57.5$ deg; Bottom right: $h = 1000\,km$, $i = 34$ deg.

search of the LFO was unsuccessful in this case and the orbit shall be discarded for further analysis. The worst case is shown in the last example at the bottom-right figure, where the orbital elements are $h = 1000\,\text{km}$, $i = 34°$, $e = 0.009935$ and $\omega = 270$ deg. In this case the orbit is not even frozen because the argument of peri-apsis shows circulation, meaning that Alg.14 failed to find the correct combination of eccentricity and argument of peri-apsis for this particular inclination.

An unstable orbit causes the eccentricity to grow rapidly, leading to an increase in the difference between the radius of apo-apsis and the radius of peri-apsis. When the orbit is low, a sudden decrease in the periapsis altitude can lead to a crash on the lunar surface caused by the instability of the frozen condition. For this reason, it is important to discard from the analysis all the orbits where the perilune altitude decreases in time, or where the range between the maximum and the minimum altitude (which will be called perilune altitude breathing from now on) is too high. This problem appears especially for orbits with semi-major axis lower than $a < 2237\,\text{km}$, because the lunar gravity field is stronger and the pull towards the surface is much more irregular due to the mascons. In the figures below some examples of Perilune Altitude evolution are presented: in Fig.3.13 the mean value of the altitude remains approximately constant for 1 year, the breathing is visible but the range is limited with respect to the orbit's altitude; in Fig.3.14 the mean value of h_p decreases over time, but the breathing (defined as the amplitude of the oscillation between the maximum and the minimum) calms down after oscillating at the beginning of the propagation; in Fig.3.15 the mean value of h_p decreases linearly until eventually the orbit will crash on the surface, therefore the orbit should discarded in a PASS/FAIL selection of the suitable orbits for the lunar constellation.

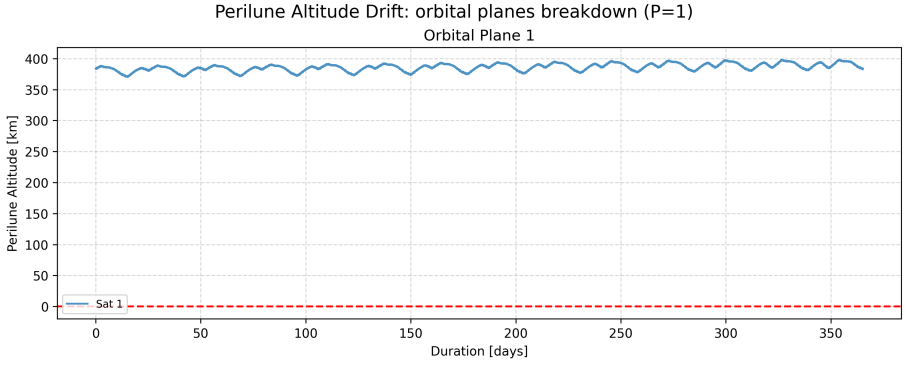


Figure 3.13: Orbital safety analysis: 1-year evolution of the Perilune Altitude (h_p). Initial orbital elements: $h = 400\,\text{km}$, $i = 76$ deg, $e = 0.007632$.

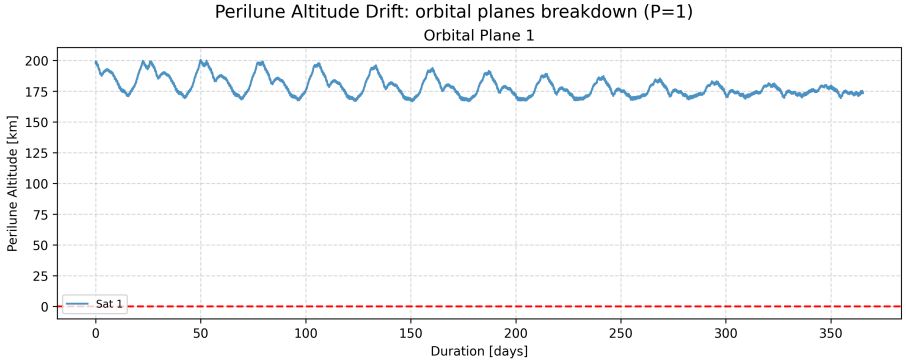


Figure 3.14: Orbital safety analysis: 1-year evolution of the Perilune Altitude (h_p). Initial orbital elements: $h = 200\,\text{km}$, $i = 82$ deg, $e = 0.000483$.

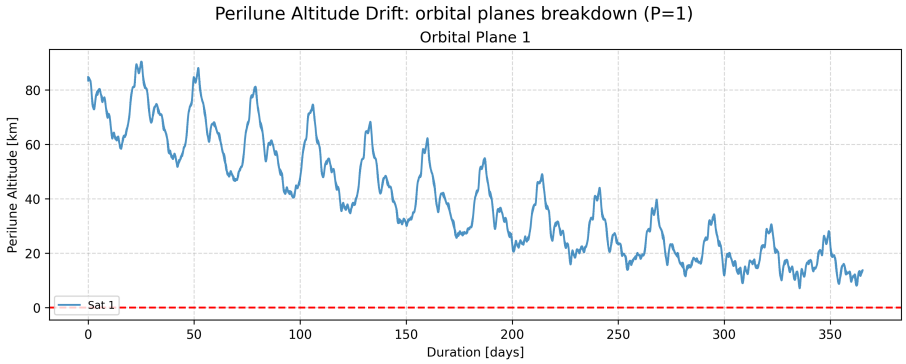


Figure 3.15: Orbital safety analysis: 1-year evolution of the Perilune Altitude (h_p). Initial orbital elements: $h = 100\,\text{km}$, $i = 82$ deg, $e = 0.008332$.

A statistical analysis is conducted to assess the feasibility of deploying a constellation in orbit around the Moon. A set of altitudes and inclinations is chosen to define a pool of candidate orbits, then each orbit is propagated for 1 year to verify the safety and the frozen stability and compared to the other candidates. The set of altitudes evaluated range from 100 km to 1000 km with step 100 km, to analyze the prevalence of the Lunar Gravity Field with respect to the Earth Third-Body Perturbation or vice-versa. The set of inclinations chosen ranges from 70 to 85 degrees with step 3 degrees, because to provide global coverage a constellation shall have higher inclination, up to near polar inclinations. In this way the gaps in the LFOs eccentricity-inclination diagram are avoided and a thinner inclination grid can be evaluated. Choosing this pool of elements, a total of 60 simulations is performed and later analyzed. For each combination of altitude and inclination, the eccentricity and the argument of peri-apsis are retrieved from the LFO database,

the RAAN and the Mean Anomaly are defaulted to 0 deg.

The first analysis in Fig3.16 shows that the orbits above 300 km of initial altitude are safe from degradation, a positive aspect about lunar orbits with respect to the Earth orbits which decay due to the atmospheric drag. The lunar orbits are less risky from this point of view because gravitational perturbations are symmetric and periodic and only orbits lower than 200 km are dangerous for possible impacts on the surface. The high orbits show a very stable behavior at perilune altitude, because the breathing (the range between $max(h_p)$ and $min(h_p)$) is only 1% of the reference altitude, while lower orbits have higher amplitude of oscillations, up to 20% of the reference altitude.

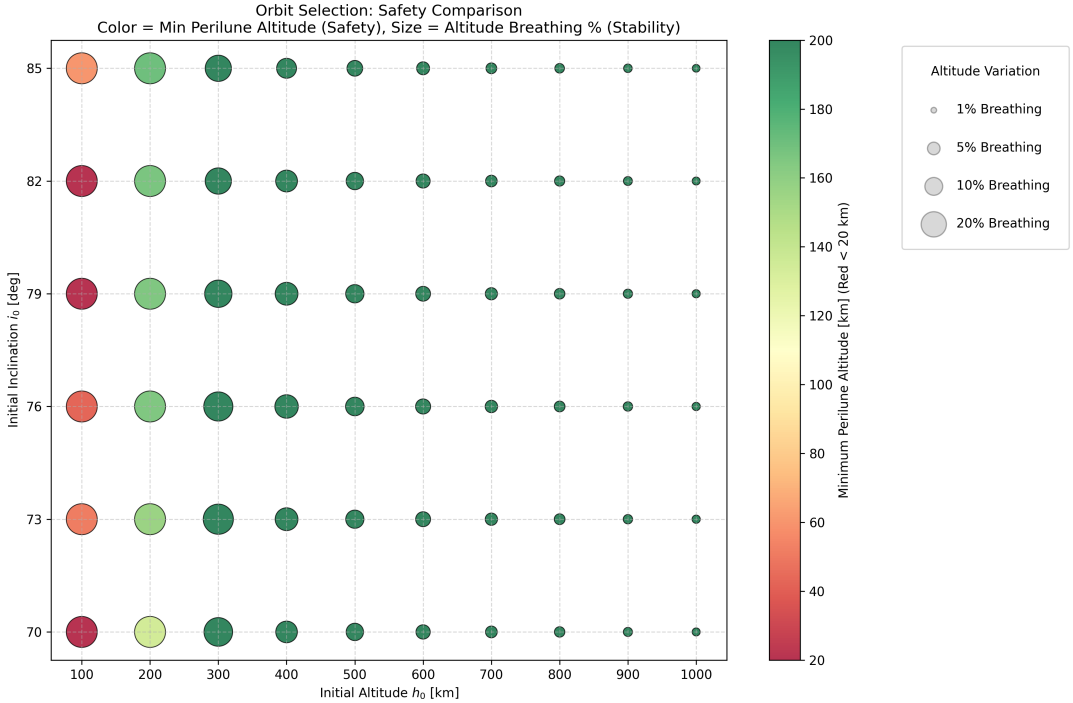


Figure 3.16: Perilune altitude (h_p) stability statistics: minimum perilune altitude and altitude breathing VS initial orbital elements (h, i).

The frozen stability is evaluated by comparing the amplitude of the oscillations of the Argument of Perilune around the frozen condition at $\omega = 90$ deg or $\omega = 270$ deg, the range $\Delta\omega$. The orbit is considered frozen if the amplitude does not exceed 90 deg, meaning maximum 45 deg from the frozen condition. Over 180 deg of amplitude, usually it means that the Argument of Perilune is not librating but rather circulating around the orbit, jumping from 0 to 360 degrees multiple times. The majority of the orbits above 500 km are frozen, while it is possible to identify

some frozen orbits also at lower altitudes, for example at $i = 79$ deg for $h = 100$ km or at $i = 70$ deg for $h = 200 - 300$ km. It is possible to affirm that the preliminary analysis for the search of LFOs is sufficient at higher altitudes, while it needs a better refinement in the correction of the initial orbital elements, especially considering algorithms to convert the mean orbital elements (defined by the double averaging theory) to the osculating orbital elements which take into account for the short-period perturbations.

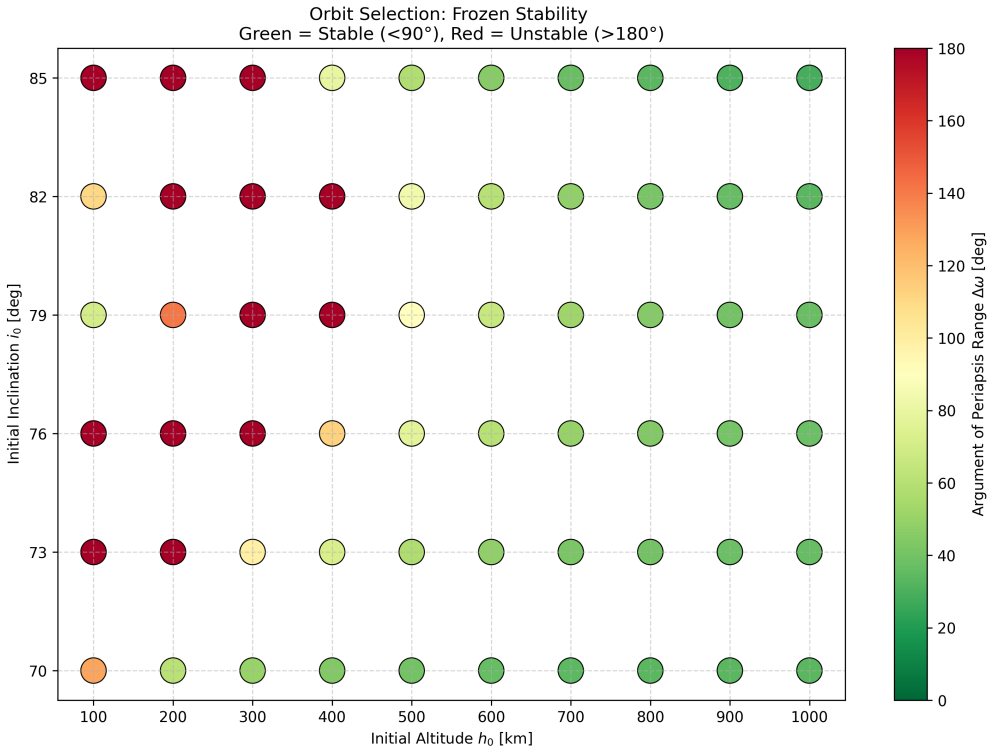


Figure 3.17: Frozen stability: amplitude of the oscillations of the argument of peri-apsis (ω) VS initial orbital elements (h, i).

The analysis of the frozen stability is further deepened by examining the dispersion of the eccentricity vector in the phase space. Fig.3.18 illustrates the mean and maximum dispersion of the eccentricity vector components $(e \cdot \cos\omega, e \cdot \sin\omega)$ as a function of the initial orbital elements (altitude and inclination). The dispersion is quantified as the Euclidean distance between the instantaneous eccentricity vector and the initial frozen vector, averaged over the propagation period (mean dispersion) or evaluated at its peak (max dispersion). The results highlight a clear correlation between altitude and stability: for orbits below 200 km, the dispersion values are significantly larger, often exceeding 10^{-2} in magnitude, which corresponds to

the wide, irregular loops observed in the phase space diagrams. Conversely, for altitudes above 500 km, the dispersion drops by an order of magnitude, indicating tightly bounded oscillations and a robust frozen condition. Furthermore, a spike in dispersion is evident around the critical inclination region ($i \approx 57$ deg), where the resonant effects destabilize the orbit and, as shown by previous Figures, leading to circulation rather than libration of the argument of perilune.

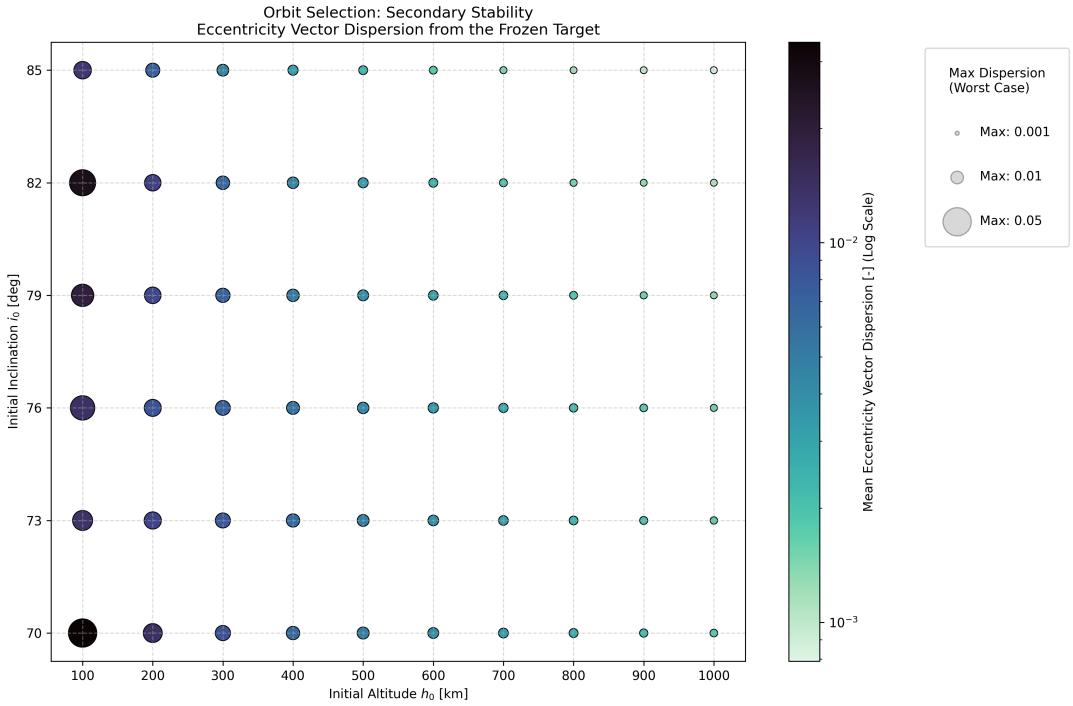


Figure 3.18: Secondary frozen stability: Mean and Max dispersion of the eccentricity vector $(e\cos\omega, e\sin\omega)$ VS initial orbital elements (h, i).

The stability analysis conducted on the pool of 60 candidate orbits demonstrates that the adaptation of Earth-like constellation patterns to the lunar environment is feasible, provided that specific orbital regimes are selected. The results indicate that orbits with an altitude $h > 300$ km generally exhibit safe behavior with minimal degradation, making them suitable candidates for long-term constellation deployment without excessive station-keeping. Low Lunar Orbits ($h < 200$ km) are highly sensitive to the lunar mass concentrations (mascons), resulting in rapid perilune decay and high eccentricity dispersion. Similarly, inclinations near 57 deg should be avoided due to the solutions gap where stable frozen conditions cannot be maintained. The numerical propagation confirms that while the analytical double-averaging theory provides a good initial guess for frozen orbits, the actual stability is strongly dependent on the full perturbation model. Orbits that maintain

a low eccentricity dispersion and a librating argument of perilune are verified as true Lunar Frozen Orbits, suitable for the constellation design. These findings allow us to filter the initial design space, discarding unstable candidates and focusing the subsequent constellation performance analysis on the robust orbital sets identified.

3.3 Semi-Major Axis Correction Map

The stability analysis assumed to initialize the orbital elements of the satellites always with default RAAN and initial Mean Anomaly, to properly assess the dependancy between the stability properties and only the initial semi-major axis and inclination. As the analysis goes further, the first results of the constellations' propagation reveals a discrepancy between osculating semi-major axis at which all satellites of the constellation are initialized (a_0) and the mean semi-major around which the evolution of the orbital element oscillates around. For example, in the Fig.3.19, a constellation made of 3 satellites whose initial osculating orbital elements are reported in Table 3.1:

a_0 [km]	e_0	i_0 [deg]	Ω_0 [deg]	ω_0 [deg]	M_0 [deg]
2737.4	0.004556	85	0	270	[0,120,240]

Table 3.1: Initial osculating orbital elements for a constellation Walker Delta 85: 3/1/0.

After 1-year propagation of the trajectory, the semi-major axis of each satellite oscillates around a different mean value of a, which means that short period perturbations act by sorting the satellites in different levels of mechanical energy. Basically, the orbital elements of the LFOs found in the previous section are referred as **mean orbital elements**, while the propagator requires to initialize the trajectory with **osculating orbital elements**. The main setback of the wrong initialization of the orbital elements is that even a discrepancy of 300 meters in a_{mean} can result in a in-plane dephasing of the constellation, with the relative mean anomaly between adjacent satellites to drift away from the initial value of Fig.3.20. To account for the short period perturbations and initialize all the satellites on the same energety value, a process to convert the mean orbital elements into osculating orbital elements is necessary. Since this process requires the use of Hamiltonian perturbation, it is not the purpose of this thesis. The amplitude of the oscillations, instead, is bounded to ± 0.5 km and is acceptable for the station-keeping limitations.

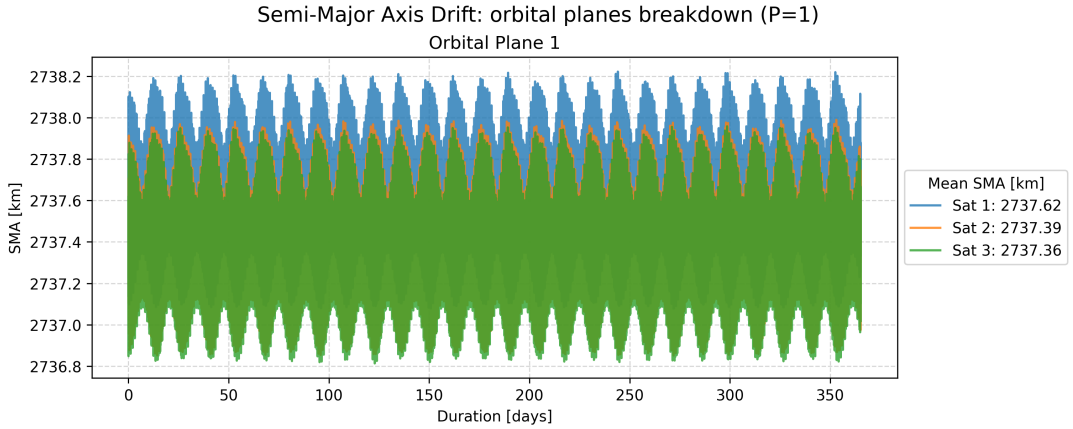


Figure 3.19: Semi-Major Axis 1-year evolution for a constellation with 3 satellites in 1 plane, deployed at $M_0 = [0,120,240]$ deg. Initial osculating orbital elements: $h = 1000$ km, $i = 85$ deg.

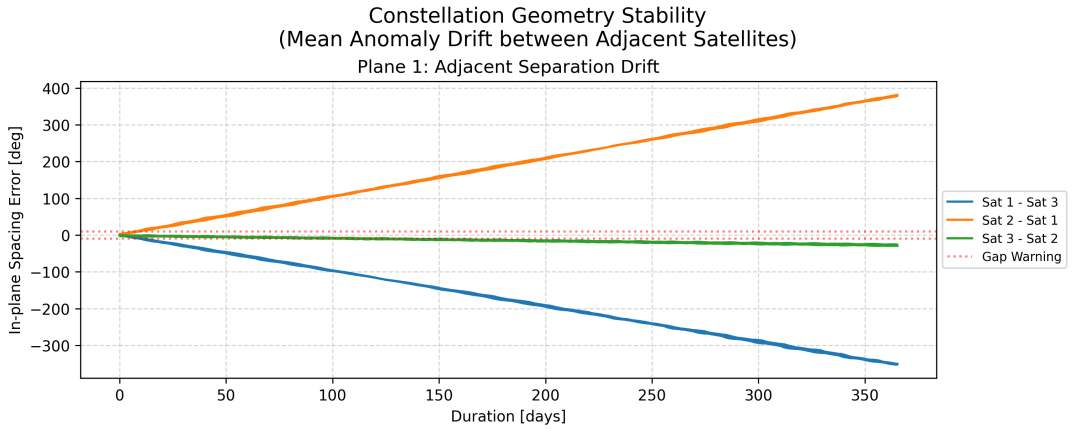


Figure 3.20: Relative Mean Anomaly Drift for a constellation with 3 satellites in 1 plane, deployed at $M_0 = [0,120,240]$ deg. Initial orbital elements: $h = 1000$ km, $i = 85$ deg.

It is of uttermost importance to verify the correlation between the mean semi-major axis (SMA) deviation and the initial conditions of the propagator. Initially, two grid heatmaps are created: in Fig.3.21 the difference between a_{mean} and a_0 is correlated to the couple (h_0, Ω_0), in Fig.3.22 the mean sma deviation is correlated to the couple (h_0, M_0), the inclination is kept constant for this analysis, while e and ω for each couple of orbital elements is retrieved from the LFO database. For the first analysis, the default mean anomaly is $M_0 = 0$ deg, while for the second $\Omega_0 = 0$ deg. Every orbit is propagated for 1-year and then in the post-processing

the mean sma is calculated, the deviation $a_{mean} - a_0$ is computed and the value is reported in the grid with a colorbar, with blue meaning a positive difference and red a negative difference.

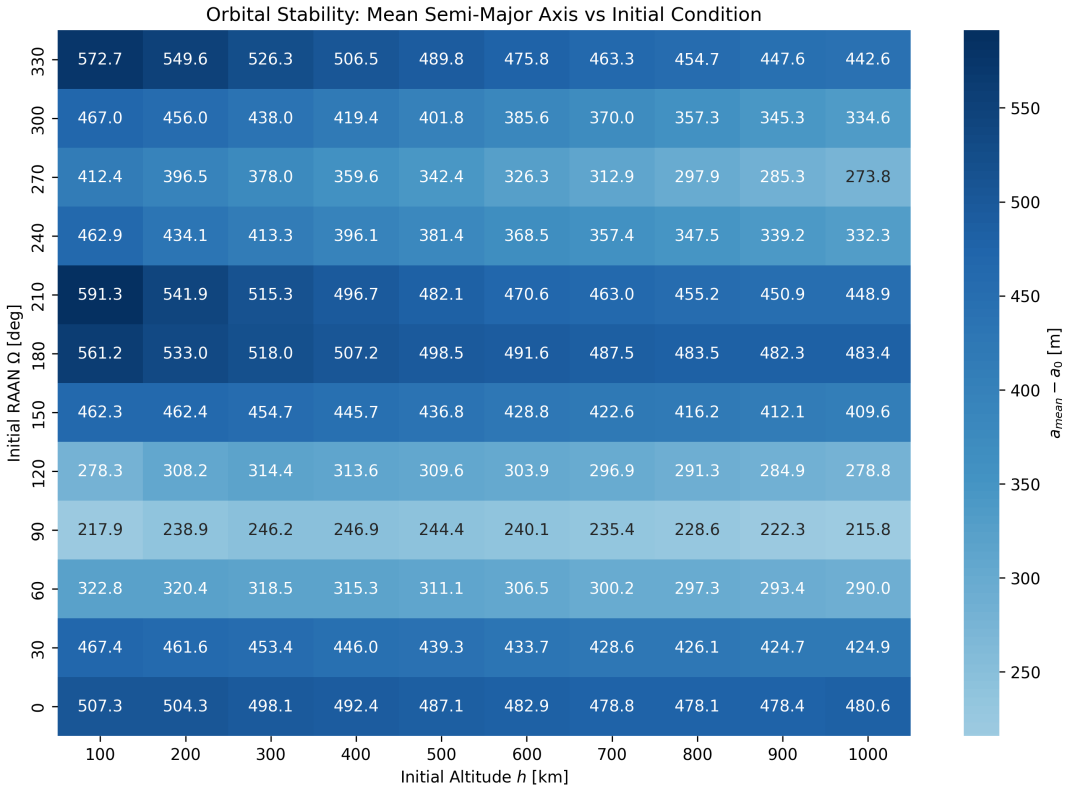


Figure 3.21: Mean Semi-major axis VS initial orbital elements (h, Ω).

The first result shows that, regardless of the initial RAAN, the satellites will always oscillate around a larger value of mean sma. We observe that there is a linear correlation between the altitude and the mean sma deviation for every fixed RAAN, meaning that this phenomenon is purely driven by the intensity of the Lunar Gravity Field rather than Earth's perturbation. Hence, the lower the altitude, the stronger the deviation of the mean sma from the initial osculating value. Another important observation is the presence of bands with larger deviation, corresponding to the counter-facing points at $\Omega_0 = 0$ deg and $\Omega_0 = 180$ deg. The reason is due to the definition of the reference frame PALRF in which the orbital elements are defined: the x-axis lies on the orbital plane and defines the prime meridian of the Moon, is also the principal axis of bigger inertia of the Moon, the longitude where the majority of the mass of the planet is distributed and therefore the gravity field is stronger. The RAAN is measured on the equatorial plane, from

the prime meridian, and therefore the mean sma deviation is stronger at these longitudes.

Since all the deviations are positive we wish to understand if other elements are contributing more to the deviation of the sma. The second heatmap grid is helpful to visualize the contribution of the initial Mean Anomaly to the mean sma deviation. Keeping the RAAN fixed at the prime meridian, another set of orbits is propagated for 1 year to study the dependancy on M_0, revealing a wave pattern if we look at each column with fixed altitude.

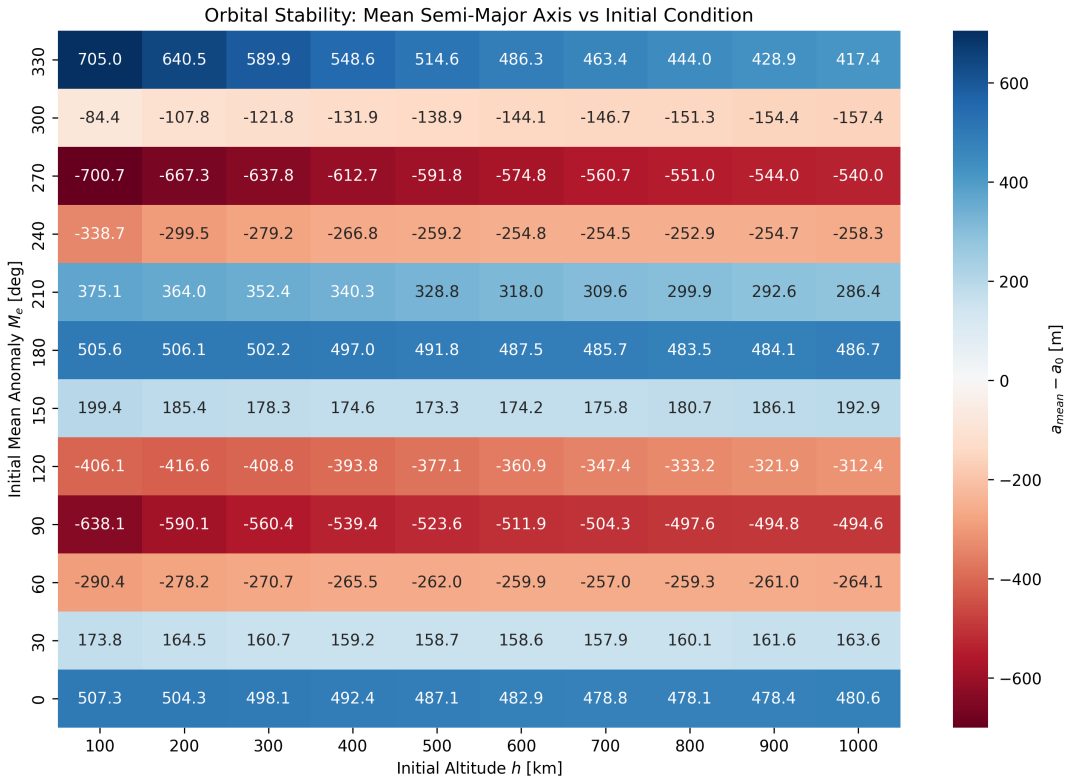


Figure 3.22: Mean Semi-major axis VS initial osculating orbital elements (h, M_e).

If the satellite is deployed with $M_0 = 90$ deg or $M_0 = 270$ deg, the mean sma will stabilize around 500-700 meters lower than the initial sma, depending on the distance from the surface. The reason is due to the theory of frozen orbits, which enforces the argument of periapsis to be only $\omega = \pm 90$ deg in corrispondence of the north or south pole of the Moon, meaning that a satellite deployed with $M_0 = \pm 90$ deg will be aligned with the equatorial plane, where the gravitational pull towards the surface is stronger and the energetic level due to the short period perturbation will be lower. The effect is visible up to a range of Mean Anomaly up to ± 30 deg

angular distance from the equator, creating a band of initial Mean Anomaly that causes a decrease in the value of a_{mean}, while all other values of M_0 experience an increase in the value of a_{mean}.

To verify the combined contribution of M_0 and Ω_0 on the deviation of the mean sma from the initial osculating sma, a Semi-Major Axis Correction Map is created: for a fixed altitude an inclination a pool of 576 possible combinations is propagated for a total of 20 orbits, considered enough revolutions to define a valid value for a_{mean} which can be mantained for a longer propagation period. For each combination of (M_0,Ω_0), the mean sma deviation defined as ($a_{mean} - a_0$) is reported on a heatmap contour plot, where the colorbar is bounded between the minimum (negative) and the maximum (positive) sma deviation.

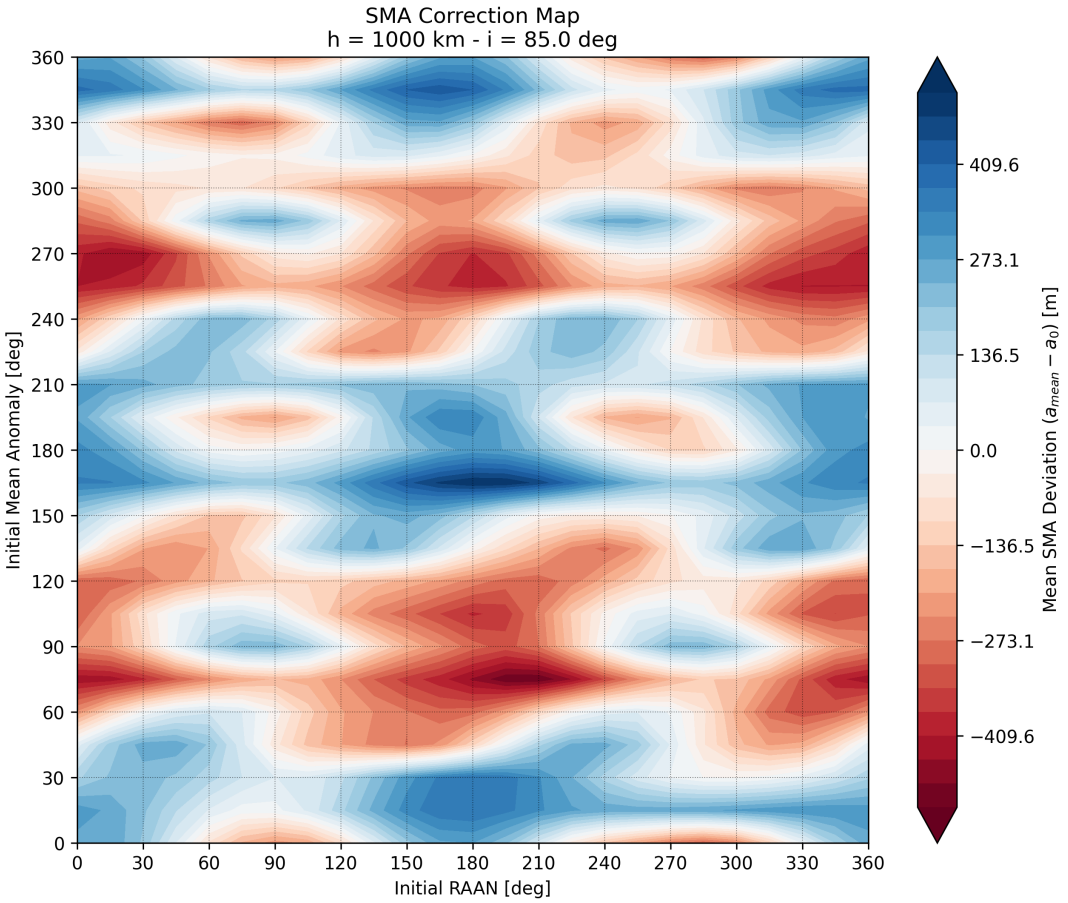


Figure 3.23: Semi-major Axis correction map: a_{mean} deviation correlated to initial RAAN (Ω) and Mean Anomaly (M_e). Initial osculating orbital elements: $h = 1000$, $i = 85$ deg.

In the Fig.3.23, an example of SMA Correction Map is reported for the fixed values of $h = 1000$ km and $i = 85$ deg. The colours are set in order to have always $a_{mean} - a_0 = 0\,[m]$ in the middle of the colorbar in white, while the colour in between a square of the sampled points grid is generated with a linear interpolation approximation. The pattern revaled is patchy, because the negative peak experienced at $\Omega_0 = 0$ deg and $\Omega_0 = 180$ deg mitigates the positive peak for $M_0 = 90$ deg and $M_0 = 270$ deg, creating some countour lines where the two effects balance each other giving a nil deviation, and some contour islands with peak positive or negative deviation.

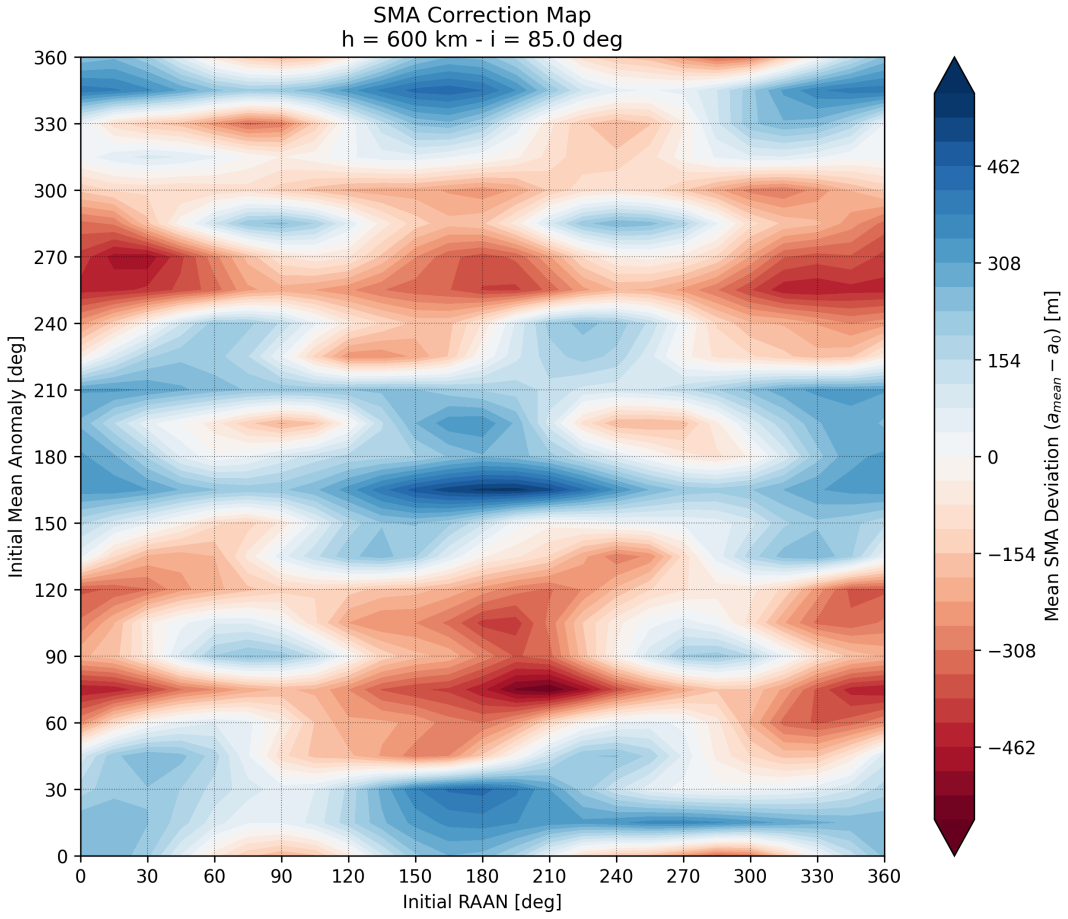


Figure 3.24: Semi-major Axis correction map: a_{mean} deviation correlated to initial RAAN (Ω) and Mean Anomaly (M_e). Initial osculating orbital elements: $h = 600$, $i = 85$ deg.

To verify if the pattern is confirmed for different altitudes or inclinations, other maps are created with the same logic. In Fig.3.24, the SMA Correction Map of the

orbit with $h = 600$ km and $i = 85$ deg is reported: the pattern is unchanged with respect to a higher altitude with the same inclination. The only difference lies in the absolute maximum peak value, confirming that the perturbations are higher at lower altitudes.

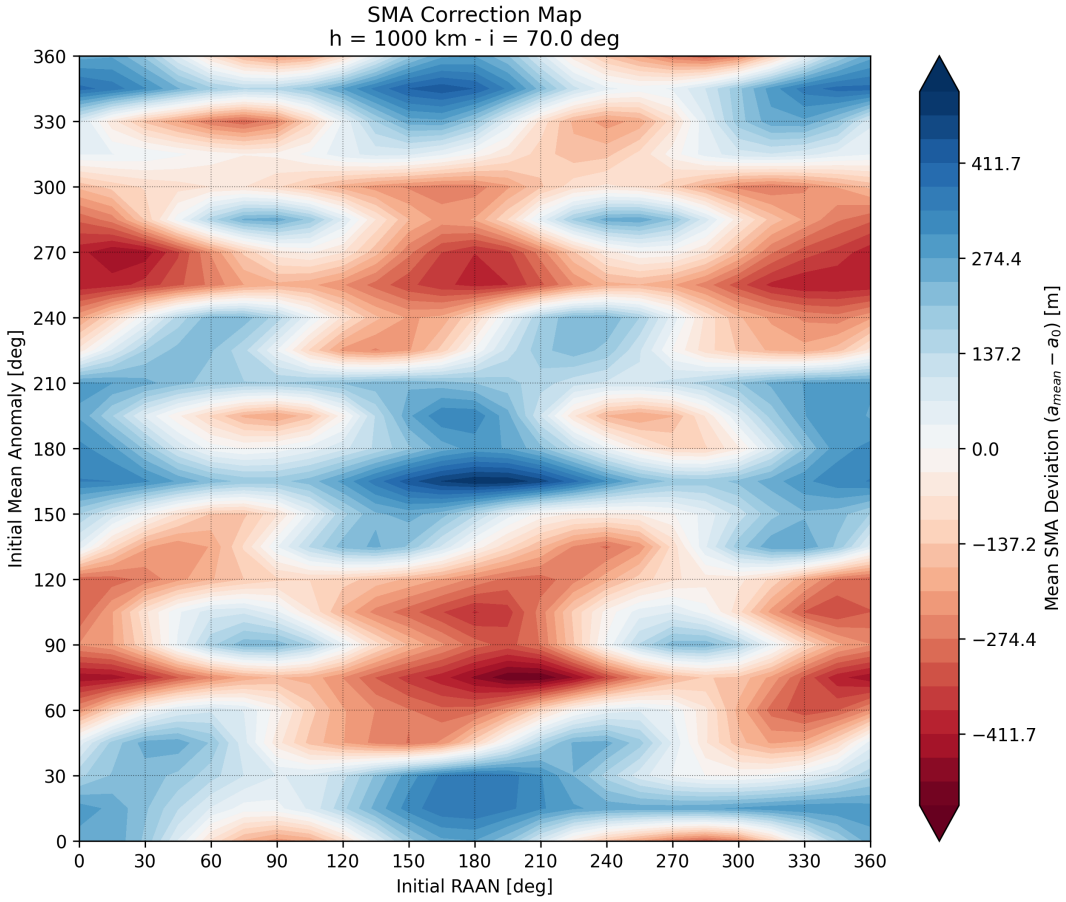


Figure 3.25: Semi-major Axis correction map: a_{mean} deviation correlated to initial RAAN (Ω) and Mean Anomaly (M_e). Initial osculating orbital elements: $h = 1000$, $i = 70$ deg.

In Fig.3.25, the SMA Correction Map for the orbit with $h = 1000$ km and $i = 85$ deg is reported: the pattern is again unchanged and even the peak values that are the colorbar limit have the same order of magnitude. It is possible to state that the SMA Correction Map has a fixed pattern depending only on the osculating RAAN and Mean Anomaly of the initial condition, while inclination does not affect at all the map, the distance from the surface influences the intensity of the deviation.

In the Figures below, other examples of SMA Correction Map are shown to strenghten the validity of the aforementioned conclusions of the analysis. The maps are created for the following couples (h, i): (300 km, 85 deg) shown by Fig.3.26; (600 km, 70 deg) shown in Fig.3.27; (300 km, 70 deg) shown in Fig.3.28.

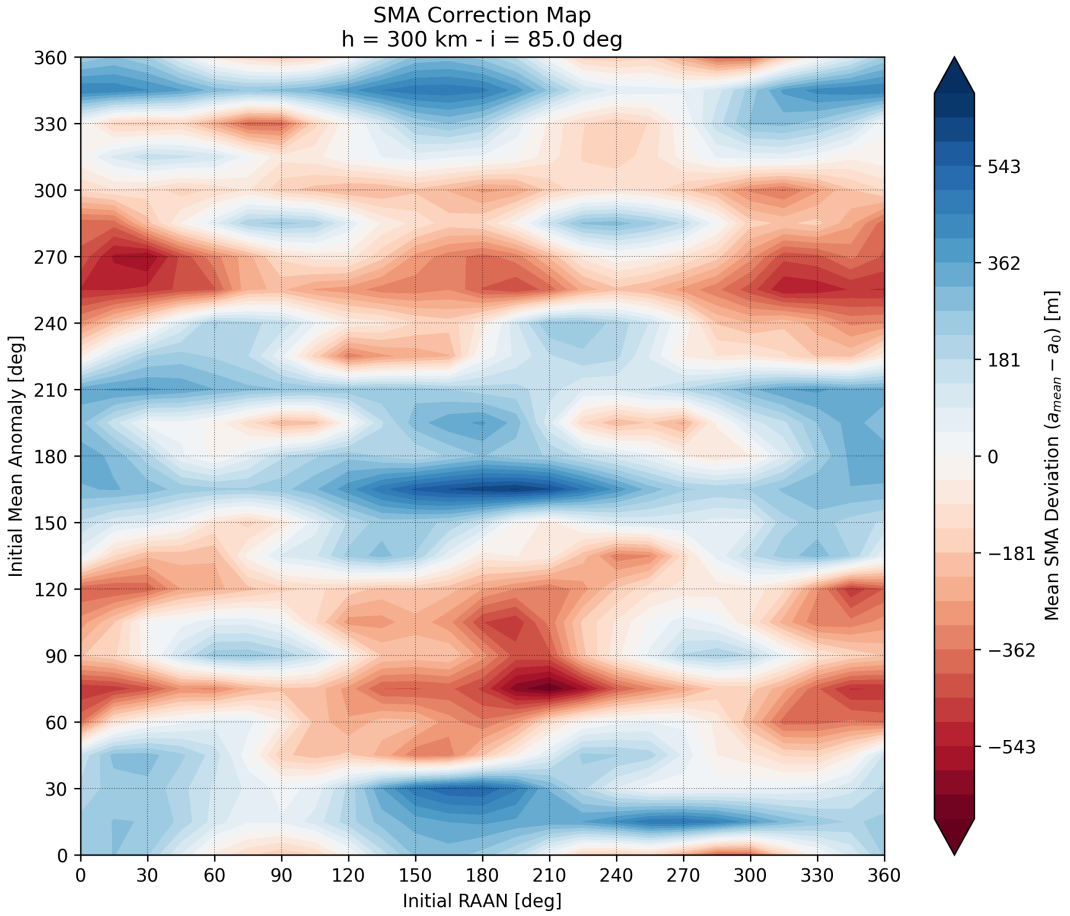


Figure 3.26: Semi-major Axis correction map: a_{mean} deviation correlated to initial RAAN (Ω) and Mean Anomaly (M_e). Initial osculating orbital elements: $h = 300$, $i = 85$ deg.

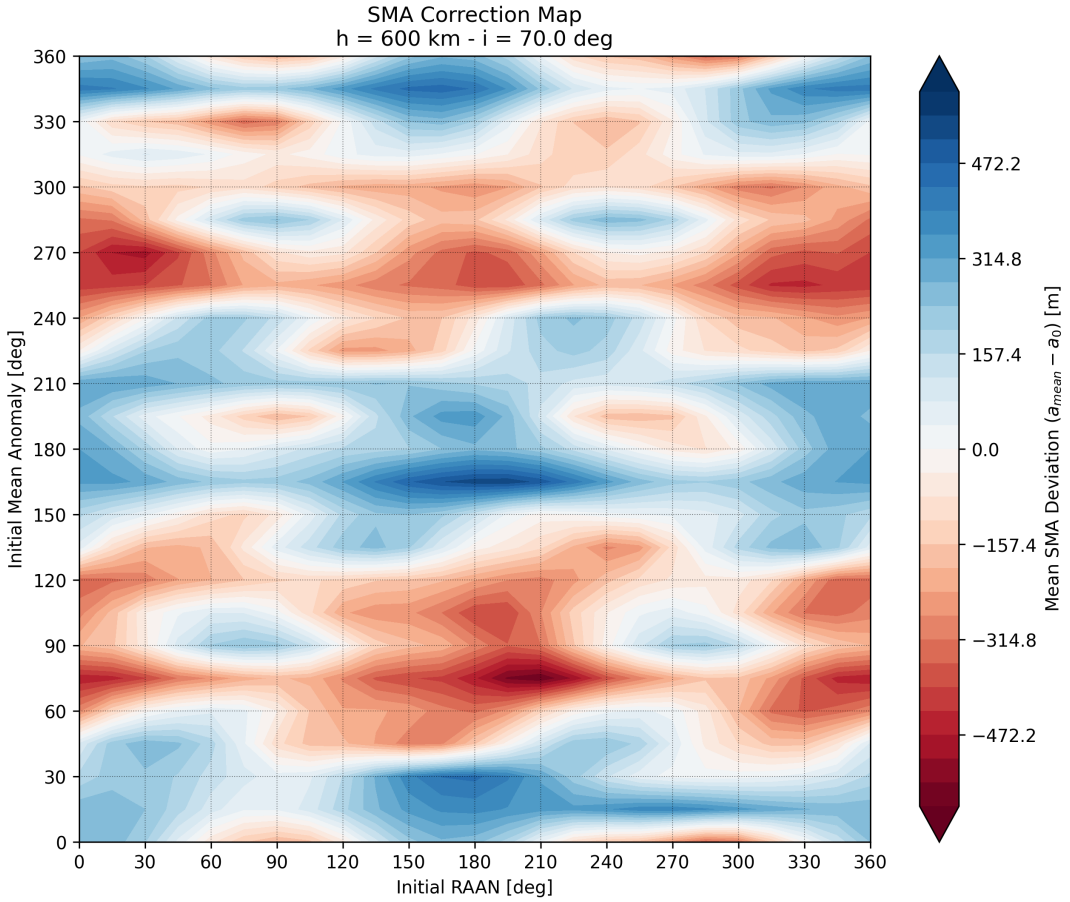


Figure 3.27: Semi-major Axis correction map: a_{mean} deviation correlated to initial RAAN (Ω) and Mean Anomaly (M_e). Initial osculating orbital elements: $h = 600$, $i = 70$ deg.

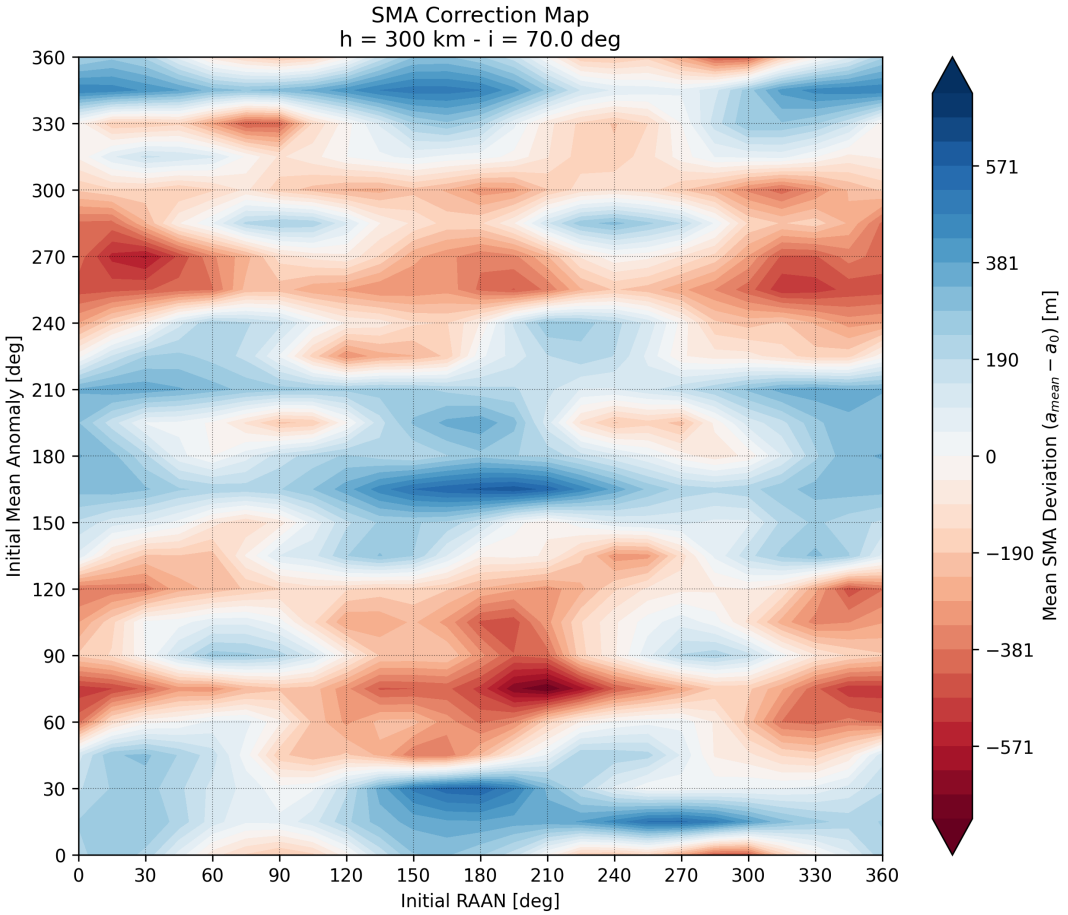


Figure 3.28: Semi-major Axis correction map: a_{mean} deviation correlated to initial RAAN (Ω) and Mean Anomaly (M_e). Initial osculating orbital elements: $h = 300$, $i = 70$ deg.

3.4 Inclination Correction Map

Another step of the analysis of the dynamics of Lunar Satellite Constellations regarded the relative drift of the inclination between planes initialized at different RAANs, and it is experienced that some orbital planes lose the desired geometry faster than others. The inclination oscillates around a mean value with a certain amplitude, the period of the oscillations being equal to the duration of the Lunar Month $T_{\leftmoon}$ defined in Table 1.3. In Fig.3.29, the inclination evolution of a Walker Delta constellation with 3 satellites in 3 different orbital planes is shown, with the initial osculating orbital elements as in Table 3.2.

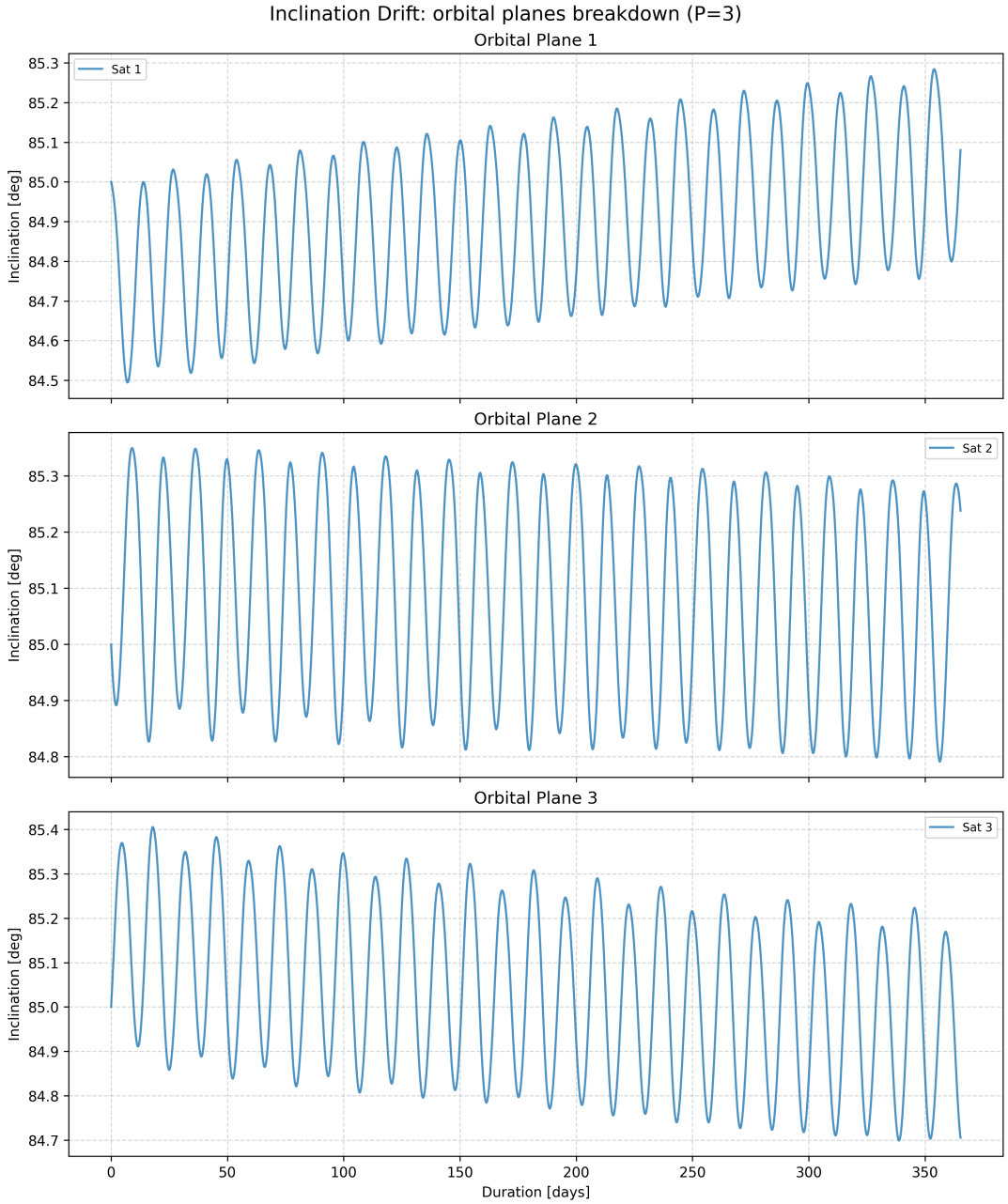


Figure 3.29: Inclination drift 1-year evolution for a constellation with 3 orbital planes at $\Omega_0 = [0,120,240]$ deg. Initial osculating orbital elements: $h = 1000$ km, $i = 85$ deg.

It is significant to specify that the amplitude of the oscillation is bounded within a range of ± 0.5 deg, and therefore it is not necessary to control it for the

a_0 [km]	e_0	i_0 [deg]	Ω_0 [deg]	ω_0 [deg]	M_0 [deg]
2737.4	0.004556	85	[0,120,240]	270	0

Table 3.2: Initial osculating orbital elements for a constellation Walker Delta 85: 3/3/0.

station-keeping. Furthermore, the period of the oscillation is as expected equal to $T_{\text{☾}}$, suggesting that this phenomenon is driven by the relative position of the Moon with respect to the Earth and therefore it is a third-body perturbation that causes this problem. It is desirable for a constellation to keep the inclination drift as close as possible to zero for several reasons: first, the coverage capabilities will be lost and the capability of the constellation to accomplish the mission goal, yielding to higher station-keeping cost; furthermore, the stability mechanism of the Kozai-Lidov coupling between eccentricity and inclination, described by Eq.(2.4), can be a source of instability if the eccentricity is perturbed enough to lose the frozen condition. An example of Kozai-Lidov coupling is shown in Fig.3.30 for a constellation with orbital elements as in Table 3.3.

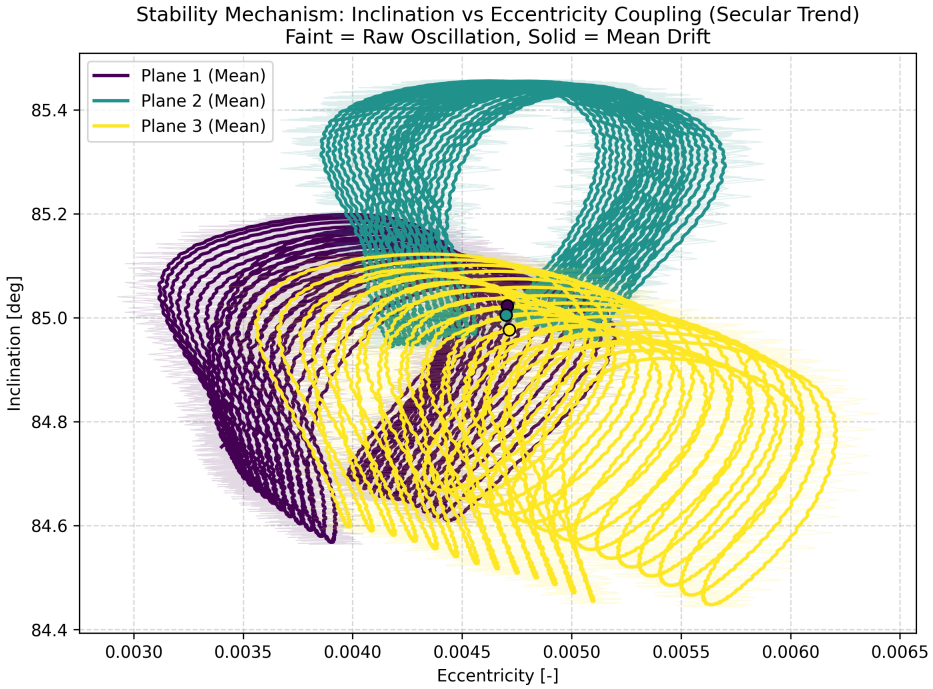


Figure 3.30: Kozai-Lidov coupling between eccentricity and inclination. Walker Star constellation pattern: 85:3/3/0.

a_0 [km]	e_0	i_0 [deg]	Ω_0 [deg]	ω_0 [deg]	M_0 [deg]
2737.4	0.004556	85	[45,90,135]	270	0

Table 3.3: Initial osculating orbital elements for a constellation Walker Delta 85: 3/3/0.

The third-body perturbation creates an energy exchange in the form of eccentricity increase at the expense of a loss of inclination, or vice-versa. If the first possibility is verified, the increase in eccentricity can cause the altitude of peri-apsis to decrease, pulling the satellite in a region where the gravitational field is stronger and starting a resonant phenomenon. In the example presented, the orbital plane at $\Omega_0 = 135$ deg is the most critical (the yellow curve shifts to the bottom-right corner of the plot) and it gives limitation on the station-keeping ΔV budget.

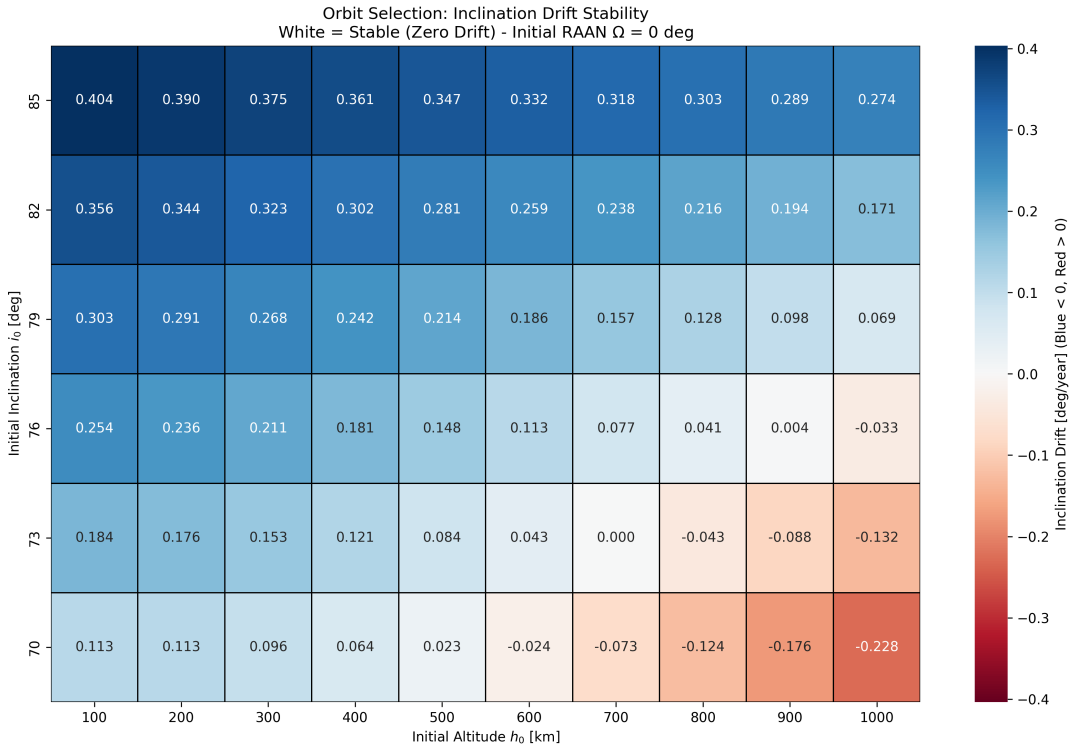


Figure 3.31: Inclination drift linear regression VS initial osculating orbital elements (h_0, i_0).

The analysis of the inclination drift linear regression is conducted for the same pool of orbits chosen for the semi-major axis correction map, revealing a correlation

between the set of initial osculating orbital elements (h_0, i_0) and the inclination drift $(\frac{di}{dt})$, as shown by Fig.3.31. For every combination of altitude and inclination, the trajectory of the satellite is propagated for 1 year, then in the post-processing a linear regression model is applied to the inclination time-series vector and the slope is plotted in a grid heatmap with the colorbar indicating the intensity of the drift slope. It is possible to identify a linear trend between the inclination at which the drift is nil: for $i_0 = 70$ deg, the slope is nullified for an altitude between $500 - 600$ km; for $i_0 = 73$ deg, the mean inclination is constant at an altitude of 700 km; for $i_0 = 76$ deg, the balancing altitude is between $900 - 1000$ km etc. Looking at the same row, and considering the altitude at which the inclination drift is balanced, the drift becomes negative (red) for higher altitudes and positive (blue) for lower altitudes. The analysis has been conducted by initializing the satellites at the same RAAN $\Omega_0 = 0$ deg and the same Mean Anomaly $M_0 = 0$ deg.

To verify if the initial osculating RAAN and Mean Anomaly have a sort of correlation with the inclination drift, the Inclination Drift Correction Map is created using the same logic of the SMA correction map. First, by verifiying the inclination evolution for a Walker Delta constellation defined by 85:12/1/0 at $h_0 = 300$ km, it was possible to eliminate the Mean Anomaly dependancy from the analysis, because as depicted in Fig.3.32 the 12 satellites evenly spaced in the same orbital plane will follow the same inclination evolution.

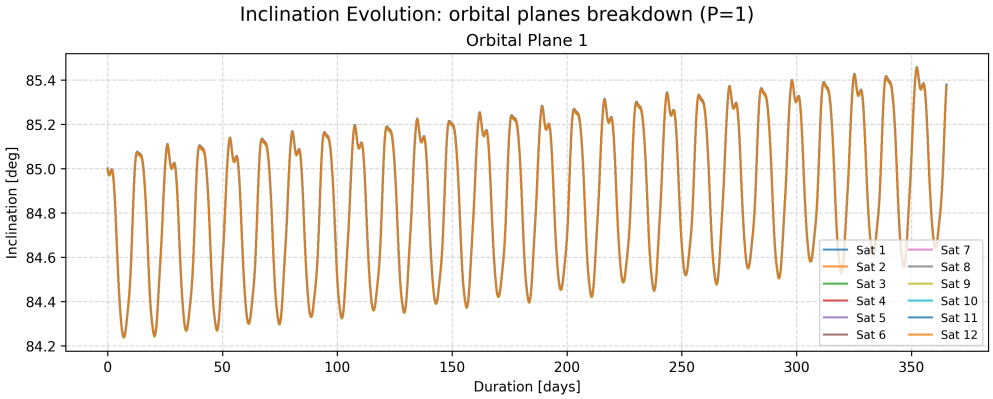


Figure 3.32: Inclination drift 1-year evolution for a constellation Walker Delta 85:12/1/0, initialized at $h_0 = 300$ km.

The Inclination Drift Correction Map is created by fixing the altitude at which the simulation is ran, then a set of 192 candidates is propagated for around 60 days, considered enough to include at least two periodic perturbation cycles. For each candidate, the linear regression model is applied to find the slope of the inclination drift curve, and then the value is visualized with a countour heatmap where the

colorbar represents the intensity of the drift (red for negative drift, white for nil drift, blue for positive drift), while the colour inside the sampled points grid is again linearly interpolated. In Fig.3.33, the Inclination Drift Correction Map is visualized for $h = 1000$ km: the pattern revealed is a sine wave, with negative drifts (the most dangerous for the Kozai-Lidov coupling) settled at $\Omega_0 = 0$ deg for lower inclinations, up to $\Omega_0 = 180$ deg for near-polar inclinations, up to $\Omega_0 = 270$ deg at again lower inclinations.

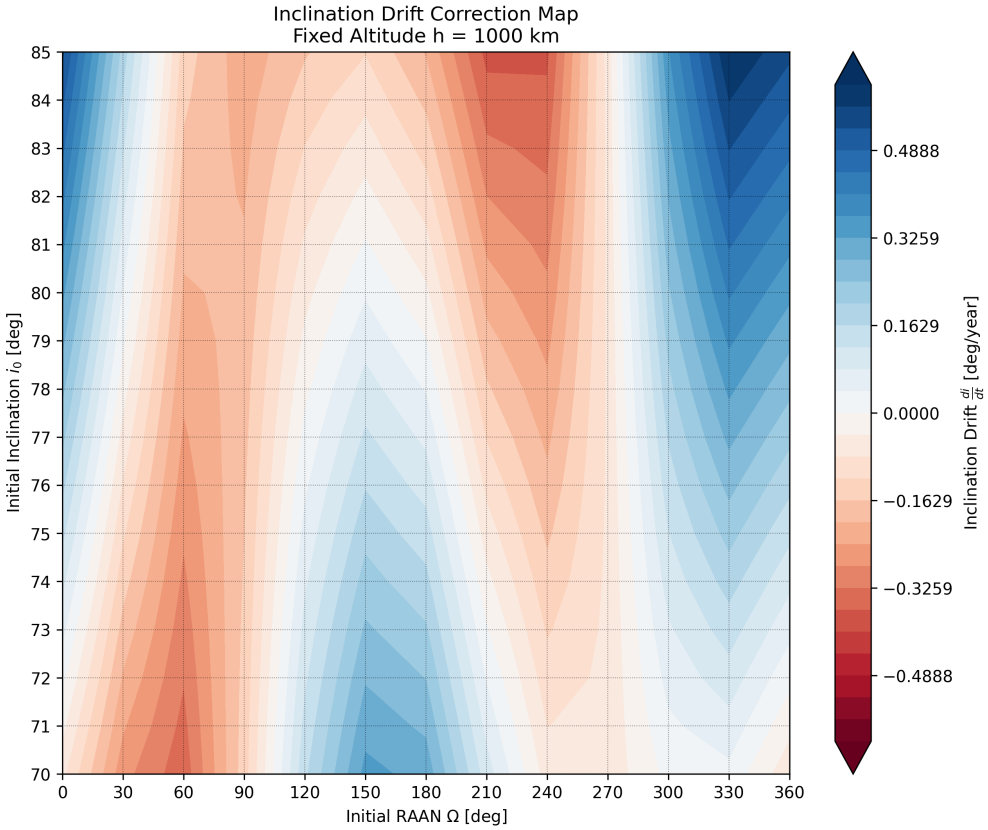


Figure 3.33: Inclination Drift correction map: $\frac{di}{dt}$ linear regression correlated to initial RAAN (Ω) and Inclination (i_0). Initial osculating orbital elements: $h = 1000\,\text{km}$.

The same process is applied to all the altitudes of interest for this thesis: the pattern of the map in Fig.3.34, generated for $h = 800$ km, is again a sine wave but the peak of the positive drift (blue) is higher at RAANs of $\Omega = 330$ deg $- 360$ deg, probably meaning that the distance from the surface and therefore the gravity field plays also a role in this perturbation.

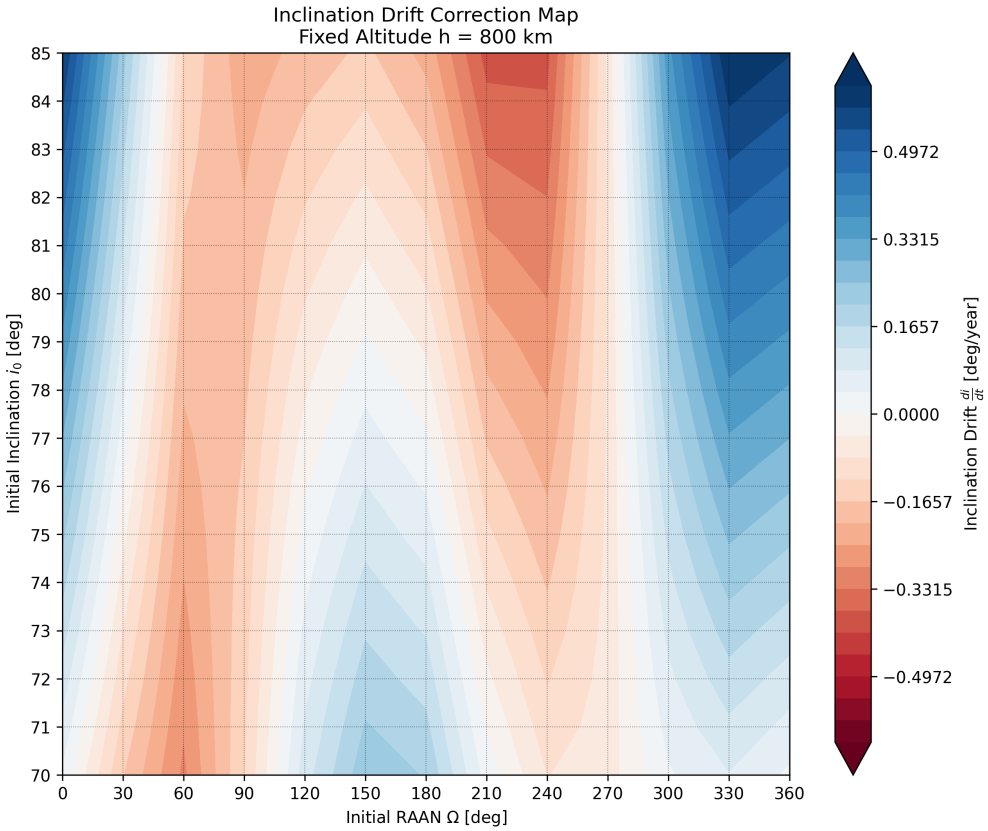


Figure 3.34: Inclination Drift correction map: $\frac{di}{dt}$ linear regression correlated to initial RAAN (Ω) and Inclination (i_0). Initial osculating orbital elements: $h = 800\,\text{km}$.

Going further with the analysis, lower altitudes like $h = 600$ km start revealing a different pattern shape, but it is important to keep in mind that the inclinations interval is bounded between 70 to 85 degrees. In fact the same sine wave pattern could be revealed if we extended the analysis to a wider range of inclinations, to have a more comprehensive understanding of the behaviour. Comparing the Inclination Drift Correction Map for different altitudes, the most relevant consideration to be made is the sine-wave pattern for a fixed inclination, while if we fix the RAAN and we look at the corresponding column, all the orbits with the same RAAN experience similar drift, regardless of the initial osculating inclination.

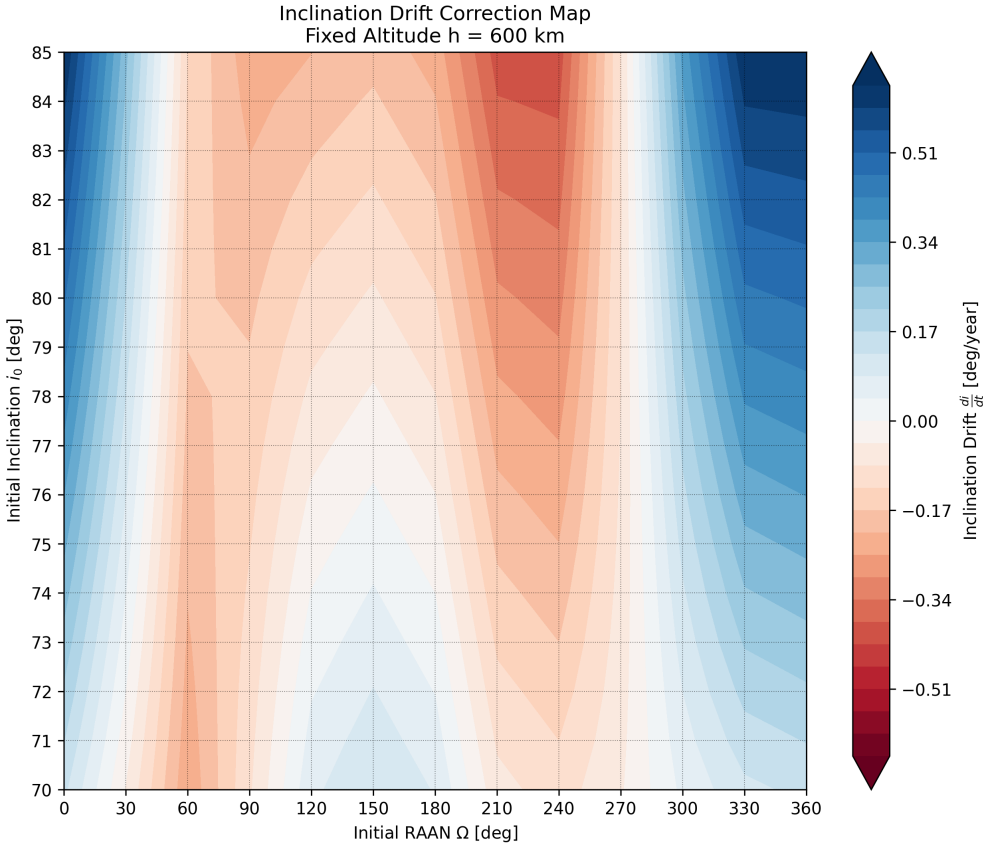


Figure 3.35: Inclination Drift correction map: $\frac{di}{dt}$ linear regression correlated to initial RAAN (Ω) and Inclination (i_0). Initial osculating orbital elements: $h = 600\,\text{km}$.

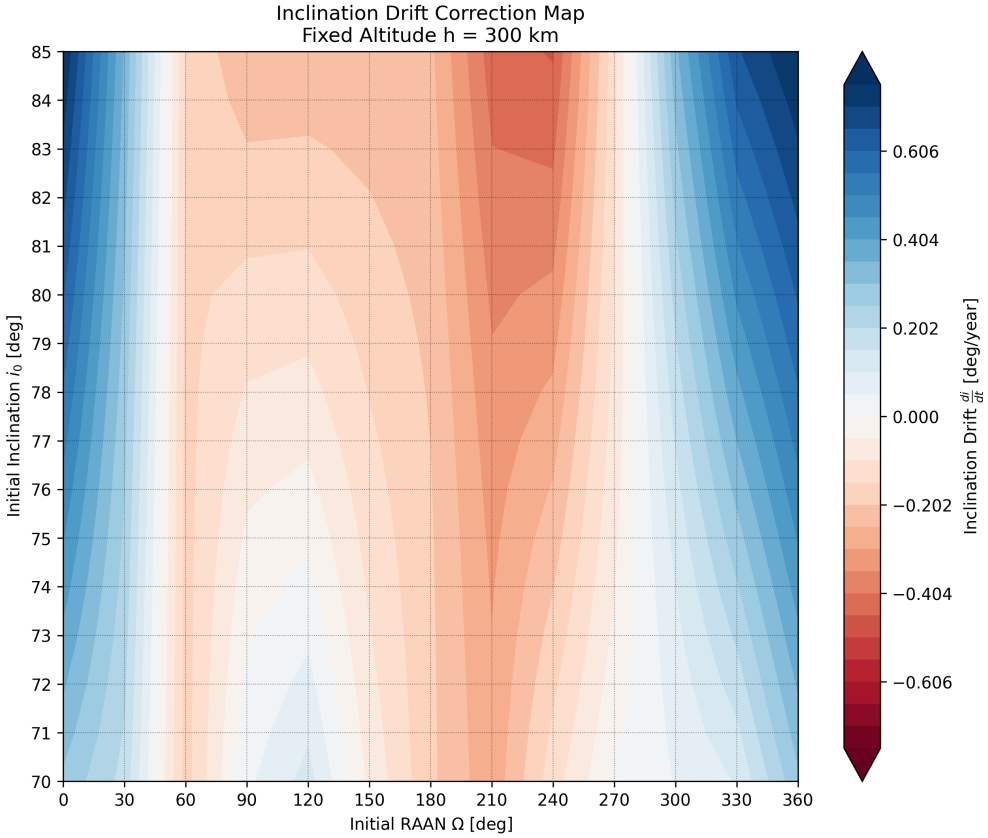


Figure 3.36: Inclination Drift correction map: $\frac{di}{dt}$ linear regression correlated to initial RAAN (Ω) and Inclination (i_0). Initial osculating orbital elements: $h = 300\,\text{km}$.

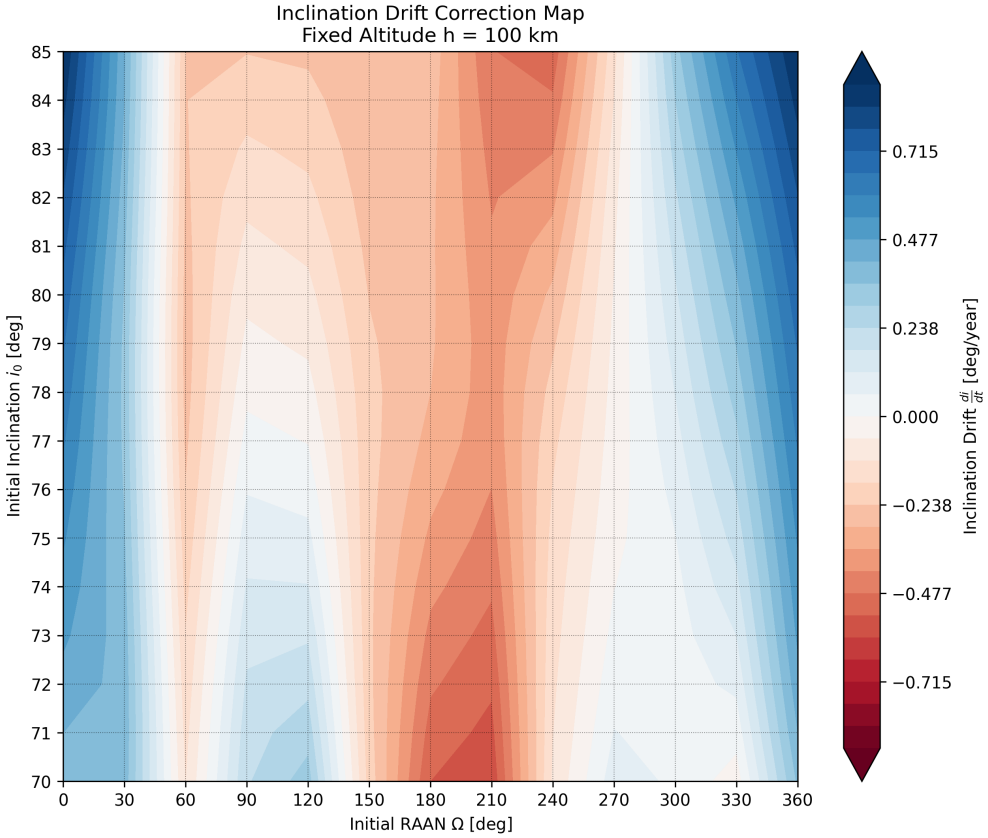


Figure 3.37: Inclination Drift correction map: $\frac{di}{dt}$ linear regression correlated to initial RAAN (Ω) and Inclination (i_0). Initial osculating orbital elements: $h = 100\,\text{km}$.

3.5 Constellations Comparison

After the stability analysis is performed, and the Correction Maps have been computed, a subset of candidate orbits is selected to proceed with a further investigation of the Lunar Constellations. It is now the primary objective of the analysis to verify if the dynamics properties are preserved if the number of satellites of the system is increased, especially regarding the constellation degradation or growth, the frozen stability and the geometric consistency. For this analysis, the best orbits are chosen from the pool of 60 candidates whose properties are represented by Fig. 3.16, 3.17, 3.18 and 3.31, doing a trade-off between the best altitude breathing, eccentricity vector dispersion, argument of peri-apsis amplitude of oscillations and inclination drift, and the 5 chosen candidates are listed in Table 3.4.

h [km]	i [deg]	$min(h_p)$ [km]	h_p stab.[%]	$\Delta\omega$ [deg]	$\Delta\vec{e}$ stab.	$max(\Delta\vec{e})$	$\frac{di}{dt}[\frac{deg}{year}]$
1000	85	983.85	0.75	28.3	0.00079	0.00179	0.274
1000	79	982.28	0.84	36.8	0.00130	0.00273	0.069
800	85	782.18	1.16	33.4	0.00115	0.00257	0.303
800	76	776.99	1.46	43.9	0.00224	0.00445	0.041
600	70	560.80	2.57	36.3	0.00401	0.00739	-0.024

Table 3.4: Best candidates orbits from the frozen stability analysis.

For each orbit, a constellation design process is applied to create a "Design Space" for the Lunar Constellation: a total of 16 different constellations is created for every orbit, where the number of orbital planes goes from 1 to 4, and the number of satellites per plane goes from 2 to 5, so in the Design Space the total number of satellites of the constellation goes from 2 to 20. To account for the gravitational phenomena driven by the Lunar Gravity Field and the Earth's Third-Body, it is necessary to distribute the satellites in a unusual way, breaking the simmetry of the Walker or SoC constellations that are used for Earth applications. In fact, the Inclination Correction Maps computed in the previous sections suggest that if the orbital planes are equally distributed along the equator, each plane will drift with a different rate, leading to a different evolution of the eccentricity vector and the loss of stability. From the SMA Correction Maps it is evident that if the satellites are evenly distributed along the orbit, they are placed on different energetic levels and will orbit around a different value of mean semi-major axis.

For this reason, a new type of Constellation Pattern needs to be developed to optimize the SMA deviation for the satellites in the same orbital plane, and optimize the relative inclination drift between orbital planes. A "Custom" constellation was developed to accomplish this goal, as described by Alg. 27: for a given altitude and inclination, the corrispective Correction Maps are loaded; from the Inclination Map, a number of RAANs equal to the number of planes P is selected by minimizing the relative inclination drift between the P planes, choosing from the row of the matrix imposed by the initial inclination; for every orbital plane, a number of Mean Anomalies equal to the number of satellites per plane is selected by minimizing the relative mean SMA deviation between the S satellites, choosing from the column of the matrix imposed by the current RAAN; the eccentricity and the argument of peri-apsis are selected from the LFO database as always. This type of constellation loses its simmetry, but the 1-year evolution of the orbital elements is planned to be more consistent with the purpose of keeping constant coverage for the duration of

the mission with minimum station-keeping maneuvers. The main difference with a Walker or SoC constellation is that the coverage pattern is less uniform, but it would take much more fuel to mantain a Walker or SoC constellation in a Lunar orbital environment.

Algorithm 27 Generate Custom Constellation

Require: Altitude h, Inclination i, Total Satellites T, Planes P
Ensure: State Matrix $X \in \mathbb{R}^{T \times 6}$

$S \leftarrow T/P$
$a \leftarrow R_{\leftmoon} + h$
$(e, \omega) \leftarrow$ get_LFO(a, i)
$Map_{inc}, Map_{sma} \leftarrow$ LoadMaps(h, i) ▷ Retrieve pre-computed Correction Maps
▷ Phase 1: Optimize RAAN for Minimal Relative Drift
$D \leftarrow \text{Sort}(\{(Map_{inc}[row, j], j \cdot 30 \text{ deg}) \mid j = 0 \dots 11\})$ **by** inclination drift value
if $P = 1$ **then**
    $BestRAANs \leftarrow \{\text{argmin}_{d \in D} |d.drift|\}$
else
    $BestRAANs \leftarrow$ subset of P contiguous elements in D with min range
end if
▷ Phase 2: Optimize Anomaly for Minimal Mean SMA Deviation
$k \leftarrow 0$
for each $c \in BestRAANs$ **do**
    $col \leftarrow \text{round}(c.RAAN_{deg}/15.0)$
    $M_Cand \leftarrow \text{Sort}(\{(Map_{sma}[r, col], r \cdot 15 \text{ deg}) \mid r = 0 \dots 23\})$ **by** mean sma dev
    if $S = 1$ **then**
        $BestM \leftarrow \{\text{argmin}_{m \in M_Cand} |m.dev|\}$
    else
        $BestM \leftarrow$ subset of S contiguous elements in M_Cand with min range
    end if
    for each $m \in BestM$ **do**
        $\nu \leftarrow \text{MeanToTrueAnomaly}(m.M, e)$
        $X[k, :] \leftarrow [a, e, i, \text{deg2rad}(c.RAAN), \omega, \nu]$
        $k \leftarrow k + 1$
    end for
end for
return X

3.5.1 $h = 1000$ km, $i = 85$ deg

The first orbit analyzed is initialized with the orbital elements described by Table 3.5.

T	P	Ω_0 [deg]	M_0 [deg]
2	1	[270]	[30,60]
3	1	[270]	[30,60,345]
4	1	[270]	[150,225,260,315]
5	1	[270]	[30,45,60,240,345]
4	2	[210,240]	[15,30]; [0,315]
6	2	[210,240]	[90,105,270]; [15,45,285]
8	2	[210,240]	[90,105,120,270]; [15,45,240,285]
10	2	[210,240]	[90,105,120,255,270]; [0,120,195,255,315]
6	3	[60,120,150]	[255,330]; [75,255]; [135,180]
9	3	[60,120,150]	[30,90,285]; [45,60,300]; [45,60,270]
12	3	[60,120,150]	[45,165,225,240]; [45,60,105,300]; [45,60,105,270]
15	3	[60,120,150]	[45,165,210,225,240]; [45,60,105,225,300]; [90,120,225,240,285]
8	4	[60,120,150,180]	[255,330]; [75,255]; [135,180]; [120,300];
12	4	[60,120,150,180]	[30,90,285]; [45,60,300]; [45,60,270]; [135,225,315]
16	4	[60,120,150,180]	[45,165,225,240]; [45,60,105,300] [45,60,105,270]; [60,90,120,300]
20	4	[60,120,150,180]	[45,165,210,225,240]; [45,60,105,225,300] [90,120,225,240,285]; [60,90,120,285,300]

Table 3.5: Custom Constellation Design Space for an orbit with initial osculating orbital elements: $h_0 = 1000\,\text{km}$, $i_0 = 85$ deg, $e_0 = 0.004556$ and $\omega_0 = 270$ deg.

The results provided in the following Figures show that all the constellations have similar standard deviation when it comes to SMA, and the performance is not linked to the number of satellites but rather to how well the Custom generation logic is able to find satellites that belong to the same deviation colour of the map, with

the worst result being the constellation with $T = 6$, $P = 2$. The standard deviation of the inclination demonstrates that it does not matter how many satellites there are in a plane, they will all follow the same inclination evolution. As for the number of orbital planes, choosing 3 planes gives slightly better results than choosing a 2 planes configuration. The mean dispersion of the eccentricity vector is an average of both time and satellites of the constellation. Therefore, it tends to increase as the number of satellite is increased, but the order of magnitude for this group of constellations is low enough to indicate a good frozen stability for all the combinations of the group. The relative node drift is also independent on the number of satellites in one plane, and of course it is zero if there is only one plane. The best results are experienced by the constellations with $P = 3$, which have a relative RAAN drift of $\Delta\dot{\Omega} = 0.54\, deg/yr$. The relative mean anomaly drift is the most critical geometrical performance of the constellations, and given the fact that all values are around 200 deg/yr, it is a sizing requirement for the station-keeping Delta-V budget. The constellations with $P = 1$ need less fuel for intra-plane phasing, while good performance belongs to the constellation $T = 4$, $P = 2$, and moreover the less fuel-expensive constellations with a higher number of satellites are $T = 9, P = 3$ and $T = 12, P = 4$. The number of collision avoidance events range from 0 up to 6 for the constellation with $T = 20, P = 4$ and $T = 10, P = 2$.

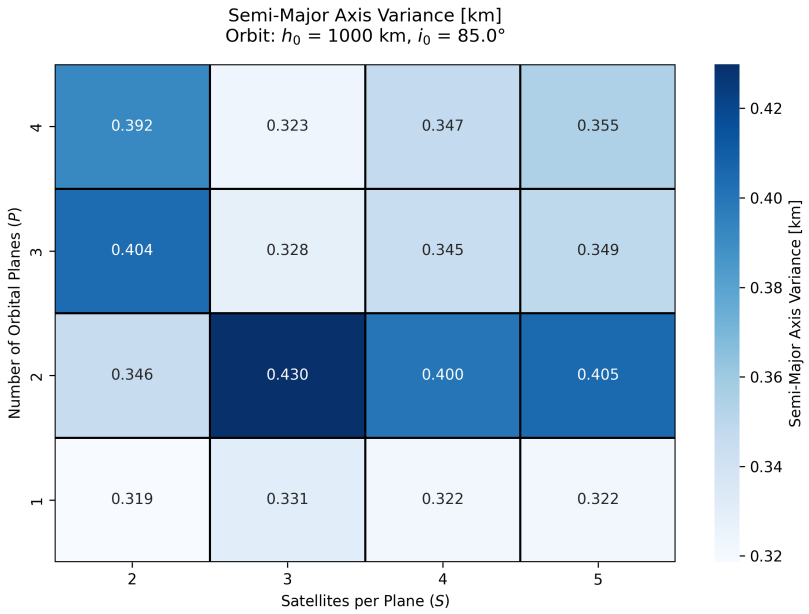


Figure 3.38: Standard Deviation of the Semi-Major Axis for all the constellations of the Design Space at $h = 1000\,\text{km}$ and $i = 85$ deg.

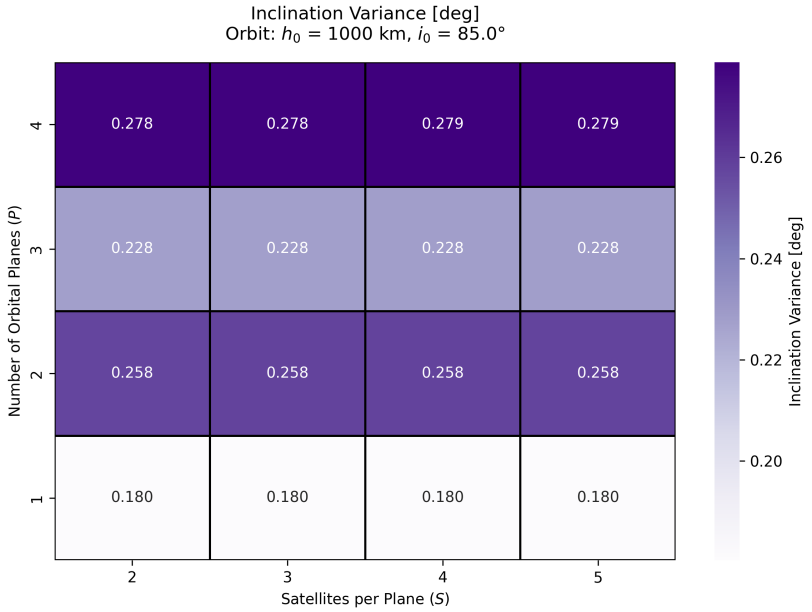


Figure 3.39: Standard Deviation of the Inclination for all the constellations of the Design Space at $h = 1000\,\text{km}$ and $i = 85$ deg.

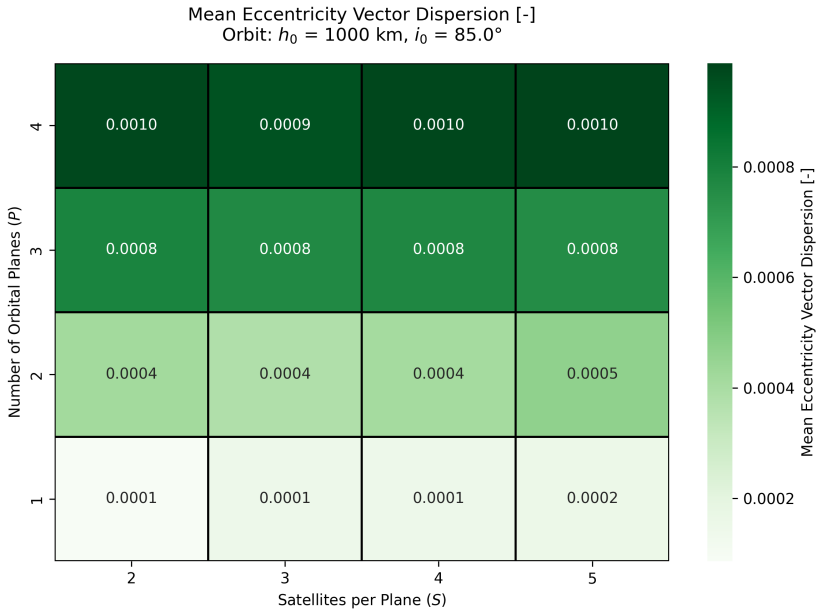


Figure 3.40: Mean Dispersion of the Eccentricity Vector for all the constellations of the Design Space at $h = 1000\,\text{km}$ and $i = 85$ deg.

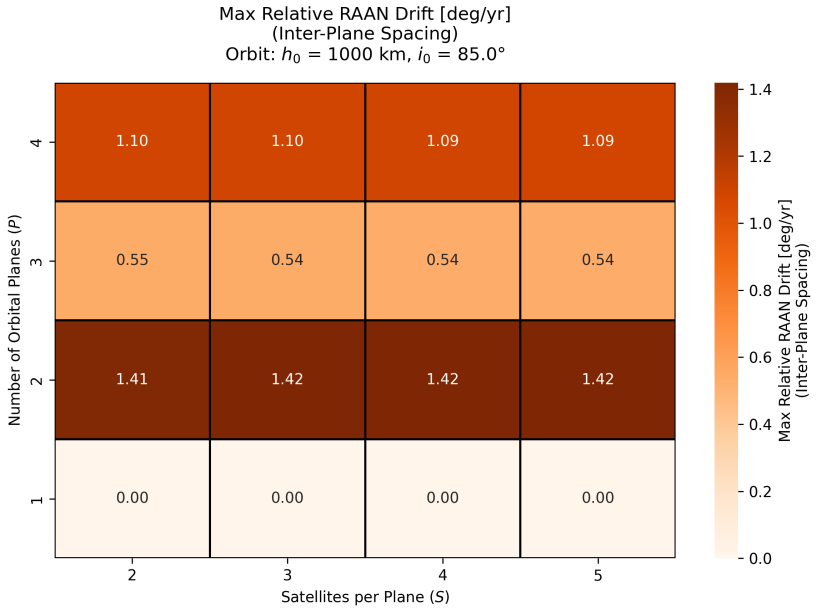


Figure 3.41: Max Slope of the Relative Node Drift (Inter-plane spacing) for all the constellations of the Design Space at $h = 1000\,\text{km}$ and $i = 85$ deg.

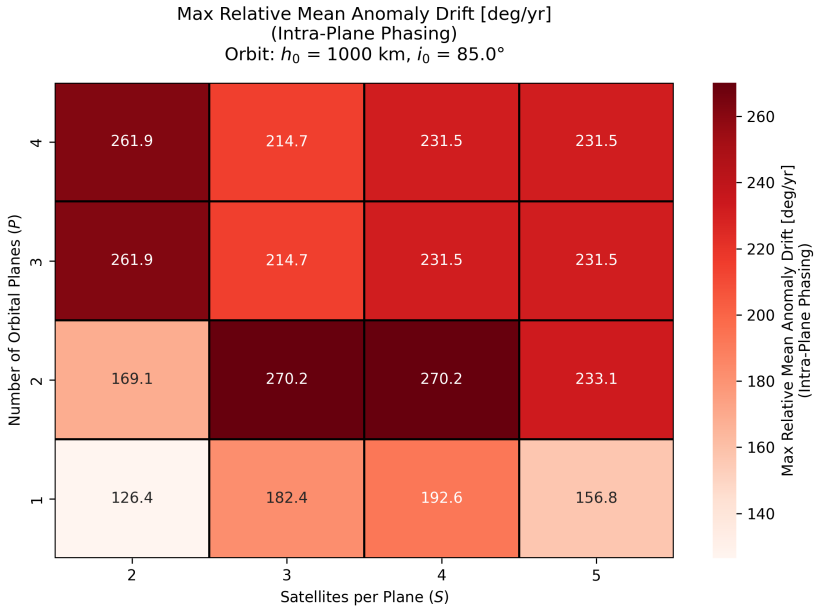


Figure 3.42: Max Slope of the Relative Mean Anomaly Drift (Intra-plane phasing) for all the constellations of the Design Space at $h = 1000\,\text{km}$ and $i = 85$ deg.

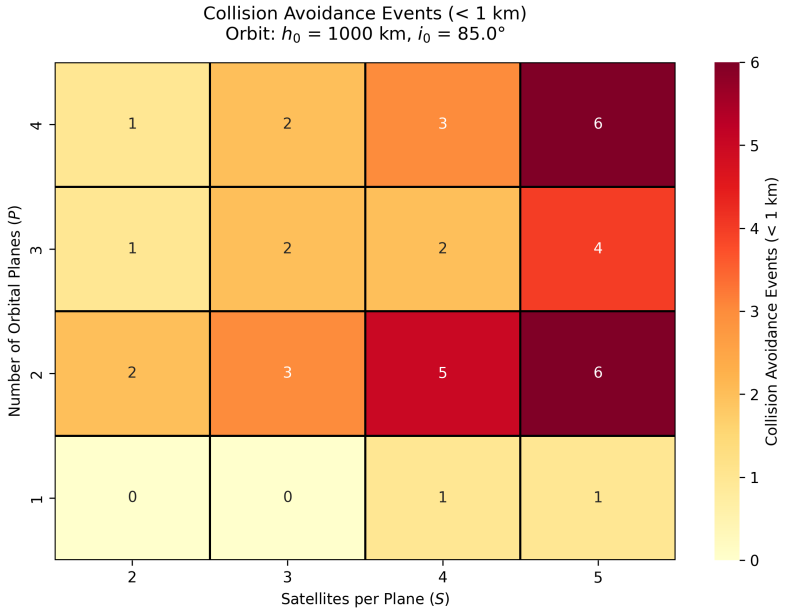


Figure 3.43: Number of Collision Avoidance Events for all the constellations of the Design Space at $h = 1000\,\text{km}$ and $i = 85$ deg.

3.5.2 $h = 1000$ km, $i = 79$ deg

The second best candidate orbit has an altitude of 1000 km and 79 deg inclination.

T	P	Ω_0 [deg]	M_0 [deg]
2	1	[180]	[120,300]
3	1	[180]	[135,225,315]
4	1	[180]	[60,90,120,300]
5	1	[180]	[60,90,120,285,300]
4	2	[90,210]	[135,225]; [15,30]
6	2	[90,210]	[15,135,225]; [90,105,270]
8	2	[90,210]	[15,135,180,225]; [90,105,120,270]
10	2	[90,210]	[15,105,135,180,225]; [90,105,120,255,270]
6	3	[60,90,210]	[255,330]; [135,225]; [15,30]
9	3	[60,90,210]	[30,90,285]; [15,135,225]; [90,105,270]
12	3	[60,90,210]	[45,165,225,240]; [15,135,180,225]; [90,105,120,270]
15	3	[60,90,210]	[45,165,210,225,240]; [15,105,135,180,225]; [90,105,120,255,270]
8	4	[60,90,210,240]	[255,330]; [135,225]; [15,30]; [0,315]
12	4	[60,90,210,240]	[30,90,285]; [15,135,225]; [90,105,270]; [15,45,285]
16	4	[60,90,210,240]	[45,165,225,240]; [15,135,180,225]; [90,105,120,270]; [15,45,240,285];
20	4	[60,90,210,240]	[45,165,210,225,240]; [15,105,135,180,225]; [90,105,120,255,270]; [0,120,195,255,315]

Table 3.6: Custom Constellation Design Space for an orbit with initial osculating orbital elements: $h_0 = 1000\,\text{km}$, $i_0 = 79$ deg, $e_0 = 0.005095$ and $\omega_0 = 270$ deg.

The results are visualized by the following Figures. In most of the cases, choosing 2 satellites per plane gives a lower standard deviation of SMA, while the worst semi-major axis variance is given by the constellations $T = 8, P = 2$ and $T = 6, P = 2$. The worst performance of the inclination evolution is given by the constellations with $P = 2$, while constellations with 4 orbital planes are suitable for applications

since the Delta-V budget for the inclination control will be lower. The mean dispersion of the eccentricity vector is worse compared to the results of the previous candidate orbit (Fig. 3.40), especially comparing the constellations with $P = 2$ or $P = 3$. The constellations with 4 orbital planes have similar frozen stability with respect to the Design Space at $h = 1000\,\text{km}$, $i = 85$ deg, making them more suitable for applications thanks to lower standard deviation of SMA and inclination. The maximum relative node drift is higher than previous results, indicating that more fuel is needed for the inter-plane station-keeping. The maximum intra-plane phasing is less expensive in this case, or even close to zero for the constellation $T = 2, P = 1$. The lower cost of inclination station-keeping will be compensated by a higher relative intra-plane phasing, concerning the worst case scenario which is sizing for the constellation as a whole. This set of initial conditions leads to an overall higher number of collision avoidance events, up to 11 for the most populated constellation $T = 20, P = 4$. It is demonstrated by Fig.3.49 that number of collision avoidance events is influenced by the number of satellites within one plane, because the inter-planes crossing spot is crossed more frequently.

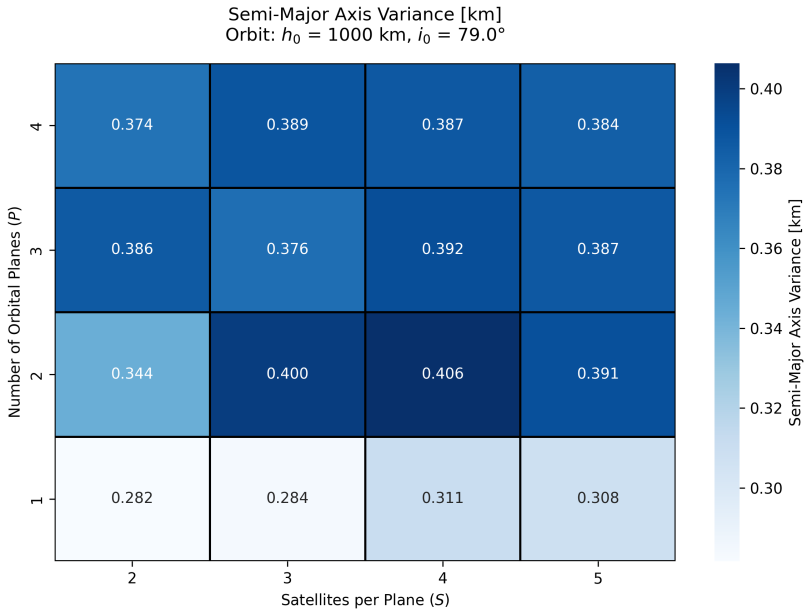


Figure 3.44: Standard Deviation of the Semi-Major Axis for all the constellations of the Design Space at $h = 1000\,\text{km}$ and $i = 79$ deg.

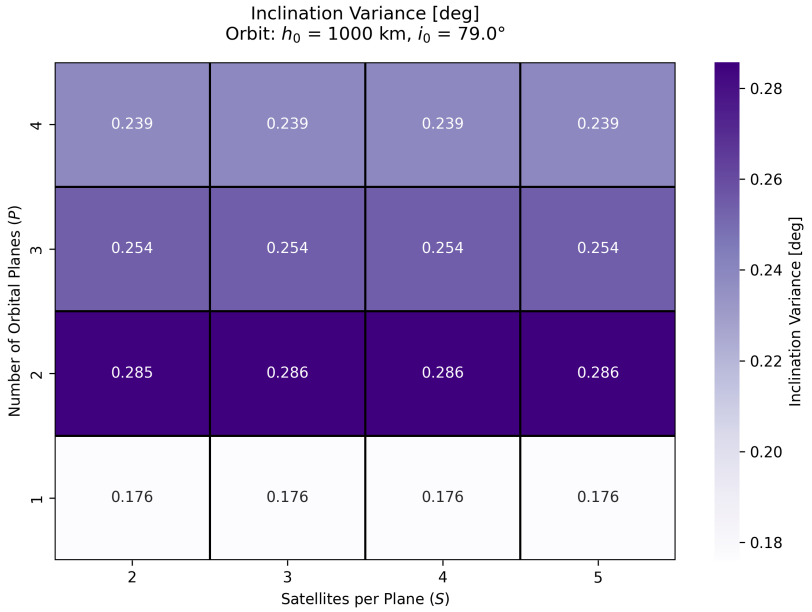


Figure 3.45: Standard Deviation of the Inclination for all the constellations of the Design Space at $h = 1000\,\text{km}$ and $i = 79$ deg.

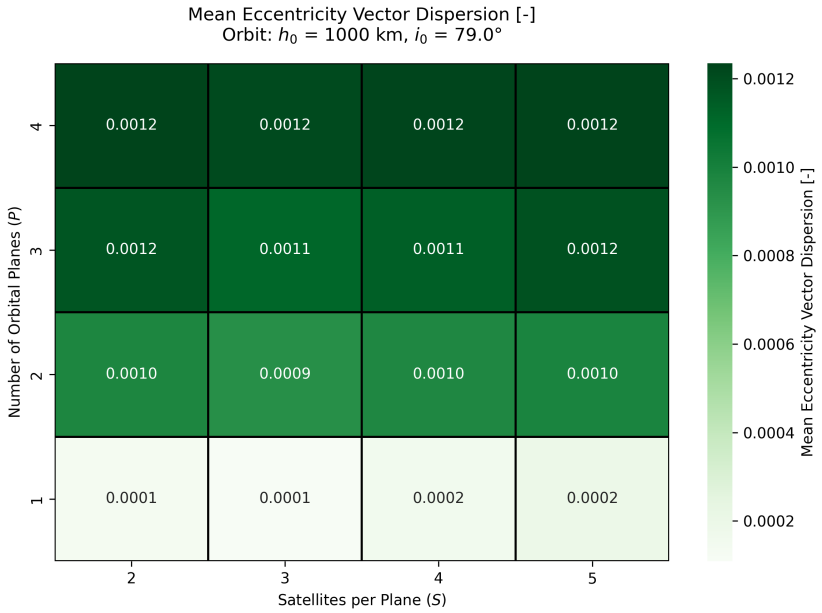


Figure 3.46: Mean Dispersion of the Eccentricity Vector for all the constellations of the Design Space at $h = 1000\,\text{km}$ and $i = 79$ deg.

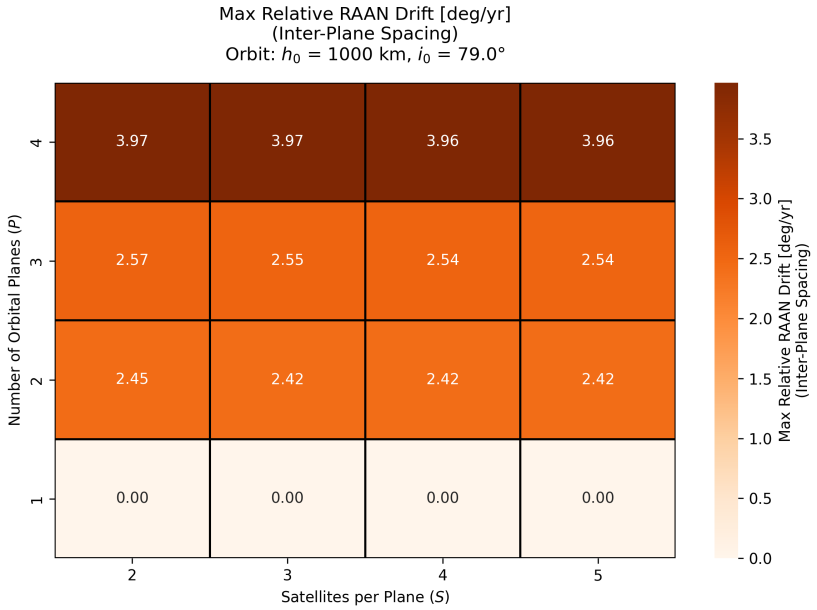


Figure 3.47: Max Slope of the Relative Node Drift (Inter-plane spacing) for all the constellations of the Design Space at $h = 1000\,\text{km}$ and $i = 79$ deg.

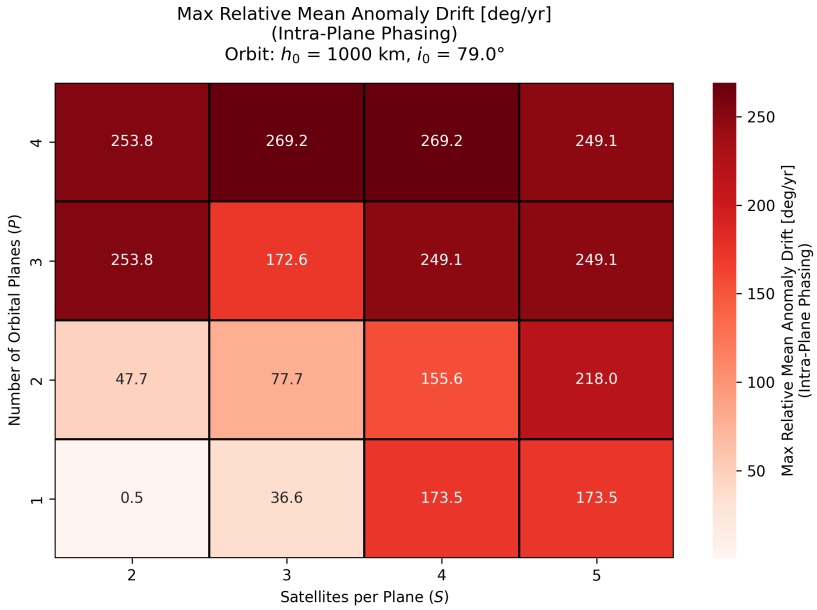


Figure 3.48: Max Slope of the Relative Mean Anomaly Drift (Intra-plane phasing) for all the constellations of the Design Space at $h = 1000\,\text{km}$ and $i = 79$ deg.

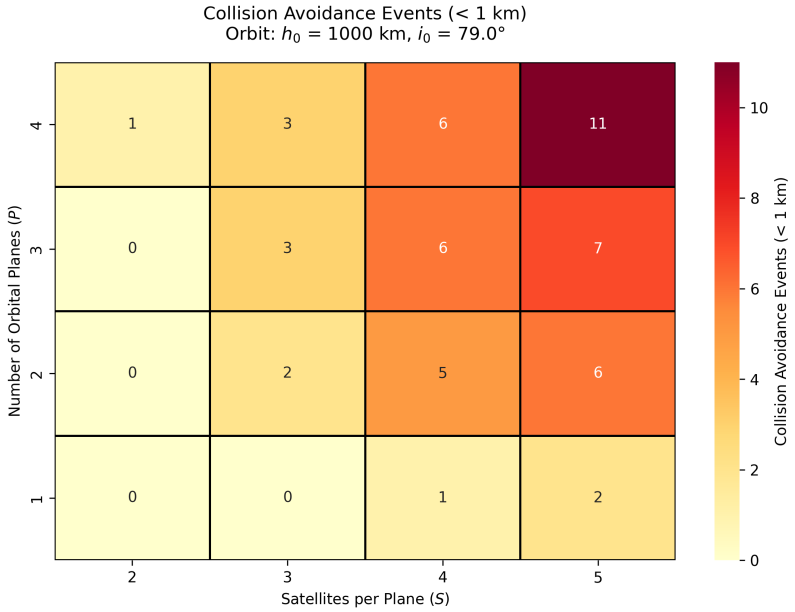


Figure 3.49: Number of Collision Avoidance Events for all the constellations of the Design Space at $h = 1000\,\text{km}$ and $i = 79$ deg.

3.5.3 $h = 800$ km, $i = 85$ deg

The third orbit selected has an altitude of 800 km and an inclination of 85 deg.

T	P	Ω_0 [deg]	M_0 [deg]
2	1	[270]	[90,165]
3	1	[270]	[30,60,240]
4	1	[270]	[30,60,240,345]
5	1	[270]	[30,60,150,240,345]
4	2	[210,240]	[225,240]; [120,255]
6	2	[210,240]	[90,105,120]; [120,195,255]
8	2	[210,240]	[180,225,240,345]; [120,195,255,330]
10	2	[210,240]	[45,180,210,225,240]; [0,120,195,255,315]
6	3	[90,120,180]	[0,195]; [90,330]; [210,330]
9	3	[90,120,180]	[0,195,255]; [0,240,270]; [105,255,270]
12	3	[90,120,180]	[15,135,180,225]; [45,60,105,300]; [60,90,120,300]
15	3	[90,120,180]	[15,105,135,180,225]; [45,60,105,225,300]; [60,90,105,255,270]
8	4	[90,120,150,180]	[0,195]; [90,330]; [135,180]; [210,330]
12	4	[90,120,150,180]	[0,195,255]; [0,240,270]; [0,135,180]; [105,255,270]
16	4	[90,120,150,180]	[15,135,180,225]; [45,60,105,300]; [45,60,105,270]; [60,90,120,300]
20	4	[90,120,150,180]	[15,105,135,180,225]; [45,60,105,225,300]; [0,135,150,180,210]; [60,90,105,255,270]

Table 3.7: Custom Constellation Design Space for an orbit with initial osculating orbital elements: $h_0 = 800$ km, $i_0 = 85$ deg, $e_0 = 0.005328$ and $\omega_0 = 270$ deg.

The standard deviation of the SMA ranges from 0.3 km to 0.45 km in all the possible combinations. The lowest value is given by the constellation $T = 4, P = 2$, while the highest value is $T = 12, P = 4$. A good compromise to achieve a highly populated constellation with good result of SMA variance is $T = 16, P = 4$. As expected from the previous results, the constellations with the lowest values of

inclination variance are the single plane combinations, $P = 1$. In this case, the worst value corresponds to $P = 3$. The mean dispersion of the eccentricity vector is similar to the Constellation Design Space of the orbit $h = 1000\,\text{km}$, $i = 85$ deg, with excellent stability for the constellations with $P = 1$ and $P = 2$, while worst global stability shown by constellations with $P = 4$. The maximum relative node drift has a maximum slope of $\Delta\dot{\Omega} = 1.42$ deg/yr, experienced by the constellations with $P = 2$. The result is coherent with the results of Fig.3.41, because the same i_0 leads to a similar perturbation of the RAANs of the orbital planes, regardless of the initial orbital planes separation $\Delta\Omega_0$. The maximum relative mean anomaly drift is $\Delta\dot{M}_e = 280$ deg/yr, with a peak of 417.7 deg/yr for the constellations $T = 8, P = 2$ and $T = 10, P = 2$. These constellations require too much fuel for station-keeping and shall be avoided, while the preferred combinations are $T = 3, P = 1$ or $T = 4, P = 2$. The trend concerning the number of collision avoidance events is similar to what is shown in Fig.3.49, with a maximum of 12 events for the most populated constellation.

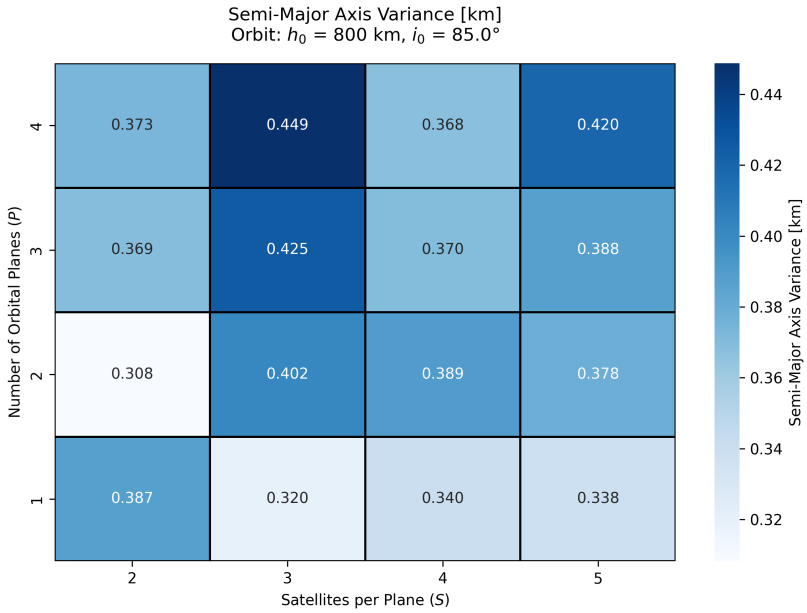


Figure 3.50: Standard Deviation of the Semi-Major Axis for all the constellations of the Design Space at $h = 800\,\text{km}$ and $i = 85$ deg.

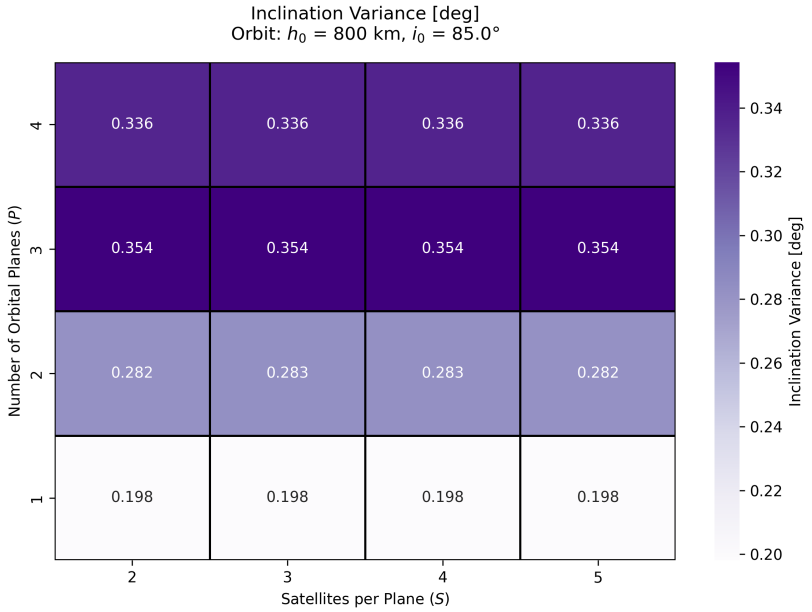


Figure 3.51: Standard Deviation of the Inclination for all the constellations of the Design Space at $h = 800\,\text{km}$ and $i = 85$ deg.

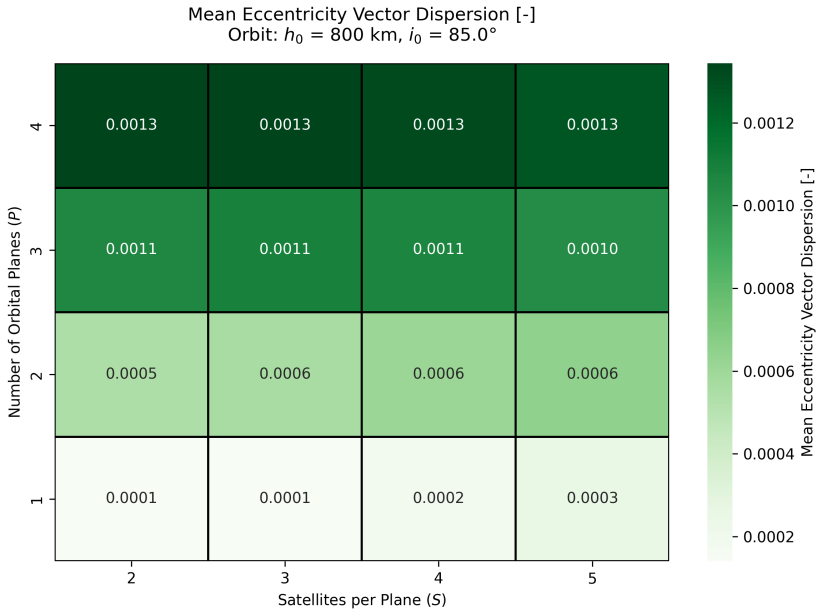


Figure 3.52: Mean Dispersion of the Eccentricity Vector for all the constellations of the Design Space at $h = 800\,\text{km}$ and $i = 85$ deg.

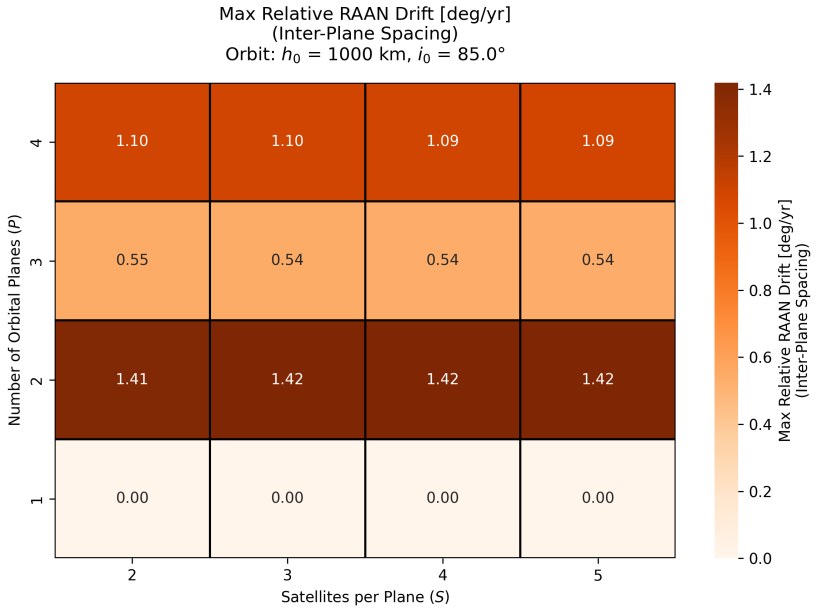


Figure 3.53: Max Slope of the Relative Node Drift (Inter-plane spacing) for all the constellations of the Design Space at $h = 800\,\text{km}$ and $i = 85$ deg.

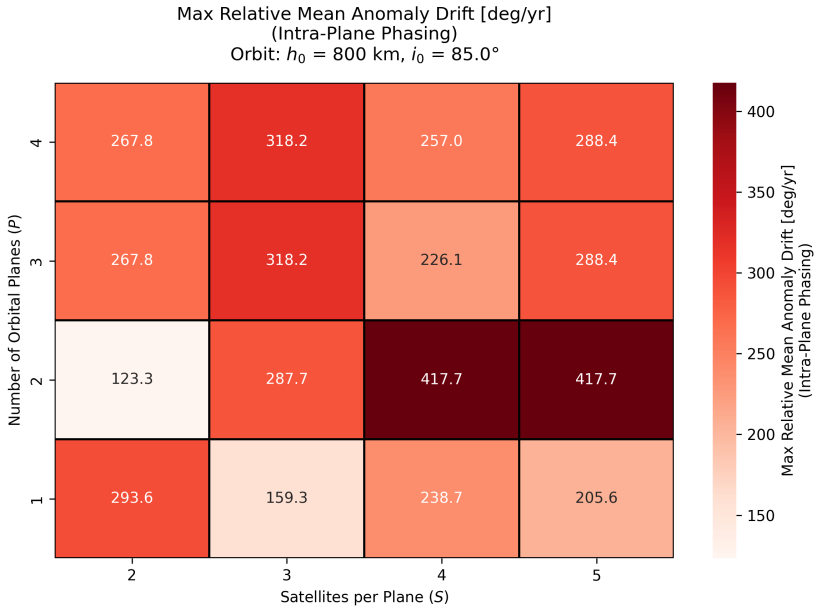


Figure 3.54: Max Slope of the Relative Mean Anomaly Drift (Intra-plane phasing) for all the constellations of the Design Space at $h = 800\,\text{km}$ and $i = 85$ deg.

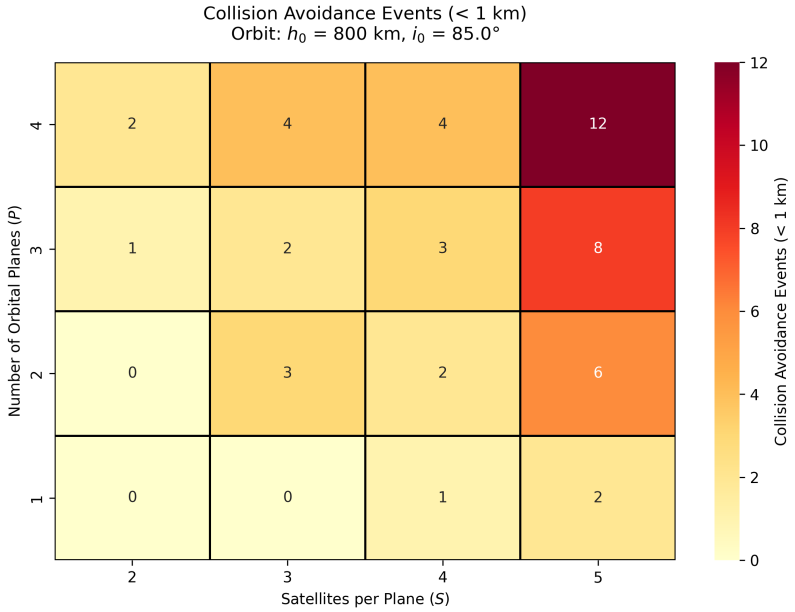


Figure 3.55: Number of Collision Avoidance Events for all the constellations of the Design Space at $h = 800\,\text{km}$ and $i = 85$ deg.

3.5.4 $h = 800$ km, $i = 76$ deg

This candidate orbit has an altitude of 800 km and an inclination of 76 deg.

T	P	Ω_0 [deg]	M_0 [deg]
2	1	[30]	[0,180]
3	1	[30]	[0,15,180]
4	1	[30]	[0,15,30,180]
5	1	[30]	[0,15,30,180,225]
4	2	[30,120]	[0,180]; [75,255]
6	2	[30,120]	[0,15,180]; [45,60,300]
8	2	[30,120]	[0,15,30,180]; [45,60,105,300]
10	2	[30,120]	[0,15,30,180,225]; [45,60,105,225,300]
6	3	[30,120,180]	[0,180]; [75,255]; [120,300]
9	3	[30,120,180]	[0,15,180]; [45,60,300]; [135,225,315]
12	3	[30,120,180]	[0,15,30,180]; [45,60,105,300]; [60,90,120,300]
15	3	[30,120,180]	[0,15,30,180,225]; [45,60,105,225,300] [60,90,120,285,300]
8	4	[60,90,210,240]	[255,330]; [135,225]; [15,30]; [0,315]
12	4	[60,90,210,240]	[30,90,285]; [15,135,225]; [90,105,270]; [15,45,285]
16	4	[60,90,210,240]	[45,165,225,240]; [15,135,165,225]; [90,105,120,270]; [14,45,240,285]
20	4	[60,90,210,240]	[45,165,210,225,240]; [15,105,135,180,225] [90,105,120,255,270]; [0,120,195,255,315]

Table 3.8: Custom Constellation Design Space for an orbit with initial osculating orbital elements: $h_0 = 800$ km, $i_0 = 76$ deg, $e_0 = 0.007078$ and $\omega_0 = 270$ deg.

The results show that the SMA variance ranges again in the interval between 0.2 and 0.5 km. The constellations to avoid because of the expensive station-keeping are $T = 4, P = 2$ and $T = 6, P = 2$, while the best result is obtained by the constellations with $P = 1$. This result is expected for every candidate orbit, because the Alg.27 searches for the minimum SMA deviation among all the satellites within

the same plane, but it does not search for a mean value of SMA where all the satellites of one constellation oscillates around it. The inclination variance is below 0.2 deg only for constellations with $P = 1$, while the second best option would be to have $P = 4$. The stability behaviour is less strong for constellations with more than one plane, therefore it is needed more station-keeping budget to mantain the frozen condition of the constellations stable over time. The results concerning the relative node drift are excellent for constellations with $P = 2$ and $P = 3$, while constellations with $P = 4$ require higher Delta-V budget to keep geometric stability. The maximum relative mean anomaly drift is high for constellations with $P = 4$ or $S = 4$, and the best result is given by $S = 2$. The number of collisions is relatively lower than other constellation groups, allowing us to deploy constellations like $T = 10, P = 2$, $T = 12, P = 4$ and $T = 12, P = 3$ without the need to plan a lot of collision avoidance maneuvers.

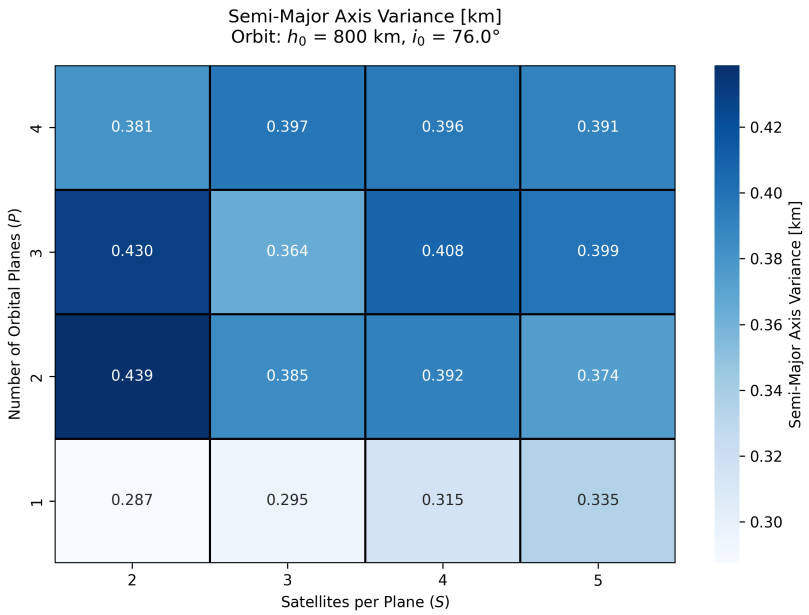


Figure 3.56: Standard Deviation of the Semi-Major Axis for all the constellations of the Design Space at $h = 800$ km and $i = 76$ deg.

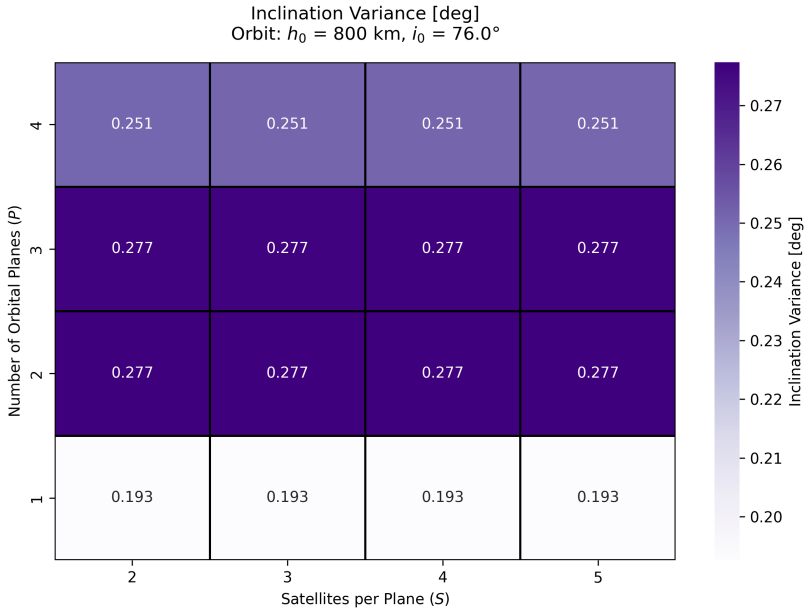


Figure 3.57: Standard Deviation of the Inclination for all the constellations of the Design Space at $h = 800\,\text{km}$ and $i = 76$ deg.

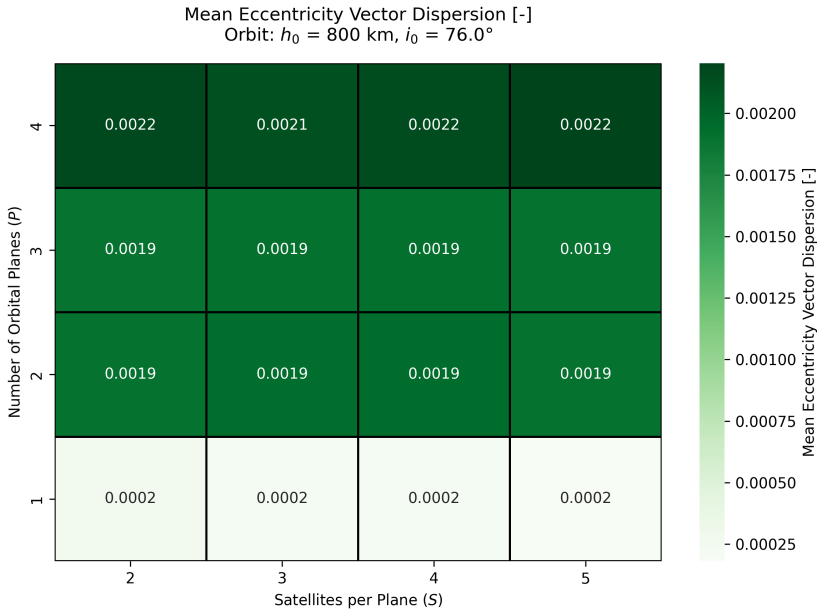


Figure 3.58: Mean Dispersion of the Eccentricity Vector for all the constellations of the Design Space at $h = 800\,\text{km}$ and $i = 76$ deg.

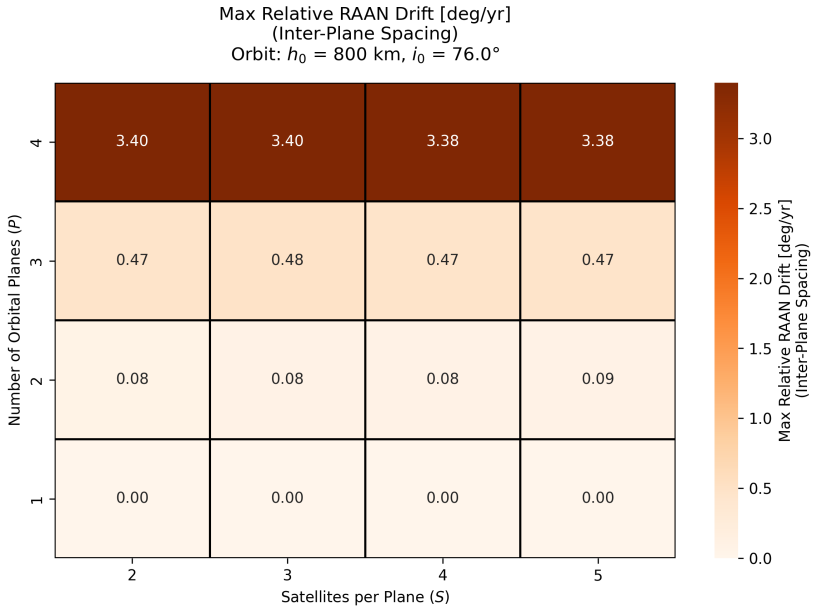


Figure 3.59: Max Slope of the Relative Node Drift (Inter-plane spacing) for all the constellations of the Design Space at $h = 800\,\text{km}$ and $i = 76$ deg.

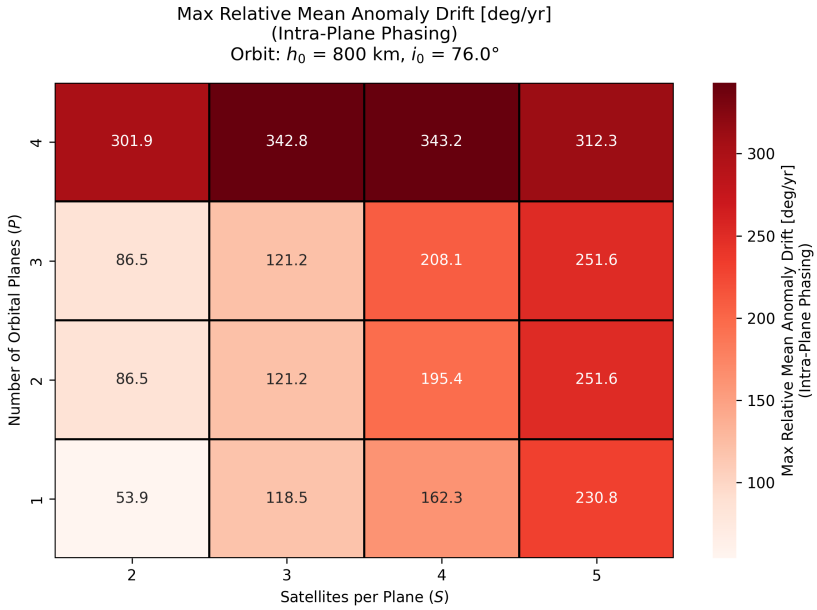


Figure 3.60: Max Slope of the Relative Mean Anomaly Drift (Intra-plane phasing) for all the constellations of the Design Space at $h = 800\,\text{km}$ and $i = 76$ deg.

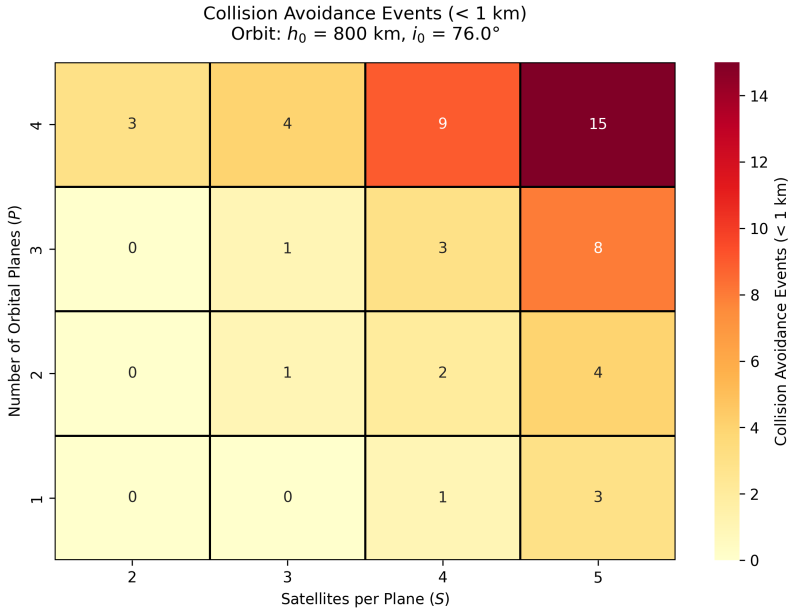


Figure 3.61: Number of Collision Avoidance Events for all the constellations of the Design Space at $h = 800\,\text{km}$ and $i = 76$ deg.

3.5.5 $h = 600$ km, $i = 70$ deg

The last group of constellations analyzed consists of an orbit with 600 km of altitude and 70 deg of inclination.

T	P	Ω_0 [deg]	M_0 [deg]
2	1	[30]	[165,210]
3	1	[30]	[0,180,225]
4	1	[30]	[0,30,180,225]
5	1	[30]	[0,15,30,180,225]
4	2	[30,270]	[165,210]; [30,60]
6	2	[30,270]	[0,180,225]; [30,60,240]
8	2	[30,270]	[0,30,180,225]; [45,105,150,345]
10	2	[30,270]	[0,15,30,180,225]; [30,60,105,150,345]
6	3	[0,150,330]	[30,150]; [150,330]; [45,225]
9	3	[0,150,330]	[165,180,210]; [150,210,330]; [60,75,270]
12	3	[0,150,330]	[15,180,195,210]; [0,150,210,330]; [15,135,195,330]
15	3	[0,150,330]	[15,165,180,195,210]; [0,135,150,210,330]; [15,135,165,195,330]
8	4	[30,90,210,270]	[165,210]; [165,210]; [180,240]; [30,60]
12	4	[30,90,210,270]	[0,180,225]; [90,165,210]; [180,240,345]; [30,60,240]
16	4	[30,90,210,270]	[0,30,180,225]; [90,165,210,345]; [180,225,240,345]; [45,105,150,345]
20	4	[30,90,210,270]	[0,15,30,180,225]; [90,165,210,285,345]; [90,105,120,255,270]; [30,60,105,150,345]

Table 3.9: Custom Constellation Design Space for an orbit with initial osculating orbital elements: $h_0 = 600$ km, $i_0 = 70$ deg, $e_0 = 0.014486$ and $\omega_0 = 270$ deg.

The performance results for this orbit group are showcased by images below. It is important to specify that this orbit has been chosen as a potential candidate to host Lunar Constellations for lower altitudes, in order to achieve a greater resolution for the surface observation. The variance of SMA is on average around 0.35 km,

similarly to previous results. Some constellations to avoid are $T = 20, P = 4$ and $T = 9, P = 3$, which experience the peak of standard deviation at 0.417 km. The standard deviation of the inclination gives overall worse results than previous orbit groups, with better performance given by constellations with $P = 1$ and $P = 3$. The frozen stability needs higher Delta-V budget to be kept within the chosen boundaries, because the eccentricity vector dispersion rises to over 0.002 in all of the cases with more than one orbital plane. The inter-plane station-keeping is highly expensive for $P = 4$ and $P = 2$, while an acceptable value is experienced by constellations with $P = 3$ as the relative node drift is $\Delta\dot{\Omega} = 2.15$ deg/yr on average. The maximum relative mean anomaly drift is too high for constellations with $P = 4$, reaching a peak of $\Delta\dot{M}_e = 525$ deg/yr which is enough to discard the constellations $T = 8, P = 4$, $T = 12, P = 4$ and $T = 16, P = 4$ from potential applications. The best result is reached by the constellation $T = 6, P = 2$, with a maximum drift of 107.4 deg/yr. The number of collision avoidance events does not increase as the altitude of the constellations is decreased, and even though the orbital period of the orbits is faster and the orbits are crossed more frequently, the amount of fuel needed for collosion avoidance maneuvers is unaffected.

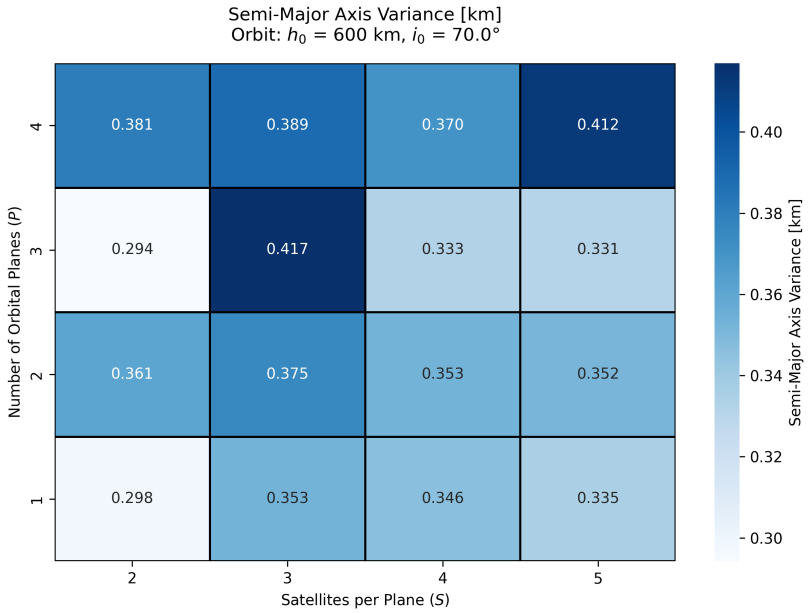


Figure 3.62: Standard Deviation of the Semi-Major Axis for all the constellations of the Design Space at $h = 600$ km and $i = 70$ deg.

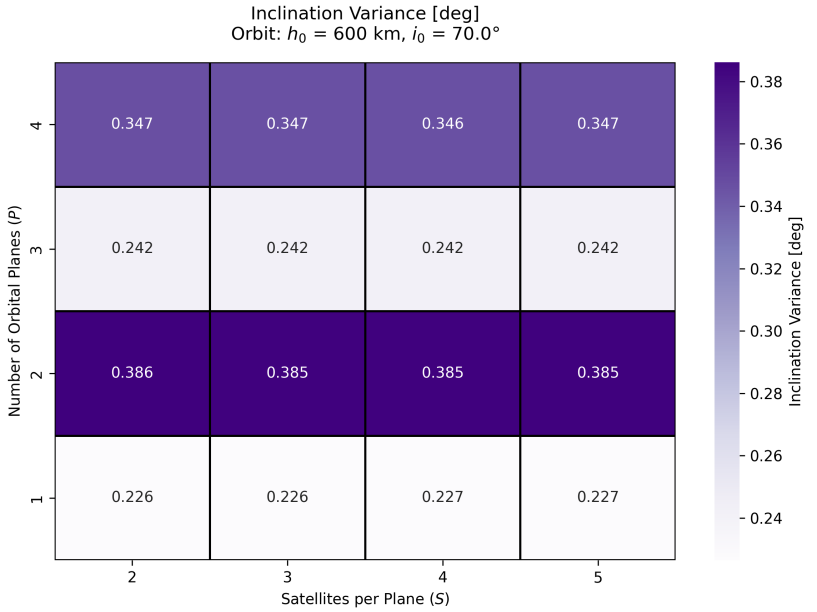


Figure 3.63: Standard Deviation of the Inclination for all the constellations of the Design Space at $h = 600\,\text{km}$ and $i = 70$ deg.

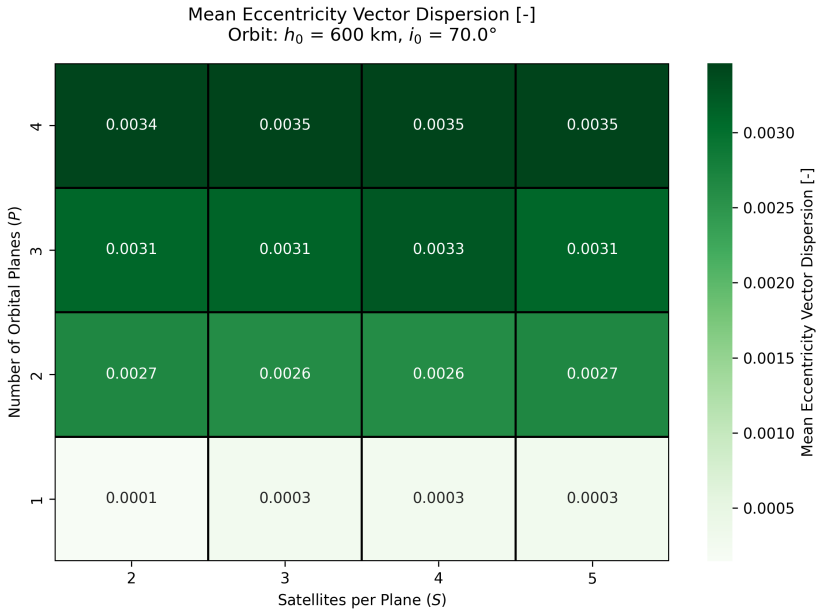


Figure 3.64: Mean Dispersion of the Eccentricity Vector for all the constellations of the Design Space at $h = 600\,\text{km}$ and $i = 70$ deg.

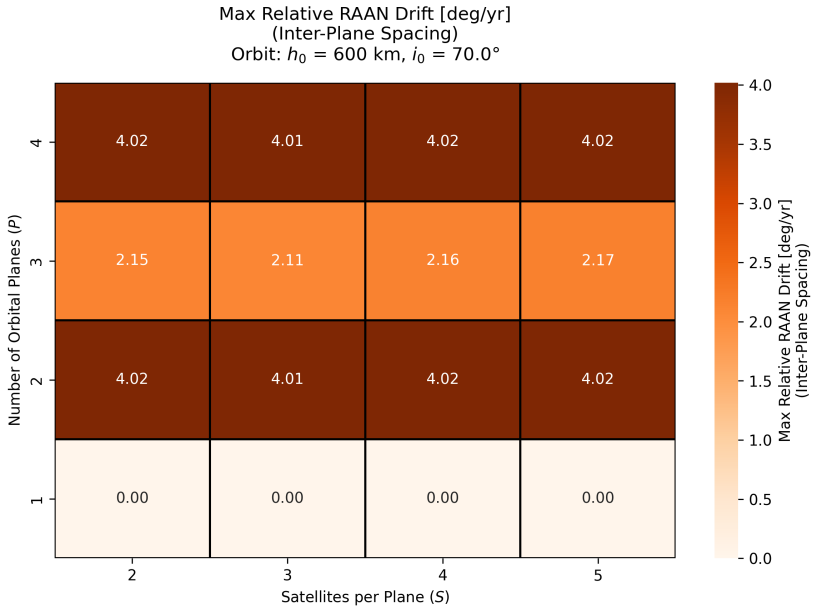


Figure 3.65: Max Slope of the Relative Node Drift (Inter-plane spacing) for all the constellations of the Design Space at $h = 600\,\text{km}$ and $i = 70$ deg.

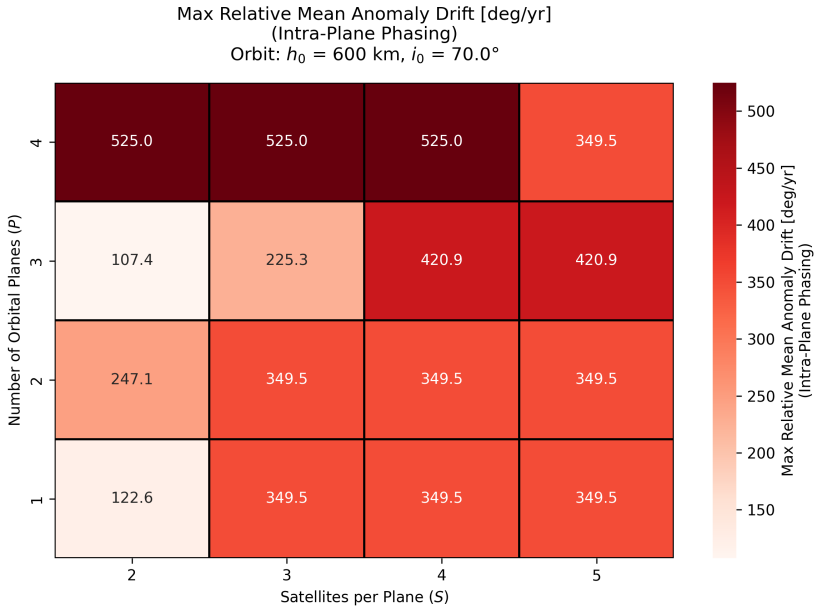


Figure 3.66: Max Slope of the Relative Mean Anomaly Drift (Intra-plane phasing) for all the constellations of the Design Space at $h = 600\,\text{km}$ and $i = 70$ deg.

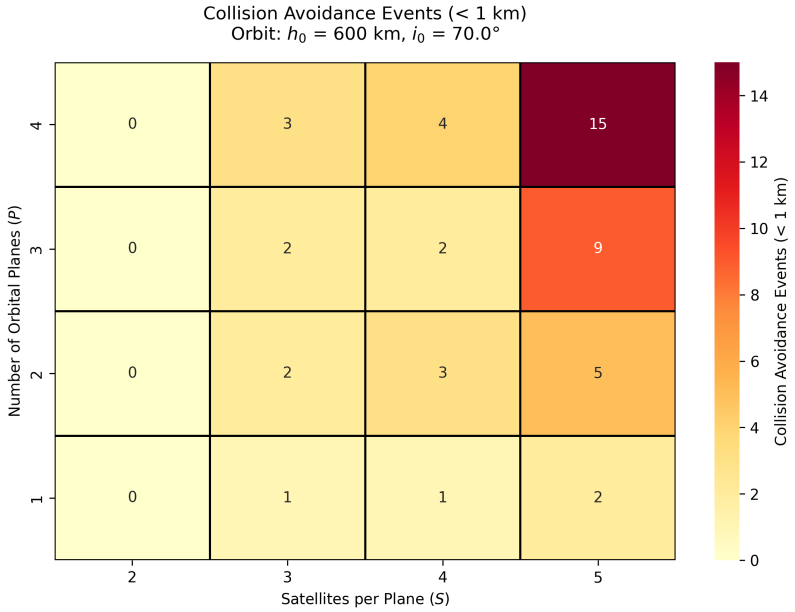


Figure 3.67: Number of Collision Avoidance Events for all the constellations of the Design Space at $h = 600\,\text{km}$ and $i = 70$ deg.

Chapter 4

Conclusions

The renewed global interest in establishing a permanent human presence on the Moon, spearheaded by initiatives such as NASA's Artemis program and ESA's Moonlight, demands reliable navigation and communication infrastructures. Unlike the Earth's orbital environment, the Moon presents a highly irregular gravitational field characterized by mass concentrations (Mascons) and significant third-body perturbations from the Earth. This thesis investigated the dynamical feasibility of deploying standard Earth-like constellation architectures (specifically Walker Delta, Walker Star, and Streets of Coverage patterns) into the lunar environment by exploiting the theory of Lunar Frozen Orbits (LFOs). The primary goal was to thoroughly examine the physical survivability and geometric stability of these constellations under realistic perturbing forces over long durations.

To accurately capture the chaotic dynamics of cislunar space, a high-fidelity numerical propagator was developed in Python. This tool integrated the full non-linear equations of motion using Cowell's Method and an 8th-order Dormand-Prince solver. The simulation environment incorporated the high-resolution GRAIL gravity model to accurately map lunar mascons and utilized the NASA SPICE toolkit to retrieve precise ephemerides for Earth's third-body tidal acceleration. By systematically propagating thousands of initial conditions for one year, the methodology bridged the gap between analytical double-averaging theories and the actual long-term behavior of satellite tracks.

The initial phase of the study mapped the solution space of Lunar Frozen Orbits across a grid of altitudes and inclinations. The numerical propagation revealed that while Earth-like patterns can survive in lunar orbit, their stability is strictly bounded by specific orbital regimes. Most orbits above an altitude of 300 km demonstrated safe behavior with minimal perilune decay, maintaining their frozen condition and securing the satellite's survival. Conversely, Low Lunar Orbits below 200 km proved

highly sensitive to mascons, suffering from rapid perilune altitude degradation and severe eccentricity vector dispersion, rendering them unstable and highly prone to surface impact. Furthermore, the stability analysis identified a critical region near the 57 degrees inclination mark where stable frozen conditions could not be maintained, resulting in the circulation rather than libration of the argument of perilune.

Even within stable LFO regimes, a critical discrepancy was observed between the mean orbital elements defined by the analytical theory and the osculating elements required for high-fidelity initialization. This misalignment generated short-period energy variations, causing satellites to oscillate around different mean semi-major axes. Such deviations translate directly into in-plane dephasing, destroying the constellation's geometric symmetry over time. Similarly, differential inclination drift was observed among orbital planes deployed at different Right Ascensions of the Ascending Node (RAAN), further threatening the constellation's coverage. To counteract this without relying on continuous active station-keeping, "Correction Maps" were computed. These maps successfully correlated the secular drift of both the semi-major axis and the inclination to the initial osculating RAAN and Mean Anomaly.

Leveraging the Correction Maps, a novel process was established to generate custom lunar constellations. By deliberately selecting specific RAANs and Mean Anomalies that minimized relative semi-major axis deviation and inclination drift, these custom configurations optimized the natural dynamics of the lunar environment. While this adaptation inherently breaks the perfect symmetry typical of standard Walker or Streets of Coverage patterns, the custom constellations demonstrated vastly superior geometric stability and consistent performance throughout the one-year propagation. The simulations proved that Earth-like constellation patterns are indeed feasible for lunar operations, but only on the strict condition that their parameters are carefully adjusted to lock into the frozen dynamic equilibrium condition.

The findings of this research establish a robust dynamical baseline for the preliminary design of future lunar navigation and communication constellations. By validating the physical survivability of adapted architectures, this work provides a framework that prioritizes passive geometric stability. Future research should build upon this foundation by converting the observed geometric drifts into quantitative station-keeping budget requirements. Extending the analysis to include active control mechanisms and more complex trade-offs involving launch costs, coverage precision or link budgets will provide a comprehensive mission architecture for the next generation of lunar infrastructure.

Bibliography

[1] The Business Research Company. *Lunar Exploration Global Market Report 2025*. Market Report. The Business Research Company, Jan. 2025. URL: https://www.thebusinessresearchcompany.com/report/lunar-exploration-global-market-report (cit. on p. 1).

[2] NASA. *NASA's Plan for Sustained Lunar Exploration and Development*. 2020 (cit. on p. 1).

[3] Marshall Smith, Douglas Craig, Nicole Herrmann, Erin Mahoney, Jonathan Krezel, Nate McIntyre, and Kandyce Goodliff. «The artemis program: An overview of nasa's activities to return humans to the moon». In: *2020 IEEE aerospace conference*. IEEE. 2020, pp. 1–10 (cit. on p. 1).

[4] ESA Applications. *ESA identifies demand for satellites around the Moon*. URL: https://www.esa.int/Applications/Connectivity_and_Secure_Communications/ESA_identifies_demand_for_satellites_around_the_Moon (cit. on p. 1).

[5] ESA Applications. *Moonlight: Connecting Earth with the Moon*. URL: https://www.esa.int/Applications/Connectivity_and_Secure_Communications/Moonlight_connecting_Earth_with_the_Moon (cit. on p. 1).

[6] Francesco Lopez, Anna Mauro, Stefano Mauro, Giuseppe Monteleone, Domenico Edoardo Sfasciamuro, and Andrea Villa. «A lunar-orbiting satellite constellation for wireless energy supply». In: *Aerospace* 10.11 (2023), p. 919 (cit. on p. 1).

[7] Sang-Uk Lee, Jae-Hoon Kim, and Seong-Pal Lee. «Communications satellite system by using moon orbit satellite constellation». In: *Journal of Astronomy and Space Sciences* 20.4 (2003), pp. 313–318 (cit. on pp. 1, 2).

[8] Richard Vondrak, John Keller, Gordon Chin, and James Garvin. «Lunar Reconnaissance Orbiter (LRO): Observations for lunar exploration and science». In: *Space science reviews* 150.1 (2010), pp. 7–22 (cit. on p. 1).

[9] John E Prussing and Bruce A Conway. «Orbital mechanics». In: *The Aeronautical Journal* () (cit. on p. 5).

[10] Roger R. Bate, Donald D. Mueller, and Jerry E. White. *Fundamentals of Astrodynamics*. eng. Dover books on astronomy and astrophysics. New York: Dover, 1971 (cit. on pp. 8, 10, 15, 18, 69).

[11] R.M.L. Baker and M.W. Makemson. *An Introduction to Astrodynamics*. Advances in space science. Academic Press, 1960. URL: https://books.google.it/books?id=kN3PAAAAMAAJ (cit. on pp. 11, 38).

[12] David A Vallado. *Fundamentals of astrodynamics and applications*. Vol. 12. Springer Science & Business Media, 2001 (cit. on pp. 12, 13).

[13] H Goldstein, C Poole, J Safko, et al. *1., Classical Mechanics*. 1980 (cit. on p. 13).

[14] James G Williams, Slava G Turyshev, and Dale H Boggs. «The past and present Earth-Moon system: the speed of light stays steady as tides evolve». In: *Planetary science* 3.1 (2014), p. 2 (cit. on pp. 17, 24).

[15] NASA JPL. *JPL Planetary and Lunar Ephemerides*. 2020. URL: https://ssd.jpl.nasa.gov/planets/eph_export.html (cit. on p. 18).

[16] Carl D Murray and Stanley F Dermott. *Solar system dynamics*. Cambridge university press, 1999 (cit. on pp. 18, 24).

[17] IAU. *Nomenclature for Fundamental Astronomy*. 2007. URL: https://syrte.obspm.fr/iauWGnfa/NFA_Glossary.html (cit. on p. 19).

[18] UNOOSA. *Lunar Reference Frame and Lunar Time - ESA's View*. 2024. URL: https://www.unoosa.org/documents/pdf/icg/2024/WG-B_Lunar_PNT_Jun24/LunarPNT_Jun24_02_04.pdf (cit. on p. 19).

[19] NASA. *Lunar Reference Frames*. 2024. URL: https://www.nasa.gov/wp-content/uploads/2024/12/acr24-lunar-reference-frames.pdf?emrc=4de7e5 (cit. on pp. 19, 23).

[20] C Ma, EF Arias, TMm Eubanks, AL Fey, A-M Gontier, CS Jacobs, OJ Sovers, BA Archinal, and P Charlot. «The International Celestial Reference Frame as Realized by VeryLong Baseline Interferometry». In: *The Astronomical Journal* 116.1 (1998), p. 516 (cit. on p. 19).

[21] Brent Allen Archinal et al. «Report of the IAU working group on cartographic coordinates and rotational elements: 2009». In: *Celestial Mechanics and Dynamical Astronomy* 109.2 (2011), pp. 101–135 (cit. on pp. 21, 22, 52).

[22] Ryan S Park, William M Folkner, James G Williams, and Dale H Boggs. «The JPL planetary and lunar ephemerides DE440 and DE441». In: *The Astronomical Journal* 161.3 (2021), p. 105 (cit. on p. 21).

[23] NASA JPL. *NASA SPICE Toolkit*. 2022. URL: https://naif.jpl.nasa.gov/naif/toolkit.html (cit. on pp. 21, 25, 55).

[24] Rita Mastroianni, Edoardo Legnaro, and Christos Efthymiopoulos. «Fully analytical propagator for lunar satellite orbits in closed form». In: *arXiv preprint arXiv:2505.09241* (2025) (cit. on pp. 22, 23, 25).

[25] Christos Efthymiopoulos, Kleomenis Tsiganis, Ioannis Gkolias, Michalis Gaitanas, and Carlos Yanez. «Selena: Semi-analytical integrator for lunar artificial satellites». In: *arXiv preprint arXiv:2309.11904* (2023) (cit. on pp. 22, 23).

[26] Daniel W Lozier. «NIST digital library of mathematical functions». In: *Annals of Mathematics and Artificial Intelligence* 38.1 (2003), pp. 105–119 (cit. on p. 23).

[27] NASA Department of Earth and Planetary Sciences. *PDS Geosciences Node*. URL: `https://pds-geosciences.wustl.edu/grail/grail-l-lgrs-5-rdr-v1/grail` (cit. on p. 23).

[28] Frank G Lemoine et al. «GRGM900C: A degree 900 lunar gravity model from GRAIL primary and extended mission data». In: *Geophysical research letters* 41.10 (2014), pp. 3382–3389 (cit. on p. 23).

[29] Sea Goossens et al. «A global degree and order 1200 model of the lunar gravity field using GRAIL mission data». In: *47th Annual Lunar and Planetary Science Conference*. 1903. 2016, p. 1484 (cit. on p. 23).

[30] NASA JPL. *GRAIL - Moon Missions*. 2011. URL: `https://www.jpl.nasa.gov/missions/gravity-recovery-and-interior-laboratory-grail/` (cit. on p. 23).

[31] C. Hirt and W.E. Featherstone. «A 1.5km-resolution gravity field model of the Moon». In: *Earth and Planetary Science Letters* 329-330 (2012), pp. 22–30 (cit. on p. 23).

[32] eoPortal. *GRAIL (Gravity Recovery and Interior Laboratory)*. 2012. URL: `https://www.eoportal.org/satellite-missions/grail#references` (cit. on p. 23).

[33] Luc Blanchet. «On the multipole expansion of the gravitational field». In: *Classical and Quantum Gravity* 15.7 (1998), p. 1971 (cit. on p. 24).

[34] Wang Sang Koon, Martin W Lo, Jerrold E Marsden, and Shane D Ross. «Dynamical systems, the three-body problem and space mission design». In: *Equadiff 99: (In 2 Volumes)*. World Scientific, 2000, pp. 1167–1181 (cit. on p. 25).

[35] Daniel C Qi and Kenshiro Oguri. «Analysis of autonomous orbit determination in various near-moon periodic orbits». In: *The Journal of the Astronautical Sciences* 70.6 (2023), p. 49 (cit. on p. 26).

[36] Sanguk Lee, J. W. Kim, and Seong-Pal Lee. «Communications Satellite System by Using Moon Orbit Satellite Constellation». In: *Journal of Astronomy and Space Sciences* 20 (Dec. 2003), pp. 313–318. DOI: 10.5140/JASS.2003.20.4.313 (cit. on p. 26).

[37] David Folta and David Quinn. «Lunar frozen orbits». In: *AIAA/AAS Astrodynamics Specialist Conference and Exhibit*. 2006, p. 6749 (cit. on pp. 26, 82).

[38] M Shirobokov, S Tromov, and M Ovchinnikov. «Lunar frozen orbits for small satellite communication/navigation constellations». In: *Proceedings of the International Astronautical Congress, IAC*. 2021 (cit. on p. 26).

[39] Mikhail Ovchinnikov, Maksim Shirobokov, and Sergey Trofimov. «Lunar Satellite Constellations in Frozen Low Orbits». In: *Aerospace* 11.11 (2024), p. 918 (cit. on p. 26).

[40] Tao Nie and Pini Gurfil. «Lunar frozen orbits revisited». In: *Celestial Mechanics and Dynamical Astronomy* 130.10 (2018), p. 61 (cit. on p. 26).

[41] A. Ely Todd. «Frozen Elliptical Inclined Lunar Orbits». In: *The Journal of the Astronautical Sciences* 53.3 (2005), pp. 301–316 (cit. on p. 26).

[42] Giuliana E Miceli, Natasha Bosanac, Michael A Mesarch, David C Folta, and Rebecca L Mesarch. «Clustering approach to identifying low lunar frozen orbits in a high-fidelity model». In: *2023 AAS/AIAA Astrodynamics Specialist Conference*. AAS 23-142. 2023 (cit. on p. 26).

[43] Martin Lara, Bernard De Saedeleer, and Sebastián Ferrer. «Preliminary design of low lunar orbits». In: *Proceedings of the 21st International Symposium on Space Flight Dynamics*. 2009, pp. 1–15 (cit. on pp. 26, 59, 82).

[44] Michael L Lidov. «The evolution of orbits of artificial satellites of planets under the action of gravitational perturbations of external bodies». In: *Planetary and Space Science* 9.10 (1962), pp. 719–759 (cit. on p. 26).

[45] Yoshihide Kozai. «Motion of a lunar orbiter». In: *Publications of the Astronomical Society of Japan* 15.3 (1963), pp. 301–312 (cit. on p. 26).

[46] Martin Lara. «Design of long-lifetime lunar orbits: A hybrid approach». In: *Acta Astronautica* 69.3-4 (2011), pp. 186–199 (cit. on p. 27).

[47] James R. Wertz et al. *Orbit & Constellation Design & Management*. 2nd. Springer, 2009 (cit. on pp. 28, 29, 32, 35, 41, 42).

[48] Yuri Ulybyshev. «Satellite constellation design for continuous coverage: short historical survey, current status and new solutions». In: *Proceedings of Moscow Aviation Institute* 13.34 (2009), pp. 1–25 (cit. on p. 28).

[49] U.S. Naval Observatory (CNMOC). *Global Positioning System Overview*. 1998. URL: https://www.cnmoc.usff.navy.mil/Our-Commands/United-States-Naval-Observatory/Precise-Time-Department/Global-Positioning-System/Global-Positioning-System-Overview/ (cit. on p. 29).

[50] M Yakovlev. «The "IADC space debris mitigation guidelines" and supporting documents». In: *4th European Conference on Space Debris*. Vol. 587. ESA Publications Division Noordwijk, The Netherlands. 2005, pp. 591–597 (cit. on p. 29).

[51] Giacomo Curzi, Dario Modenini, and Paolo Tortora. «Large constellations of small satellites: A survey of near future challenges and missions». In: *Aerospace* 7.9 (2020), p. 133 (cit. on p. 29).

[52] Juan Misael Gongora-Torres, Cesar Vargas-Rosales, Alejandro Aragon-Zavala, and Rafaela Villalpando-Hernandez. «Elevation angle characterization for LEO satellites: First and second order statistics». In: *Applied Sciences* 13.7 (2023), p. 4405 (cit. on p. 37).

[53] John G. Walker. «Satellite Constellations». In: *Journal of the British Interplanetary Society* 37 (1984), pp. 559–571 (cit. on pp. 39, 41).

[54] John Gerard Walker. *Coverage Predictions and Selection Criteria for Satellite Constellations.* Tech. rep. 1982 (cit. on p. 39).

[55] S Huang, C Colombo, and F Bernelli-Zazzera. «Multi-criteria design of continuous global coverage Walker and Street-of-Coverage constellations through property assessment». In: *Acta Astronautica* 188 (2021), pp. 151–170 (cit. on pp. 41, 43).

[56] Yuri Ulybyshev. «Satellite constellation design for continuous coverage: short historical survey, current status and new solutions». In: *Proceedings of Moscow Aviation Institute* 13.34 (2009), pp. 1–25 (cit. on p. 41).

[57] David A. Vallado. *Fundamentals of Astrodynamics and Applications*. 2nd. Springer, 2001 (cit. on pp. 43, 45).

[58] L Rider. «Optimized polar orbit constellations for redundant earth coverage». In: *Journal of the Astronautical Sciences* 33 (1985), pp. 147–161 (cit. on p. 48).

[59] Christopher Rackauckas. «A comparison between differential equation solver suites in matlab, r, julia, python, c, mathematica, maple, and fortran». In: *Authorea Preprints* (2023) (cit. on p. 51).

[60] Charles R Harris et al. «Array programming with NumPy». In: *nature* 585.7825 (2020), pp. 357–362 (cit. on p. 51).

[61] Pauli Virtanen et al. «SciPy 1.0: Fundamental Algorithms for Scientific Computing in Python». In: *Nature Methods* 17 (2020), pp. 261–272. DOI: 10.1038/s41592-019-0686-2 (cit. on p. 51).

[62] J. D. Hunter. «Matplotlib: A 2D graphics environment». In: *Computing in Science & Engineering* 9.3 (2007), pp. 90–95. DOI: 10.1109/MCSE.2007.55 (cit. on p. 51).

[63] Wes McKinney et al. «pandas: a foundational Python library for data analysis and statistics». In: *Python for high performance and scientific computing* 14.9 (2011), pp. 1–9 (cit. on p. 51).

[64] Charles H Acton Jr. «Ancillary data services of NASA's navigation and ancillary information facility». In: *Planetary and Space Science* 44.1 (1996), pp. 65–70 (cit. on p. 51).

[65] A Annex. «SpiceyPy, a Python Wrapper for SPICE». In: *Third planetary data workshop and the planetary geologic mappers annual meeting*. Vol. 1986. 2017, p. 7081 (cit. on p. 51).

[66] AM Annex. «SpiceyPy, a Complete Pythonic Interface for Spice». In: *4th Planetary Data Workshop*. Vol. 2151. 2019, p. 7043 (cit. on p. 51).

[67] Mark Wieczorek and Matthias Meschede. «SHTools: Tools for Working with Spherical Harmonics». In: *Geochemistry, Geophysics, Geosystems* 19 (May 2018). DOI: 10.1029/2018GC007529 (cit. on p. 51).

[68] NASA Planetary Data System (PDS) Geosciences Node. *GRAIL Level 5 Reduced Data Record*. URL: https://pds-geosciences.wustl.edu/ (cit. on p. 55).

[69] Ryan S Park, William M Folkner, James G Williams, and Dale H Boggs. «The JPL planetary and lunar ephemerides DE440 and DE441». In: *The Astronomical Journal* 161.3 (2021), p. 105 (cit. on p. 55).

[70] Richard Brent, Shmuel Winograd, and Philip Wolfe. «Optimal iterative processes for root-finding». In: *Numerische Mathematik* 20.5 (1972), pp. 327–341 (cit. on p. 60).

[71] Bernard De Saedeleer and Jacques Henrard. «The combined effect of J2 and C22 on the critical inclination of a lunar orbiter». In: *Advances in Space Research* 37.1 (2006), pp. 80–87 (cit. on p. 77).

[72] Peng Zong Saeid Kohani. «Autonomous Semi-Major Axis adjustment for Mega Constellation Continuous Coverage». In: *The Journal of Space Safety Engineering* 5 (2018), pp. 203–208.

[73] Xu Yun et al. «LEO constellation design for regional coverage based on the safety of van allen belt radiation». In: *Advances in Space Research* 73 (2024), pp. 5582–5594.

[74] Roman Korobkov, Petr Mukhachev, and Dmitry Pritykin. «Traffic prediction model for broadband microsatellites constellations». In: *Advances in the Astronautical Sciences* (2020), pp. 75–89.

[75] NASA GSFC. *A standardized lunar coordinate system for lunar reconnaissance orbiter*. Tech. rep. Tech. rep. NASA Goddard Space Flight Center, Greenbelt, MD, 2008.

[76] Thomas P Robitaille et al. «Astropy: A community Python package for astronomy». In: *Astronomy & Astrophysics* 558 (2013), A33.

[77] Adrian M Price-Whelan et al. «The astropy project: Building an open-science project and status of the v2. 0 core package». In: *The Astronomical Journal* 156.3 (2018), p. 123.

[78] Adrian M Price-Whelan et al. «The Astropy Project: sustaining and growing a community-oriented open-source project and the latest major release (v5. 0) of the core package». In: *The Astrophysical Journal* 935.2 (2022), p. 167.

[79] Simon A Holmes and Will E Featherstone. «A unified approach to the Clenshaw summation and the recursive computation of very high degree and order normalised associated Legendre functions». In: *Journal of Geodesy* 76.5 (2002), pp. 279–299.

[80] Charles Acton, Nathaniel Bachman, Boris Semenov, and Edward Wright. «A look towards the future in the handling of space science mission geometry». In: *Planetary and Space Science* 150 (2018), pp. 9–12.

[81] Ralph B Roncoli. *Lunar constants and models document*. Jet Propulsion Laboratory, 2005.

[82] L Rider. «Analytic design of satellite constellations for zonal earth coverage using inclined circular orbits». In: *Journal of the Astronautical Sciences* 34 (1986), pp. 31–64.

[83] Wiley J Larson and James Richard Wertz. *Space mission analysis and design*. Dordrecht, 1999.

[84] David J Israel and Cheryl Jane Gramling. *LunaNet Interoperability Specification Document*. Tech. rep. 2023.

[85] Francesco Lopez, Anna Mauro, Domenico Edoardo Sfasciamuro, Andrea Villa, and Stefano Mauro. «Wireless power transmission: A new frontier for lunar colonisation development». In: *2024 11th International Workshop on Metrology for AeroSpace (MetroAeroSpace)*. IEEE. 2024, pp. 303–308.

[86] Erica Scantamburlo, Marco Luigi Ottavi, Domenico Edoardo Sfasciamuro, Leonardo Pappalardo, Ivano Verzola, and Stefano Mauro. «Wireless Power Transmission for lunar applications.» In: *2025 IEEE 12th International Workshop on Metrology for AeroSpace (MetroAeroSpace)*. IEEE. 2025, pp. 514–519.

[87] NASA's Scientific Visualization Studio. *CGI Moon Kit*. URL: `https://svs.gsfc.nasa.gov/4720`.